

Development of Atomic Magnetometry Towards Unshielded Sensors

Carolyn O'Dwyer

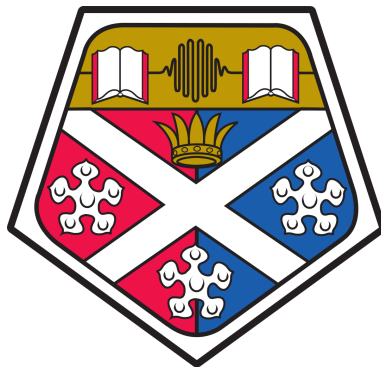
Abstract

This thesis describes experiments in double-resonance magnetometry with a view to the development of future portable magnetic sensors. Two experimental setups - shielded and unshielded - are described, as well as design choices that facilitate scalability to compact, portable sensors. This work includes several techniques to mitigate noise or otherwise improve sensitivity. Maintaining the sensitivity of the device has been prioritised while incorporating miniaturised components, and a sensitivity of $2 \text{ pT}/\sqrt{\text{Hz}}$ has been achieved in the unshielded environment. Additionally, the bandwidth of the sensor has been found to be 520 Hz. An iterative optimisation routine for the improvement of field homogeneity produced by static field coils is presented, as well as procedures for the characterisation of microfabricated atomic vapour cells. A technique to address periodic noise has been developed and has successfully suppressed noise arising from the 50 Hz mains AC line, with 22 dB noise suppression achieved between 45 and 55 Hz. Two magnetic gradiometry configurations are also discussed, and preliminary results presented, with an outlook to further development.

Development of Atomic Magnetometry Towards Unshielded Sensors

Carolyn O'Dwyer

A thesis submitted in partial fulfilment
of the requirements for the degree of
Doctor of Philosophy



Department of Physics
University of Strathclyde

July 27, 2020

Contents

| | Page |
|--|------------|
| Contents | i |
| Declaration | iii |
| Acknowledgements | iv |
| 1 Introduction | 1 |
| 1.1 Thesis Overview | 6 |
| 2 Theory | 8 |
| 2.1 Atomic Structure | 8 |
| 2.2 Atom-Light Interaction | 9 |
| 2.2.1 Saturation Parameter | 13 |
| 2.2.2 Optical Lineshape | 14 |
| 2.2.3 Optical Pumping | 15 |
| 2.3 Relaxation Mechanisms | 16 |
| 2.4 Atom-Field Interaction | 18 |
| 2.5 Magnetic Resonance Lineshape | 19 |
| 2.6 Signal Detection | 24 |
| 2.7 Sensitivity | 25 |
| 3 The Shielded Experiment | 27 |
| 3.1 Vapour Cells | 30 |
| 3.2 Magnetic Field Control | 35 |
| 3.2.1 Iterative Optimisation Routine | 36 |
| 3.3 Field Orientation Considerations | 40 |

| | | |
|----------|--|-----------|
| 4 | The Unshielded Experiment | 42 |
| 4.1 | Microfabricated Cells | 42 |
| 4.2 | Magnetometry Considerations for Buffer Gas Cells | 46 |
| 4.2.1 | Light Narrowing | 52 |
| 4.2.2 | Alignment to Orientation Conversion | 54 |
| 5 | Noise Suppression | 57 |
| 5.1 | Measurement-Induced Noise | 58 |
| 5.2 | Detection Noise | 60 |
| 5.3 | Measurement Modes | 61 |
| 5.4 | Feed-Forward Technique | 63 |
| 5.4.1 | Bandwidth Response | 68 |
| 5.4.2 | Signal Recovery | 71 |
| 6 | Gradiometry | 74 |
| 6.1 | Common-Mode Noise Cancellation | 74 |
| 6.2 | Microfabricated Cell Gradiometer | 76 |
| 6.3 | Glass Vapour Cell Gradiometer | 83 |
| 6.3.1 | Vapour Cell Mount Design | 83 |
| 6.3.2 | Sensor Characterisation | 84 |
| 7 | Conclusion and Outlook | 87 |
| | Appendix | 90 |
| | Bibliography | 96 |

Declaration

This thesis is the result of the author's original research. It has been composed by the author and has not been previously submitted for examination which has led to the award of a degree.

The copyright of this thesis belongs to the author under the terms of the United Kingdom Copyright Acts as qualified by University of Strathclyde Regulation 3.50. Due acknowledgement must always be made of the use of any material contained in, or derived from, this thesis.

Carolyn O'Dwyer
Glasgow, July 27, 2020

Acknowledgements

First, I would like to thank my supervisor Paul Griffin for his unwavering support throughout the course of my PhD and especially his assistance in getting this thesis over the line; all correct uses of semicolons in my writing may be credited to him. Thank you to Erling Riis for being a great boss who has provided excellent advice and support any time I needed it. I feel extremely lucky to have had two truly fantastic supervisors. I would also like to sincerely thank Stuart Ingleby for everyday technical support and guidance in the lab.

I have had the great pleasure of working in the EQOP Group, which is full of kind and clever people. Thank you for making my PhD years enjoyable and educational in equal measure. Thanks in particular to my fantastic office and lab mates for comic relief and camaraderie.

I would like to thank my examiners, David McKee and Peter Krueger for an interesting and enjoyable discussion and numerous helpful suggestions for improving this thesis.

The Disability and Wellbeing Service is a credit to Strathclyde, and I extend my thanks to the team and in particular to Cara Milor.

I am a product of all the great friends that I have around me, and I am grateful to have so many dear ones. In particular I would like to profusely thank Delia for her unwavering support even in the hardest of times. Thank you for buying me ice cream and helping to rephrase sentences. To all my climbing and cycling pals, thank you for the reminders that there is more to life than physics, and for making me do other types of difficult thing on a regular basis. A small thanks too to Odin for being a regular source of entertainment and a reasonably considerate home coworker.

I am indebted to my wonderful mum and dad, Rhona and Paul, who taught me to be a scientist and have always had my back. Thank you to my sisters Rachael and Ellen for being my support crew and for helping to complete the

O'Dwyer science triad. Finally, I would like to thank my love, Peter, from the bottom of my heart. Thank you for cooking countless gourmet thesis lunches, embarking on hare-brained trips with me, and for being my best friend.

Chapter 1

Introduction

The study of magnetic fields has been documented since 206 BCE [1]. Magnetic measurements began in China with lodestones suspended by silk strings or polished and placed on a flat surface. These devices pointed in the direction of the Earth's field, and were initially used for fortune telling and geomancy. By 1000 CE magnetic sensing was widely used for navigation, performed using a magnetised iron needle floating in water or suspended by a string [2]. In the 14th century the sailing season was extended by 5 months by the use of the compass; navigation with reference to the Earth's magnetic field could be done in poorer conditions without the sun or stars for reference [3].

Edmund Halley mapped the deviation of the compass from true north and produced a declination chart in 1701. This improved the precision of navigation as well as yielding an insight into the magnetic field of the Earth. The intensity of the Earth's field began to be measured in addition to its direction. This was achieved by comparing the period of oscillation of magnetised needles at different points on the globe. The oscillation period is inversely proportional to the square root of the field intensity [2]. The time variation of the local magnetic field began to be measured in the 1700s, and Graham produced a measurement of its diurnal variation due to interaction of the sun with the ionosphere in 1772 [4]. Observations such as these gave a better understanding of the dynamic forces that contribute to the local magnetic field.

Gauss made many great contributions to the study of magnetism. Previously, no measurement of the Earth's magnetic field had been made against an absolute scale. His measurement of a magnet deflecting a needle gave

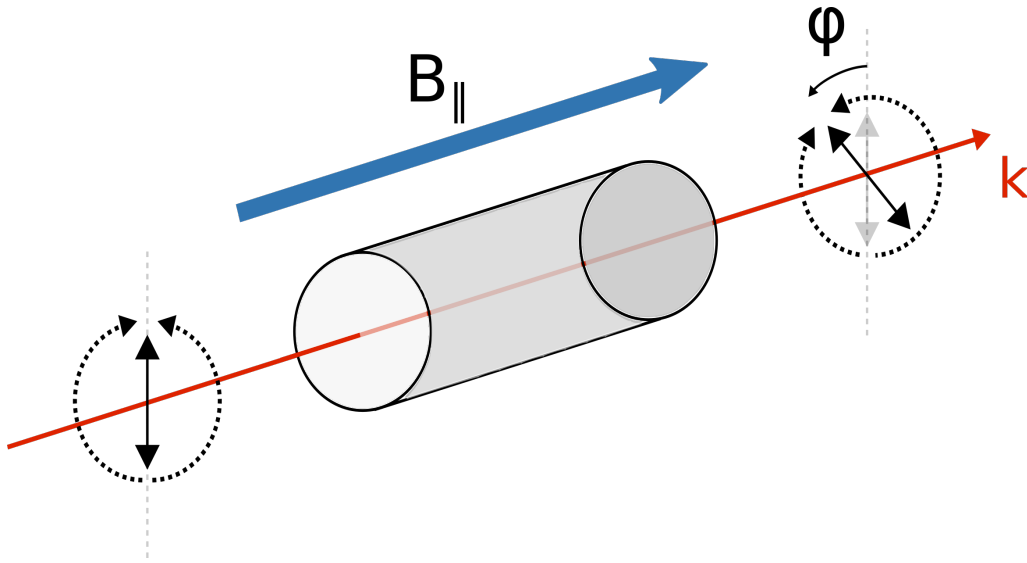


Figure 1.1: Schematic of the Faraday rotation experiment. A linearly polarised light beam, k , is incident upon leaded glass, which is in a magnetic field, $B_{||}$. The polarisation axis is rotated by the angle ϕ with respect to the original polarisation axis.

the magnetic moment M of the magnet, therefore allowing a calibration of the needle's deflection due to other fields, allowing a measurement of the horizontal component of the Earth's field, and the first measurement of the Earth's field that was not on an arbitrary scale [2]. Gilbert's De Magnete is the first known record of a proposed connection between magnetism and electricity [5], but it was Oersted who directly measured the relationship by the deflection of a compass needle due to a current flowing in a wire in 1820. This experiment triggered many exciting experiments and proposals in electromagnetism by many others, including Ampere and Faraday.

In 1845 Michael Faraday observed that when he shone linearly polarised light on a piece of leaded glass in a magnetic field, the initial polarisation angle of the light had been rotated when it left the sample, as seen in Figure 1.1. This experiment demonstrated the eponymous Faraday effect; when linearly polarised light travels through a medium that is experiencing a magnetic field along the axis of the light, the polarisation of the resultant light will have its axis rotated. The polarisation rotation is proportional to the strength of the magnetic field.

Macaluso and Corbino replicated the Faraday effect in an alkali vapour in 1898 [6]. They produced rotation of the polarisation proportional to the field

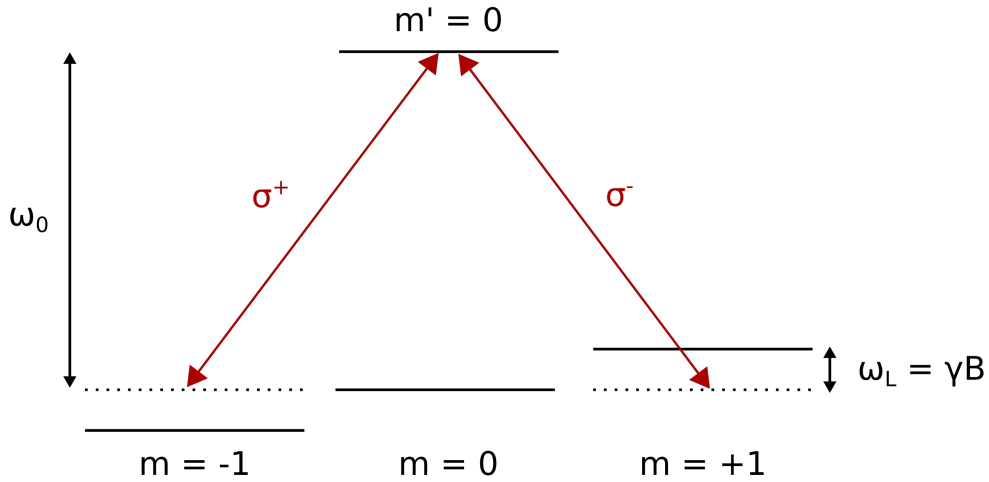


Figure 1.2: Linear polarised light interacting with a two-state atomic system in the presence of a magnetic field, B . The ground state Zeeman sublevels have been shifted and the left- and right- circularly polarised light components have different resonance frequencies.

applied but observed a resonant response of the polarisation rotation when the light frequency used was close to the atomic resonance frequency [7]. This resonant relationship was in fact the same effect as that observed by Faraday; the solid state effect produces a much wider dispersive feature than that of the alkali vapour. This experiment prompted Voigt to theorise that the polarisation rotation was due to the refractive index of the medium [8]. In order to describe the Macaluso-Corbino effect, it is useful to consider a semiclassical approach, where resonant classical light is incident on an atom with two states, with angular momentum 0 and 1. Linearly polarised light may be considered to be equal parts left and right circularly polarised; σ_+ and σ_- . The rotation of the polarisation axis in the Faraday effect arises due to each circular component acquiring a phase shift in the medium. The difference between the phase shift in each component gives the angle of rotation, ϕ . [8, 9]

Without a magnetic field, the Zeeman sublevels of the atoms are degenerate, and linearly polarised light couples only to $m = 0$. The resonant light at frequency ω_0 is unmodified. When a magnetic field, B , is present along the quantisation axis, the $m = +1$ and $m = -1$ states are shifted by ω_L , the

Larmor frequency,

$$\omega_L = \gamma B , \quad (1.1)$$

where γ is the gyromagnetic ratio. The components of the π -polarisation, σ_+ and σ_- , couple to the $m \pm 1$ ground state levels, but the splitting due to B means that the frequency response is changed, one blue- and one red-detuned. This is illustrated in Figure 1.2. The complex refractive index, η is given by:

$$\eta_{\pm} \approx 1 + 2\pi\chi_0 \frac{1}{(\delta \mp \omega_L) + i\Gamma_0/2} , \quad (1.2)$$

where χ_0 is the linear atomic susceptibility, δ is the frequency detuning from resonance, and Γ_0 is the rate of spontaneous relaxation from the excited to ground state. After traversing the medium, the sum of the circular components gives a rotation in the linear polarisation that is the function of the real parts of the refractive index:

$$\phi = \frac{\omega_0 l}{c} (Re[\eta_+] - Re[\eta_-]) , \quad (1.3)$$

where l is the length of the medium. The real part of Equation 1.2 for each transition is given by a Lorentzian; for small shifts the rotation can then be described with a dispersive profile.

Two significant advances in the mid twentieth century were the demonstration of optical detection of magnetic resonances in 1949 and optical pumping in 1950 [9, 10]. Optical pumping improved the achievable atomic spin polarisation by many orders of magnitude, and optical detection improved the efficiency of detection. These advances led to huge improvements in the signal to noise ratio for signals observed in atomic magnetometry.

Kastler and Brossel proposed a double-resonance method as early as 1949 [11], in which an on-resonance light beam was incident on the atoms while a radio-frequency field was tuned to resonance with the Larmor frequency. “Double-resonance” refers to the two resonant aspects of the system; the laser light and the RF field. The double-resonance configuration was demonstrated experimentally in 1952 [12].

In rapid succession Bell and Bloom demonstrated the first optical detection of magnetic resonance with crossed pump and probe beams. They observed the Larmor precession of the atoms imprinted on the intensity of the probe beam, coherently driven by an RF field [13]. The effects observed in these

experiments began to be described as a quantum effect, as an ensemble of spins rather than the bulk media of the original Faraday Effect.

After the invention of the laser in the 1960's, Gawlik et al. demonstrated the nonlinear Faraday effect with a coherent light source in 1974. The nonlinear Faraday rotation yielded a light intensity dependent polarisation rotation signal [14, 15]. Experiments such as this have given rise to a great many optically pumped magnetometer configurations, including many double-resonance schemes. The numerous sensor types will not be covered here but are described in detail by Budker et al. [8, 16] Savukov [17], and Kimball et al [9].

The field of optically pumped magnetometry has expanded rapidly since the 1960's. Monitoring the Larmor precession frequency gives a direct measurement of the ambient field, this means that OPMs require no calibration. This is an advantage over traditional sensors such as fluxgates and Hall probes. Many types of OPM have now been demonstrated with applications in geophysics [18], structural imaging, [19, 20] and RF communications [21].

Within optically pumped magnetometers, spin exchange relaxation-free (SERF) schemes lead the way in absolute sensitivity [22]. SERF sensors have achieved sensitivity in the aT range [23], but their measurement range is limited to near-zero fields [24]. Low-field sensors must operate in a magnetic shield or field-compensated room, but have exciting applications in magneto-cardiography (MCG), magnetoencephalography (MEG) [25] and fundamental physics [26].

Superconducting quantum interference devices (SQUIDs) and fluxgates are the main competitors to OPMs. They have long been established as sensitive and reliable magnetic sensors, but they have a number of limitations. SQUIDs require cryogenic cooling which limits their use as portable, compact sensors [27]. Fluxgates, despite their portability, lack the required sensitivity for applications with short integration times or those requiring good low frequency resolution, such as detection of rotating machinery [28, 29]. Optically pumped atomic magnetometers have sensing volumes with operating temperatures in the range 20-200°C and demonstrate sensitivities comparable with SQUIDs and far exceeding fluxgates.

The experiments discussed in this thesis have been built with a view to developing sensors that operate in the Earth's magnetic field. In order to operate in a wide range of applications, the sensor must have high dynamic

range, wide bandwidth, and high sensitivity. The scheme that has been explored in this thesis is the double-resonance magnetometer operating in Mx mode, which will be examined in detail in Chapter 3.

Portable, compact magnetic sensors will be useful for many unshielded applications. Several groups have already built impressive portable sensors [30–32] while maintaining high sensitivity. In biomagnetic applications, source localisation is a high priority. Compact sensors that may be placed in an array for this purpose are much in demand and already showing great promise [25, 33, 34].

1.1 Thesis Overview

This thesis describes an experimental framework for a double-resonance magnetometer, and includes an overview of the theoretical background of the experiment. Chapter 2 introduces theoretical principles which are important both in the discussion of the double resonance magnetometer, and in understanding the results presented in the following experimental chapters. Chapter 3 details the experimental setup of the shielded double-resonance magnetometer, which has been used to investigate effects inherent to this type of sensor, as well as development of calibration techniques. Much of this experimental work has contributed to the unshielded sensor presented in Chapter 4, which describes the operation of a similarly configured double resonance magnetometer without any static shielding. This setup has been used to test miniaturised components, including microfabricated cells. Chapter 5 describes and discusses the primary noise sources affecting the unshielded sensor, and presents a method for the suppression of periodic noise. A review of the principal results of this technique can be found in [35], by O’Dwyer et al. Chapter 6 describes preliminary work conducted in the unshielded environment using two different cell types to build a magnetic gradiometer. Provisional results are presented, as well as discussion on future work which may arise from this.

The work presented in this thesis has been conducted in the Experimental Quantum Optics and Photonics group at the University of Strathclyde. Two double resonance magnetometers were used to take the data in the following chapters. The shielded and unshielded sensors were designed and

constructed by the magnetometry team prior to the work described here being undertaken. The author has contributed to improvement of the software and optical hardware of the shielded experiment, and has implemented major modifications and upgrades to software and hardware to the unshielded experiment. All of the data in the following chapters was taken and analysed by the author. The author has benefited from working closely with postdoctoral researcher, Stuart Ingleby, and several publications have been written as a result of collaboration on these experiments.

Publications Arising from this Work

- Stuart J. Ingleby, Carolyn O’Dwyer, Paul F. Griffin, Aidan S. Arnold, and Erling Riis, “Orientational effects on the amplitude and phase of polarimeter signals in double-resonance atomic magnetometry” [Physical Review A 96, 1-6 \(2017\)](#), [arXiv:1707.04418](#)
- Stuart J. Ingleby, Iain C. Chalmers, Carolyn O’Dwyer, Paul F. Griffin, Aidan S. Arnold, and Erling Riis, “Optically pumped magnetometry in arbitrarily oriented magnetic fields,” [2017 IEEE SENSORS, Glasgow, 2017](#), pp. 1-3, doi: [10.1109/ICSENS.2017.8233895](#)
- Stuart J. Ingleby, Carolyn O’Dwyer, Paul F. Griffin, Aidan S. Arnold, and Erling Riis, “Vector Magnetometry Exploiting Phase-Geometry Effects in a Double-Resonance Alignment Magnetometer” [Physical Review Applied 10, 034035 \(2018\)](#), [arXiv:1802.09273](#)
- Carolyn O’Dwyer, Stuart J. Ingleby, Iain C. Chalmers, Paul F. Griffin, and Erling Riis, “A feed-forward measurement scheme for periodic noise suppression in atomic magnetometry” [Review of Scientific Instruments 91, 045103 \(2020\)](#), [10.1063/5.0002964](#)

Chapter 2

Theory

The theory of light-atom interactions is well understood, and a measure of its success is the excellent agreement with experimental results. This means that systems probed with lasers are ideal for precision measurement. Among the experiments benefiting from atomic precision are optically pumped magnetometers. This chapter will describe the theory and concepts required to describe the experimental double resonance magnetometer presented in the following chapters.

2.1 Atomic Structure

Alkali atoms are widely implemented in metrological measurements and atomic sensors due to their simple hydrogenic electronic structure, arising from a single valence electron. The main work in this section is to look at the coupling of the various angular momenta within the atom to describe a spinful system. This model can then be used to examine the atomic interaction with optical and magnetic fields in the following sections.

In a single-electron system, orbital angular momentum of the electron \mathbf{L} , which arises due to the motion of the electron around the atom, is constrained in the range $0 \leq L \leq n - 1$, where n is the principal quantum number, and L is the magnitude of the vector \mathbf{L} . The intrinsic angular momentum of the electron must also be considered. In this case the alkali earth metals have a single outer valence electron, and the ground state has a single electron spin $S = 1/2$. The total spin angular momentum is $\mathbf{S} = 1/2$ [36].

The total angular momentum of the electron, \mathbf{J} , is given by the sum of the vectors \mathbf{L} and \mathbf{S} . The coupling of \mathbf{L} and \mathbf{S} is described by the L-S coupling

scheme, which describes the splitting of the atomic states. The motion of the electron generates a magnetic field which lifts the degeneracy of the orbital structure and results in fine structure splitting. The quantum number \mathbf{J} is in the range $|L - S| \leq J \leq |L + S|$.

The spectroscopic notation used to describe the electronic configuration is $n^{2S+1}L_J$, where $L = 0, 1, \dots$, written in this notation as $L = S, P, \dots$ for the available orbitals. This work will be concerned only with the $6^2S_{1/2}$ and $6^2P_{1/2}$ states of caesium.

The interaction of \mathbf{I} , the total angular momentum of the nuclear spin, with the angular momentum of the electron causes hyperfine splitting of the fine structure. Similar to the fine structure described above, the total atomic angular momentum \mathbf{F} is given by $\mathbf{F} = \mathbf{I} + \mathbf{J}$. The magnitude of \mathbf{F} has the values $|I - J| \leq F \leq |I + J|$.

The hyperfine energy levels F split further to magnetic sublevels with magnetic quantum numbers m_F . The number of m_F sublevels for a given F state is given by $2F + 1$. The m_F states are degenerate in the absence of a magnetic field. The resulting states for caesium's first two subshells S and P are given in Figure 2.1. These represent the lowest energy levels of the outer shell $n = 6$ [37-39].

2.2 Atom-Light Interaction

In order to describe the interaction of light with alkali atoms it is useful to consider a two-level atomic system interacting with a plane wave, seen in Figure 2.2. The two-level atom can be described by defining a ground state $|g\rangle$, and an excited state $|e\rangle$, with corresponding energies $E_g = \hbar\omega_g$ and $E_e = \hbar\omega_e$.

The Hamiltonian \hat{H}_0 , can be written,

$$\hat{H}_0 = \hbar\omega_g |g\rangle \langle g| + \hbar\omega_e |e\rangle \langle e| . \quad (2.1)$$

To describe the light's interaction with the atomic system, the overall Hamiltonian becomes:

$$\hat{H} = \hat{H}_0 + \hat{H}_{AL} , \quad (2.2)$$

where \hat{H}_{AL} is the atom-light interaction Hamiltonian. This Hamiltonian is comprised of $\mathbf{E}(t)$, a classical plane-wave description of light, $\mathbf{E}(t) =$

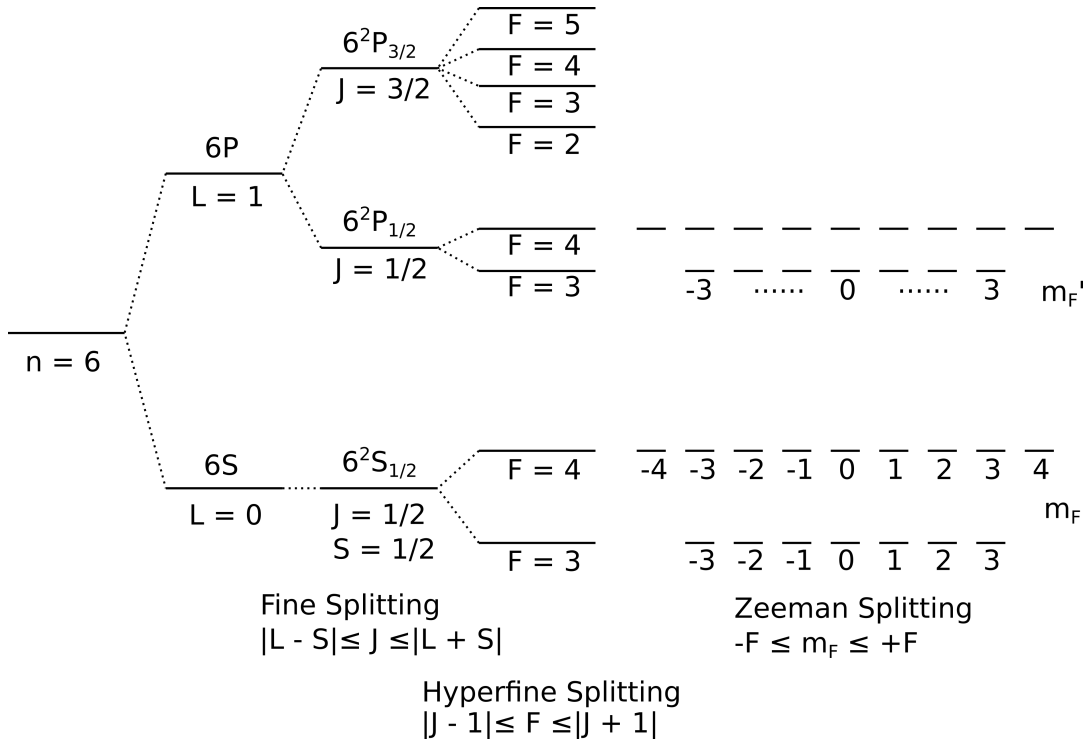


Figure 2.1: Overview of the quantum numbers describing caesium 6S and 6P manifolds, with magnetic sublevels relevant to this thesis shown. The nuclear spin of caesium is $I = 7/2$.

$\epsilon \mathbf{E}_0 \cos \omega_0 t$ and \mathbf{d} , the atomic dipole moment, to give:

$$\hat{H}_{AL} = -\mathbf{d} \cdot \mathbf{E}(t) = -\mathbf{d} \cdot \mathbf{E}_0 \cos \omega_0 t . \quad (2.3)$$

The wavefunction describes how this system evolves over time:

$$|\psi(t)\rangle = c_g(t) e^{-i\omega_g t} |g\rangle + c_e(t) e^{-i\omega_e t} |e\rangle , \quad (2.4)$$

with complex coefficients c_g and c_e . To model the dynamical evolution the time-dependent Schrödinger equation is used:

$$i\hbar \frac{\partial}{\partial t} |\psi(t)\rangle = \hat{H} |\psi(t)\rangle , . \quad (2.5)$$

By combining Equations 2.4 and 2.5 the time-dependent state amplitudes can be given:

$$i\hbar \dot{c}_k(t) = \sum_n c_n(t) e^{i\omega_{nk}t} \langle k | \hat{H} | n \rangle . \quad (2.6)$$

Substituting Equation 2.3 into Equation 2.6 results in the rate equations for

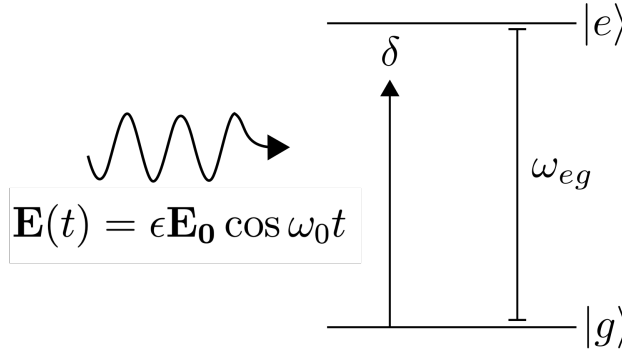


Figure 2.2: Two-level atom with ground and excited states, $|g\rangle$ and $|e\rangle$. The frequency of the resonant transition is ω_{eg} . A plane wave, $\mathbf{E}(t)$, is incident on the atom, which is detuned from the transition by the detuning, δ .

the complex coefficients with respect to time. Defining $\omega_e - \omega_g$ as ω_{eg} , these rate equations are:

$$i\hbar\dot{c}_g(t) = c_e(t)e^{-i\omega_{eg}t} \langle g | \mathbf{d} \epsilon | e \rangle E_0 \cos \omega_0 t \quad (2.7)$$

$$i\hbar\dot{c}_e(t) = c_g(t)e^{i\omega_{eg}t} \langle e | \mathbf{d} \epsilon | g \rangle E_0 \cos \omega_0 t \quad (2.8)$$

By taking the exponential form of the cosine terms, defining $\delta = \omega_0 - \omega_{eg}$ to be the detuning, and defining the Rabi frequency $\Omega = \frac{\langle g | \mathbf{d} | e \rangle E_0}{\hbar}$ these descriptions can be simplified. The rotating wave approximation removes the “fast oscillating” terms on the order of 2ω that arise. These terms do not contribute to the dynamics of the system on the time scales considered here [39]. This approximation produces:

$$\dot{c}_g(t) = ic_e(t) \frac{\Omega}{2} \exp(+i\delta t) \quad (2.9)$$

$$\dot{c}_e(t) = ic_g(t) \frac{\Omega}{2} \exp(-i\delta t) . \quad (2.10)$$

At this stage, introducing two new time dependent variables, $\tilde{c}_g(t)$ and $\tilde{c}_e(t)$:

$$\tilde{c}_g(t) = c_g(t) \exp\left(-\frac{i\delta t}{2}\right) \quad (2.11)$$

$$\tilde{c}_e(t) = c_e(t) \exp\left(\frac{i\delta t}{2}\right) \quad (2.12)$$

and then taking the derivative gives the time-evolution of a two-level system interacting with an electric field:

$$\begin{pmatrix} \dot{\tilde{c}}_g(t) \\ \dot{\tilde{c}}_e(t) \end{pmatrix} = \frac{i}{2} \begin{pmatrix} \delta & \Omega \\ \Omega & -\delta \end{pmatrix} \begin{pmatrix} \tilde{c}_e(t) \\ \tilde{c}_g(t) \end{pmatrix}. \quad (2.13)$$

From here the general solutions can be found. At this stage it is convenient to use a density matrix approach. The density matrix has an operator $\hat{\rho} = |\psi\rangle\langle\psi|$ which in the two level system gives the matrix:

$$\hat{\rho} = \begin{pmatrix} \rho_{gg} & \rho_{ge} \\ \rho_{eg} & \rho_{ee} \end{pmatrix} = \begin{pmatrix} |c_g|^2 & c_g c_e^* \\ c_e c_g^* & |c_e|^2 \end{pmatrix} \quad (2.14)$$

The diagonal entries represent the populations of the respective states, and the off-diagonals the coherences between the states. At this stage the Bloch equations can be derived using the Liouville equation, which is a general form of the master equation. The Liouville equation accounts for coherent processes of the system which lead to Rabi oscillations, stimulated emission and absorption. The incoherent process of spontaneous emission requires an additional decay term, Γ_0 . By modifying the Liouville equation, the Lindblad master equation can be given:

$$\dot{\hat{\rho}} = \frac{i}{\hbar} [\hat{\rho}, \hat{H}] + \mathcal{L}\hat{\rho}, \quad (2.15)$$

Where $\mathcal{L}\hat{\rho}$ is the Lindblad operator:

$$\mathcal{L}\hat{\rho} = \begin{pmatrix} \Gamma_0 \rho_{ee} & -\frac{\Gamma_0}{2} \tilde{\rho}_{ge} \\ -\frac{\Gamma_0}{2} \tilde{\rho}_{eg} & -\Gamma_0 \rho_{ee} \end{pmatrix}. \quad (2.16)$$

Equation 2.15 describes the time evolution of the system due to coherent and incoherent processes during interaction with a classical light field. From here the Optical Bloch equations can be described:

$$\dot{\rho}_{ee} = -\Gamma_0 \rho_{ee} + \frac{i\Omega}{2} (\tilde{\rho}_{ge}^* - \tilde{\rho}_{ge}) \quad (2.17)$$

$$\dot{\rho}_{gg} = \Gamma_0 \rho_{ee} + \frac{i\Omega}{2} (\tilde{\rho}_{ge}^* - \tilde{\rho}_{ge}) \quad (2.18)$$

$$\dot{\rho}_{ge}^* = \dot{\rho}_{eg} = \left(\frac{\Gamma_0}{2} + i\delta \right) \tilde{\rho}_{eg} + \frac{i\Omega}{2} (\rho_{gg} - \rho_{ee}) \quad (2.19)$$

Spontaneous decay from the excited to ground state interrupts the coherent dynamics of an atom at random, so that at long time periods in an ensemble of atoms there will be many atoms oscillating out of phase with one another. The steady-state solution for time $t \gg 1/\Gamma_0$ can be solved by setting Equations 2.17 to zero, and using the relation $\rho_{ee} + \rho_{gg} = 1$, to find:

$$\rho_{ee}^{SS} = \frac{\Omega^2/4}{(\Omega^2/2 + \Gamma_0^2/4 + \delta^2)} \quad (2.20)$$

$$\tilde{\rho}_{eg}^{SS} = \frac{\Omega}{2} \frac{\delta - i\Gamma_0/2}{(\Omega^2/2 + \Gamma_0^2/4 + \delta^2)}, \quad (2.21)$$

which describe the steady-state population of the excited state and coherence for the spontaneous emission from excited to ground states.

2.2.1 Saturation Parameter

The saturation parameter, S , can be defined with respect to a given transition as the population saturation as a function of the Rabi frequency. This describes the ratio of coherent to incoherent decay rates of the system:

$$S = \frac{\Omega^2/2}{\delta^2 + \Gamma_0/2} = \frac{s_0}{1 + (2\delta/\Gamma_0)}. \quad (2.22)$$

s_0 is defined as the resonant saturation parameter which characterises the strength of the atomic transition,

$$s_0 = \frac{2\Omega^2}{\Gamma_0^2} = \frac{I}{I_{\text{sat}}}, \quad (2.23)$$

where I is the intensity of the laser light and I_{sat} is the saturation intensity. For experimental considerations the low-light power regime can be defined as when $I \ll I_{\text{sat}}$. Practically this means that the atoms remain mostly in the ground state.

The steady-state photon scattering rate, R_{scat} , is the rate at which an atom emits a photon. R_{scat} depends upon how many atoms are in the excited state, and the rate of spontaneous decay,

$$R_{\text{scat}} = \Gamma_0 \rho_{ee}^{SS} = \frac{\Gamma_0}{2} \frac{s_0}{1 + s_0 + 4(\frac{\delta}{\Gamma_0})^2}. \quad (2.24)$$

2.2.2 Optical Lineshape

Up to this point the atomic transition has been considered as having a single resonant frequency. In reality, the transition is always a spread of frequencies characterised by the transition linewidth. The atomic linewidth arises due to both features of the atom itself; natural broadening, and external effects that may be homogeneous or inhomogeneous. The natural linewidth of a transition arises from the finite excited-state lifetime and is characterised by a Lorentzian profile. A Lorentzian profile also describes other homogeneous broadening effects, while inhomogeneous effects have a Gaussian lineshape. The normalised Lorentzian spectral distribution due to natural broadening is given by:

$$\phi_0(\nu) = \frac{1}{\pi} \frac{\Gamma_0/2}{(\nu - \nu_0)^2 + (\Gamma_0/2)^2}, \quad (2.25)$$

for a frequency ν relative to the resonance frequency ν_0 . Γ_0 is the spontaneous decay rate from the excited state.

Collisional or pressure broadening also has a Lorentzian lineshape. The effective linewidth Γ_{eff} can be used to describe the natural linewidth plus the contributions from collisions, Γ_{coll} . This term is dependent on the cross-section and the thermal velocity of the atoms. Collisional broadening is a homogeneous effect and therefore has a Lorentzian optical profile. This holds not only for alkali-alkali collisions but also alkali-buffer gas collisions [40, 41]. The collision-broadened lineshape will be discussed in more detail in Section 4.2.

Doppler broadening is a source of inhomogeneous broadening of the spectral line. For a thermal sample of atoms, the velocities of the atoms are described by the Maxwell-Boltzmann distribution. Each velocity class of atoms experiences a different laser frequency due to the Doppler effect as they move with respect to the light. This gives an inhomogeneous profile which is Gaussian:

$$\phi(\nu) = \frac{2 \ln 2}{\sqrt{\pi} \Delta_D} \exp \left[-\ln 2 \left(\frac{\nu - \nu_0}{\Delta_D/2} \right)^2 \right], \quad (2.26)$$

where Δ_D is the FWHM of the Doppler broadened profile, given by: $\Delta_D = \nu_0 \sqrt{8 k_B T \ln 2 / m c^2}$ which takes into account the most probable speed of an atom in a vapour. Boltzmann's constant is k_B , m is the mass of the atom, and c is the speed of light.

Convolving the Lorentzian and Gaussian profiles gives the Voigt profile [40, 42]. The cells in this thesis are operated at or above room temperature, with a FWHM $\Delta_D \approx 360$ MHz [43]. Doppler broadening is dominant except in the case of cells containing sufficiently high buffer gas pressure, which will be discussed in Section 4.

2.2.3 Optical Pumping

Optical pumping is the process by which angular momentum is transferred from light to the atoms in order to transfer them to a desired state. A resonant photon may transfer one unit of angular momentum to an atom at a time, exciting the atom to an excited state given by the polarisation of the light. The m_F magnetic sublevels have the following selection rules: $m'_F = m_F + 1$ for σ_+ transitions, $m'_F = m_F - 1$ for σ_- transitions, and $m'_F = 0$ for π transitions. Once in an excited state, the atom will decay, with a probability of decaying to a particular ground state given by the relevant Clebsch-Gordon coefficients.

For the purposes of this thesis, the $F = 4 \rightarrow F' = 3$ optical transition of the caesium D1 line will be considered, as it is the one primarily used for optical pumping. With light polarised to drive σ_+ -transitions, the atoms will absorb and spontaneously emit many photons until they decay to the $m_F = +4$ magnetic sublevel (neglecting decay to the $F = 3$ sublevel). This state is “dark”, meaning that it is transparent to the laser light. At this point no further pumping of these atoms occurs. By populating this state while continuing to depopulate all others, a net magnetisation \mathbf{M} is created in the sample. This is an orientation moment, with a preferred direction. An orientation moment may also be created by driving σ_- -transitions to populate the $m_F = -4$ state. Similarly, an aligned state may be created by the action of a π -polarised transition which can drive the population to the $m_F \pm 4$ states. The alignment moment has no preferred direction but does have a preferred axis. A schematic of the atomic population and both pumping processes is shown in Figure 2.3.

The subsequent precession between adjacent m_F levels at the Larmor frequency creates the magnetometry signal. The signal detected is due to the rotation of the light polarisation as the populations of the m_F sublevels precess in and out of the dark ground states to the bright ones. The precession

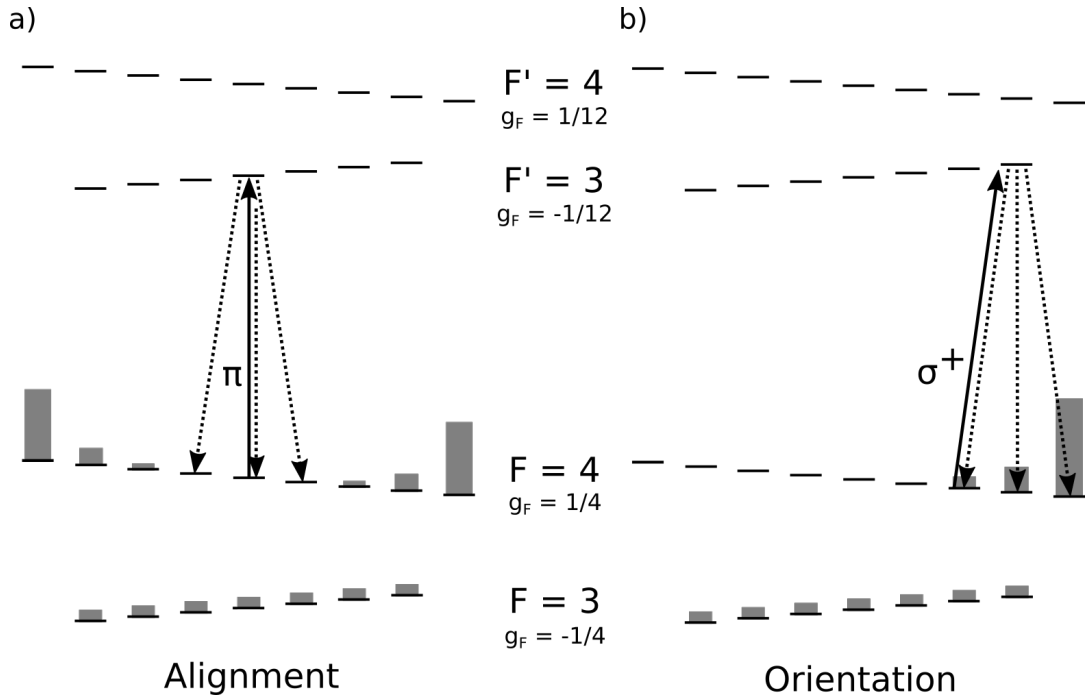


Figure 2.3: Level diagram of the hyperfine states in the D1 line of caesium with resolved excited hyperfine states. The light is resonant with the $F = 4 \rightarrow F' = 3$ states. Level populations are shown representing the pumping of the atomic ensemble into an aligned, a) or oriented, b) state. The level diagrams a) and b) are identical, with linear (π) polarised light in a) and right-circular (σ_+) polarised light in b).

of a magnetic moment will be discussed in Section 2.5 and the resulting signal in Section 2.6.

Regardless of the moment created, some population of the $F = 3$ ground state will remain. The precession of this state is in the opposite direction to that of the $F = 4$, and can cause depolarising spin-exchange collisions. Two-beam magnetometers benefit from being able to pump on one transition and probe on the other, and the pump and probe beams may have different polarisation. In a single-beam setup with resolved hyperfine levels, pumping and probing is limited to the same transition.

2.3 Relaxation Mechanisms

Once the atoms have been pumped into an aligned or oriented state, it is advantageous that the state is conserved until they can interact with the probe beam. Relaxation contributions can be categorised as intrinsic or

extrinsic. Intrinsic processes depend on atomic cell design and temperature, while extrinsic processes are operational; sources of perturbation such as laser light and oscillating magnetic fields light power and RF power [44].

For a caesium atom in a glass cell, there are three types of intrinsic relaxation contribution due to collisions: alkali–wall, alkali–buffer gas, and alkali–alkali. Rates here will be defined as Γ_i , which are the inverse of the relevant coherence lifetime, T_i . Within intrinsic relaxation rates there are longitudinal, Γ_1 , and transverse Γ_2 contributions with respect to the quantisation axis.

The longitudinal lifetime T_1 is dependent on mechanisms affecting the expectation value of the spin component along the quantisation axis, B . The lifetime, T_1 is comprised of the following contributions [45]:

$$\frac{1}{T_1} = \frac{1}{q} (\Gamma_{\text{SD}} + \Gamma_{\text{P}}) + \Gamma_{\text{wall}} , \quad (2.27)$$

where Γ_{SD} is the spin-destruction rate, Γ_{P} is the relaxation rate due to absorption of a photon from the incident beam, Γ_{wall} is the rate of decoherence due to wall collisions, and q is the nuclear slowing down factor. After spin-changing collisions, some spin polarisation will be preserved. The nuclear spin polarisation is much longer lived than that of the electron, and q here quantifies how much spin polarisation remains. Γ_{SD} arises due to collisions between the probed species and alkali, $\Gamma_{\text{SD}}^{\text{Cs}}$, buffer, $\Gamma_{\text{SD}}^{\text{B}}$ and quenching gases, $\Gamma_{\text{SD}}^{\text{Q}}$. Buffer and quenching gases may be introduced as separate species, or a single species may be used for both purposes. The spin-destruction due to these contributions is given by:

$$\Gamma_{\text{SD}} = \Gamma_{\text{SD}}^{\text{Cs}} + \Gamma_{\text{SD}}^{\text{B}} + \Gamma_{\text{SD}}^{\text{Q}} . \quad (2.28)$$

The transverse lifetime is due to dephasing between precessing atoms:

$$\frac{1}{T_2} = \frac{1}{T_1} + \frac{1}{q_{\text{SE}}} \Gamma_{\text{SE}} + \Gamma_{\text{gr}} , \quad (2.29)$$

where Γ_{gr} is the dephasing contribution due to gradients. The spin-exchange broadening factor, q_{SE} , is dependent on the field magnitude and vapour density.

The transverse and longitudinal relaxation lifetimes have been investigated experimentally for large antirelaxation coating vapour cells by Castagna et al. [46] and for microfabricated cells with buffer gas by Scholtes et al. [44].

The contributions to relaxation in this thesis will be discussed in detail in Sections 3.1 and 4.1.

2.4 Atom-Field Interaction

The quantum numbers given in Section 2.1 which describe the states including the hyperfine interaction are L , S , and I . The Hamiltonian to describe the contributions from the orbital and nuclear spin components in the presence of a magnetic field is:

$$\hat{H}_B = \frac{\mu_B}{\hbar}(g_S \mathbf{S} + g_L \mathbf{L} + g_I \mathbf{I}) \cdot \mathbf{B} , \quad (2.30)$$

where μ_B is the Bohr magneton, g_S is the electron spin g-factor, g_L is the electron orbital g-factor, and g_I is the nuclear g-factor. These g-factors are dimensionless proportionality constants.

When the magnetic field, B , is small enough that the energy splitting induced is small with respect to the hyperfine structure splitting, F is a good quantum number, and the splitting can be described:

$$\Delta E_{|F, m_F\rangle} = \mu_B g_F m_F B_z , \quad (2.31)$$

where g_F is the Landé g-factor for the hyperfine splitting:

$$g_F = g_J \left(\frac{F(F+1) + J(J+1) - I(I+1)}{2F(F+1)} \right) + \dots \quad (2.32)$$

$$g_I \left(\frac{F(F+1) - J(J+1) + I(I+1)}{2F(F+1)} \right)$$

Equation 2.31 describes the linear Zeeman effect, which only occurs in very low magnetic fields.

The Breit-Rabi formula can be used to calculate the energy shifts for states with angular momentum $J = 1/2$:

$$E_{|F=I+1/2, m_F\rangle} = -\frac{E_{\text{HFS}}}{2(2I+1)} - g_I \mu_B B m_F \pm \frac{E_{\text{HFS}}}{2} \left(1 + \frac{4m_F x}{2I+1} + x^2 \right)^{\frac{1}{2}} , \quad (2.33)$$

where $E_{\text{HFS}} = A_{\text{HFS}}(I + 1/2)$, A_{HFS} is the hyperfine structure constant, and

x is given by:

$$x = \frac{(g_I + g_J)\mu_B B}{E_{\text{HFS}}} . \quad (2.34)$$

Equation 2.33 is used to calculate the splitting of the D1 ground state hyperfine levels $F = 3$ and $F = 4$ into the m_F Zeeman sublevels, shown in Figure 2.4.

For the ground state of caesium considered here, $6^2S_{1/2}$, $S = 1/2$, $L = 0$, $J = 1/2$, and $I = 7/2$. For the lower ground state, $F = I - J$, and for the upper ground state, $F = I + J$. Neglecting the effect of g_I , and using $g_F \approx 2$, this leads from Equation 2.32 to:

$$g_F = \pm \frac{2}{2I + 1} . \quad (2.35)$$

These opposite signed g-factors result in opposite signed Larmor precession frequencies [37].

2.5 Magnetic Resonance Lineshape

In the classical picture, an alkali atom prepared in a magnetised state will precess about the static field, with a frequency given by:

$$\omega_L = \gamma B_0 , \quad (2.36)$$

where γ is the gyromagnetic ratio, defined by fundamental constants:

$$\gamma = \frac{eg_F}{2m_e} , \quad (2.37)$$

e is the electron charge, g_F is the g-factor defined in Equation 2.35, and m_e is the mass of the electron. If the atomic ensemble experiences a magnetic field, each atom will precess, but with a random phase. Probing the ensemble will result in a detected signal averaging to 0. Resonant excitation of the atomic precession is required to coherently drive the spin ensemble in phase, which will then lead to a non-zero signal detected.

The magnetisation of the atomic ensemble, \mathbf{M} , is the sum of the individual moments of each spin that contributes to the magnetometer signal. \mathbf{M} can be considered as a classical vector in a static magnetic field, \mathbf{B}_0 in the z -direction. The evolution of the spin ensemble can be modelled as

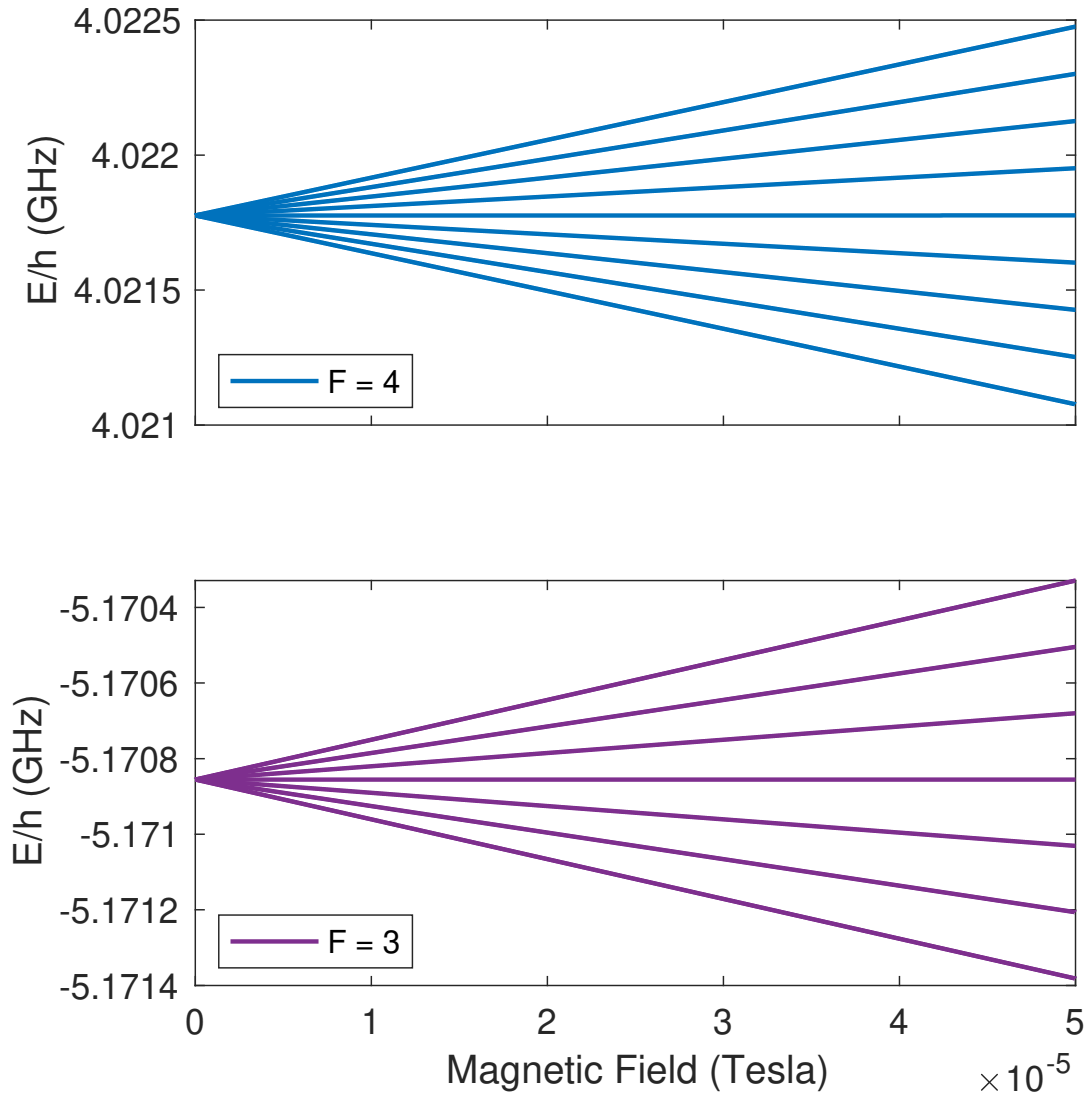


Figure 2.4: Splitting of the Zeeman sublevels for the ground-state $F = 3$ and $F = 4$ hyperfine levels. The y-axis splitting in GHz/h is with respect to the energy of the $6^2S_{1/2}$ level. The range of magnetic fields for which the splitting is shown is representative of the field magnitudes used in this thesis.

\mathbf{M} precesses about \mathbf{B}_0 at the Larmor frequency, ω_L . \mathbf{M} has components $\{M_x, M_y, M_z\}$ in the lab frame.

The time evolution is given by:

$$\frac{\partial \mathbf{M}}{\partial t} = \gamma \mathbf{M} \times \mathbf{B}_0, \quad (2.38)$$

which for each component of \mathbf{M} is:

$$\frac{\partial M_x}{\partial t} = \gamma M_y(t) B_z \quad (2.39)$$

$$\frac{\partial M_y}{\partial t} = \gamma M_x(t) B_z \quad (2.40)$$

$$\frac{\partial M_z}{\partial t} = 0. \quad (2.41)$$

As \mathbf{B}_0 has been defined along the z -axis, the field contributions are due to B_z alone. This describes precession of \mathbf{M} about \mathbf{B}_0 in the $x - y$ -plane.

In matrix form:

$$\dot{\mathbf{M}} = \gamma \begin{pmatrix} M_x \\ M_y \\ M_z \end{pmatrix} \times \begin{pmatrix} 0 \\ 0 \\ B_z \end{pmatrix}. \quad (2.42)$$

Relaxation of the magnetisation occurs in all three components of \mathbf{M} . The transverse relaxation term, Γ_2 , affect the components in the $x - y$ -plane, and the longitudinal term, Γ_1 , affects the z -component. At $t \rightarrow \infty$, the M_x and M_y components relax to zero, and the M_z component relaxes towards M_0 , the steady-state magnetisation. The relaxation terms are summed with the evolution described in Equation 2.42

$$\dot{\mathbf{M}} = \gamma \mathbf{M} \times \mathbf{B}_0 - \begin{pmatrix} \Gamma_2 & 0 & 0 \\ 0 & \Gamma_2 & 0 \\ 0 & 0 & \Gamma_1 \end{pmatrix} \begin{pmatrix} M_x \\ M_y \\ M_z \end{pmatrix} + \Gamma_1 \begin{pmatrix} 0 \\ 0 \\ M_0 \end{pmatrix}. \quad (2.43)$$

In order to drive the coherent precession in the transverse field, an RF field is introduced which co-rotates with \mathbf{M} . It is convenient to transform to a rotating frame at the driving frequency of the RF field, ω_{RF} . This ensures that the only component moving in the rotating frame is the RF field along y' . The transformation can be seen in Figure 2.5. The magnetisation and magnetic field in the rotated frame are signified as \mathbf{M}' and \mathbf{B}' respectively. The transformation from the lab to the rotating frame coordinates is made

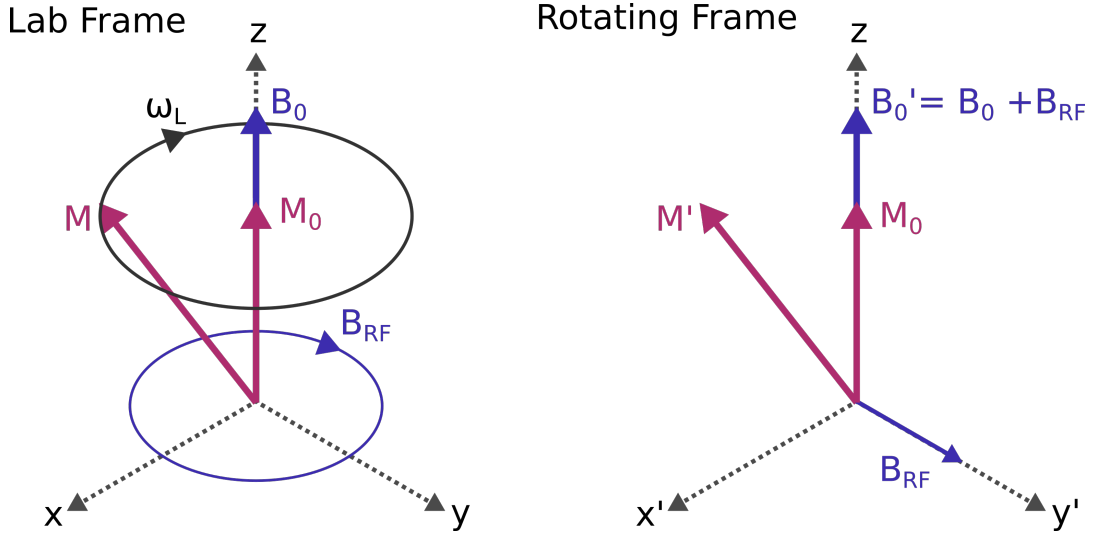


Figure 2.5: Transformation from the lab frame to the rotating frame. The rotating frame rotates about the z -axis at a frequency ω_{RF} .

using the following relation:

$$M_x = M'_x \cos(\omega_{\text{RF}}t) + M'_y \sin(\omega_{\text{RF}}t) \quad (2.44)$$

$$M_y = M'_x \sin(\omega_{\text{RF}}t) - M'_y \cos(\omega_{\text{RF}}t) , \quad (2.45)$$

which transforms Equation 2.43 to:

$$\dot{\mathbf{M}}' = \gamma \begin{pmatrix} M'_x \\ M'_y \\ M'_z \end{pmatrix} \times \begin{pmatrix} -B_{\text{RF}} \\ 0 \\ B_0 + B_{\text{RF}} \end{pmatrix} - \begin{pmatrix} \Gamma_2 & 0 & 0 \\ 0 & \Gamma_2 & 0 \\ 0 & 0 & \Gamma_1 \end{pmatrix} \begin{pmatrix} M'_x \\ M'_y \\ M'_z \end{pmatrix} + \Gamma_1 \begin{pmatrix} 0 \\ 0 \\ M_0 \end{pmatrix} , \quad (2.46)$$

which is the evolution of \mathbf{M}' in the rotating frame.

The magnetic detuning, Δ , between the RF field frequency and the Larmor frequency can be defined here as $\gamma(B_0 + B_{\text{RF}}) = \Delta$, and the RF Rabi frequency, Ω_{RF} is γB_{RF} [47]. By expanding the cross-product in Equation 2.46 and making these substitutions, the system can then be written as:

$$\dot{\mathbf{M}}' = \begin{pmatrix} 0 & \Delta & 0 \\ -\Delta & 0 & -\Omega_{\text{RF}} \\ 0 & \Omega_{\text{RF}} & 0 \end{pmatrix} \begin{pmatrix} M'_x \\ M'_y \\ M'_z \end{pmatrix} - \begin{pmatrix} \Gamma_2 & 0 & 0 \\ 0 & \Gamma_2 & 0 \\ 0 & 0 & \Gamma_1 \end{pmatrix} \begin{pmatrix} M'_x \\ M'_y \\ M'_z \end{pmatrix} + \Gamma_1 \begin{pmatrix} 0 \\ 0 \\ M_0 \end{pmatrix} . \quad (2.47)$$

By combining the relaxation terms this becomes:

$$\dot{\mathbf{M}}' = \begin{pmatrix} -\Gamma_2 & \Delta & 0 \\ -\Delta & -\Gamma_2 & \Omega_{\text{RF}} \\ 0 & \Omega_{\text{RF}} & -\Gamma_1 \end{pmatrix} \begin{pmatrix} M'_x \\ M'_y \\ M'_z \end{pmatrix} + \Gamma_1 \begin{pmatrix} 0 \\ 0 \\ M_0 \end{pmatrix}. \quad (2.48)$$

The steady state solutions are obtained by setting $\dot{\mathbf{M}} = 0$ and solving for $\{M'_x, M'_y, M'_z\}$, giving:

$$M'_x = M_0 \frac{\Omega_{\text{RF}} \Delta}{\Gamma_2^2 + \Delta^2 + \frac{\Gamma_2}{\Gamma_1} \Omega_{\text{RF}}^2} \quad (2.49)$$

$$M'_y = M_0 \frac{\Omega_{\text{RF}} \Gamma_2}{\Gamma_2^2 + \Delta^2 + \frac{\Gamma_2}{\Gamma_1} \Omega_{\text{RF}}^2} \quad (2.50)$$

$$M'_z = M_0 \frac{\Delta^2 + \Gamma_2^2}{\Gamma_2^2 + \Delta^2 + \frac{\Gamma_2}{\Gamma_1} \Omega_{\text{RF}}^2}. \quad (2.51)$$

For the purpose of the signals observed in this work, $\Gamma_2 \approx \Gamma_1$, and Γ will be used from this point to refer to Γ_2 . Γ can be defined as the FWHM (full width, half max) of a Lorentzian lineshape. The RF saturation parameter, is $S = \frac{\Omega_{\text{RF}}}{\Gamma}$ and $x = \frac{\Delta}{\Gamma}$. These simplifications give a standard Lorentzian form with absorptive and dispersive components, M'_x and M'_y :

$$M'_x = SM_0 \frac{x}{x^2 + S^2 + 1} \quad (2.52)$$

$$M'_y = SM_0 \frac{1}{x^2 + S^2 + 1}. \quad (2.53)$$

Equation 2.45 can be used to transform back to the laboratory frame.

In this thesis, the light propagation axis is defined along y . As will be expanded upon in the following section, the spin component imprinted on the probe beam is M_y , which has contributions from the M'_x and M'_y oscillating in-phase and in quadrature with respect to the RF field. By demodulating the signal at ω_{RF} , these components may be extracted from the probe beam, yielding in-phase (IP) and quadrature (Q) signals:

$$IP = \frac{xA}{1 + S^2 + x^2} \quad (2.54)$$

$$Q = \frac{A}{1 + S^2 + x^2}, \quad (2.55)$$

where A is the signal amplitude of the resonance. There exists a discrep-

ancy in the terminology used to describe the absorptive and dispersive terms arising due to the optical rotation in magnetometry. The convention in this group has been to describe the in-phase and quadrature components by the outputs of the demodulation, as in lock-in detection [48], such that the dispersive curve is the in-phase component, and the absorptive is the quadrature component. For the remainder of this thesis, the in-phase and quadrature signals will be referred to as X and Y , respectively.

2.6 Signal Detection

In this thesis the detection of the probe beam is done using a balanced polarimeter. After interacting with the atoms, the probe passes through a half waveplate followed by a polarising beamsplitter. The light is then detected on a balanced photodetector. The waveplate is used to adjust the polarisation axis of the probe such that the intensity of the ports of the polarimeter is equal. The subtractive photodiode reads zero signal when there is no optical rotation of the light polarisation. Any imbalance of the ports of the beamsplitter indicates a rotation of the probe beam.

The Larmor precession of the atoms is imprinted on to the beam as a rotation of the polarisation components of the light. By monitoring the ports of the beamsplitter the angle of polarisation can be extracted. The intensity of the light from each port, I_1 and I_2 are given by Malus's law,

$$I_1 = I_0 \sin^2 \left(\phi - \frac{\pi}{4} \right) \quad (2.56)$$

$$I_2 = I_0 \cos^2 \left(\phi - \frac{\pi}{4} \right) . \quad (2.57)$$

I_0 is the initial intensity of the beam before passing through the beamsplitter, and ϕ is the angle of polarisation of the light. Subtracting the intensity of each port of the beamsplitter yields the polarisation rotation angle for small rotations, given as:

$$\phi = \frac{I_1 - I_2}{2(I_1 + I_2)} \quad (2.58)$$

This holds for the experiments described in the following chapters for the detection of circular and linear polarised light [7, 40].

2.7 Sensitivity

The DC sensitivity of the sensor is the smallest change in the measured field that it is capable of detecting. The Larmor frequency is measured by monitoring the on-resonance slope of the dispersive (in-phase) curve described in Equation 2.55. The on-resonance gradient is the change in the magnetic field δB with respect to the change in the amplitude of the in-phase signal, δX . It is given by:

$$\frac{\delta B}{\delta X} = \frac{\Gamma}{\gamma SNR} , \quad (2.59)$$

where Γ is the FWHM, γ is the gyromagnetic ratio; in the 6S ground state manifold of caesium $\gamma = 3.5 \text{ Hz/nT}$. The signal-to-noise ratio, SNR , is the ratio of the resonance amplitude to the noise on the measurement. The sensitivity of the sensor improves as the slope of the resonant response becomes steeper. The following chapters describe techniques and design choices that have been chosen to maximise the sensitivity of the sensor by increasing the signal amplitude, narrowing the FWHM, and decreasing the noise.

The fundamental sensitivity of optically-pumped magnetometers is limited by the spin-projection noise and photon shot-noise contributions [8]; methods for approaching these limits have been discussed extensively elsewhere [49, 50]. The photon shot noise has been defined by modifying the approach taken by Schultze et al. [51] for the balanced polarimeter used in the following chapters. The root mean square photon shot noise is defined as:

$$\delta V_{SN} = G\sqrt{2eRP_{opt}} , \quad (2.60)$$

where G is the gain of the detector; e is the electron charge; R is the responsivity of the photodetector, adjusted for the wavelength of incident light; P_{opt} is the total optical power incident on the detectors. The noise sources that affect the sensitivity of the magnetometer will be discussed in detail in Chapter 5.

The sensitivity of a magnetometer is given in units of $\text{T}/\sqrt{\text{Hz}}$. This means that the sensitivity improves as the square root of the total measurement time. Here the sensitivity of the device is defined as the square root of the power spectral density (PSD):

$$\sqrt{PSD} = \frac{1}{\sqrt{BW}} \frac{\delta B}{\delta X} \partial X , \quad (2.61)$$

where BW is the measured bandwidth of the magnetometer, $\frac{\delta B}{\delta X}$ is the on-resonance gradient of the X signal and ∂X is the RMS noise of the polarimeter signal after demodulation. The measurement of ∂X and a detailed discussion on noise sources is given in Chapter 5.

The magnetometer's ability to detect an oscillating signal is frequency dependent. The magnetometer bandwidth is defined here as the frequency range of oscillating fields that the sensor is able to detect. The ability of the sensor to detect a fixed amplitude oscillating field decreases at higher frequencies. The experimental procedure for measuring the bandwidth is outlined in the Appendix.

The power spectral density of the measured magnetic field will be presented in the following chapters. It is a useful metric for determining sources of magnetic noise, and its floor is often used to provide a sensitivity estimate. However, the spectral response exhibits a sharp roll-off that artificially distorts the sensitivity estimate at high frequencies. As a result, spectral data presented here has been rescaled by the measured bandwidth of the sensor. The recovered amplitude is normalised and the power spectral density divided by this rescaling factor.

It is in the interest of improving sensitivity to create a high atomic polarisation, decrease the rate at which the polarised ensemble decoheres, and collect as many probe photons as possible after interaction with the ensemble. In addition, the noise introduced to the system must be minimised. This is done by ensuring perturbations such as the laser and RF field are optimised, and by reducing noise on detection and in processing of the signal. The following chapters describe techniques to broadly tackle each of these components.

Chapter 3

The Shielded Experiment

This thesis describes experiments in two separate double-resonance setups, the shielded and unshielded experiments. The external cavity diode laser (ECDL) and spectroscopy setup is common to both. In configuration, the experimental setups are close to identical, with a single beam incident on a caesium vapour cell, with RF coils close to the cell to drive precession. This single beam-path configuration has been chosen for ease of scaling to portable setups. In minimising beam paths and equipment in the lab-based experiments, it is possible to more easily scale to portable sensors with miniaturised components.

Optically pumped magnetometers can achieve excellent sensitivity using an independent pump and probe configuration [52]. By pumping strongly on a different transition to that which is probed, high atomic polarisation can be achieved without equivalent power broadening of the probed resonance that would arise for a single-beam setup. However two-beam setups present a significant engineering challenge when scaling to portable sensors. In the shielded experiment, light powers below I_{sat} are used, low enough that power-broadening from the single beam is not a significant source of broadening in the magnetic resonance signal.

A single-beam setup has design advantages in both layout of beam paths and a reduction of optical components. Choosing RF field modulation as the double-resonance method avoids additional optical components such as acousto-optical modulators (AOMs) and electro-optical modulators (EOMs) required with an amplitude or polarisation modulation scheme [53, 54].

A controlled, magnetically quiet environment is ideal for testing effects inherent to the double resonance system, such as the angular dependence of

signal amplitude and phase [55]. The shielded experiment was built in order to understand effects such as these before transitioning to an unshielded environment where there is less control over the applied fields and field gradients. To date, the shielded setup has been used for investigating principles of magnetometry including orientational effects pertinent to double-resonance systems [55] as well as new operation schemes, such as vector magnetometry [56].

The atomic vapour cell is mounted inside a five-layer mumetal shield. Magnetic shielding reduces static and oscillating fields through two different methods. Oscillating fields such as those arising from the mains AC line are shielded by the skin effect, and static or low-frequency fields are “shunted” through a material of high permeability, essentially distorting the field lines around the area inside the shields. The efficiency of a shield is quantified by the shielding factor. This is the ratio between the field that would be present in the shielded volume and that which remains inside after shielding. The shielding factor for a cylindrical shield can be increased by its orientation with respect to the static field and its aspect ratio [57–59]

The shield comprises five layers of nested mumetal cylinders with end caps on the outermost layer. Each individual layer is wound axially with a degaussing coil. Degaussing brings each layer to magnetic saturation using a 5 Hz alternating current, with a maximum current of 0.5 A which decays exponentially to 1 mA over 12 minutes. This process can increase the shielding factor by a factor of 15 [59]. Degaussing is completed periodically, or after any changes in local magnetic field on the optical table due to movement of other equipment. The shield has an aspect ratio of 8:1 and is oriented in the North-South direction in order to best shield the geomagnetic field. Two small apertures 10 mm in diameter are in place for beam access in the transverse direction, as seen in Figure 3.1.

Two independent coil pairs in the Helmholtz configuration are mounted inside the shield and close to the cell in order to apply the RF modulation field, B_{RF} , on the x - and z -axes. The x -axis is along the long axis of the shield and the z -axis is orthogonal to both the long-axis of the shield and the laser axis, which can be seen in Figure 3.1. The signal to the RF coils is generated in software, and the signal and driving current are sent to the coils via a data acquisition system (DAQ)¹, (National Instruments PCIe-6353) with 1 MS/s

¹The data acquisition system (DAQ) used here incorporates an ADC; analog to digital

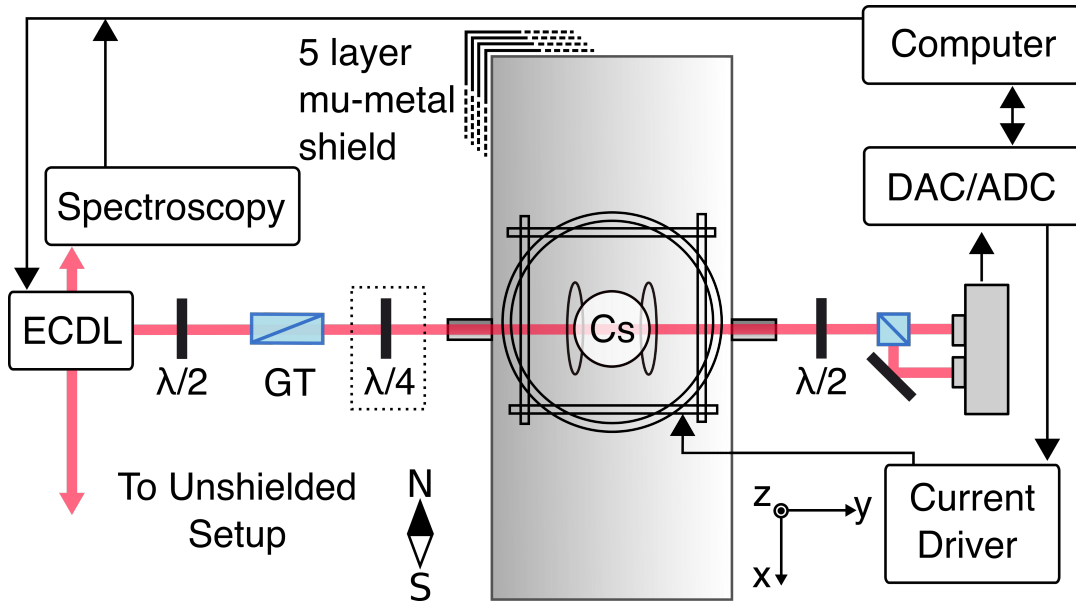


Figure 3.1: The shielded magnetometer experimental setup used in the following chapter. ECDL: external cavity diode laser; GT: Glan-Thompson polariser; Cs: caesium vapour cell; DAC: digital to analog converter; ADC: analog to digital converter.

read and write rates. Additionally a larger three-axis coil set comprising six independent coils is mounted within the shield, positioned such that the cell at its centre for static field control. These coils are controlled via a slower DAQ card (National Instruments PCI-6723). The signal from the slow DAQ to the coils is amplified and filtered using a custom coil current driver with a low pass filter with a -3 dB roll-off at 1 kHz [60].

An extended cavity diode laser (ECDL) is tuned to resonance with the caesium D1 transition at 895 nm, using an absorption spectroscopy setup as a reference. It became clear that the polarisation was important for the orientational effects described in Section 3.3. The polarisation was previously limited by a polarising beam splitter with an extinction ratio of 1000:1. The angular phase distribution shown in [56] exhibited a rotation around the vertical axis with respect to the modelled response prior to this improvement. A Glan-Thompson polariser cleans up the linear polarisation with an extinction ratio of 100000:1 after which a $\lambda/4$ waveplate is in place for the case of experiments using circular polarisation.

After exiting the shield, the laser beam is analysed by a Wollaston prism

converter, and DAC; digital to analog converter. From here on in, "DAQ" will be used when referring to reading or writing analog signals.

which splits the beam at a defined opening angle onto the photodetector. The Wollaston has an extinction ratio of 100000:1. The signal is read in to the computer via a commercial differential detector (New Focus large area photodiode 2307) with 40 dB common-mode rejection ratio and high bandwidth (up to 1 MHz). The data are read synchronously with the output of the RF field. The photodiode is read in via the fast DAQ card and the signal is demodulated in software at the B_{RF} modulation frequency, ω_{RF} . The two-beams incident on the photodetector have their optical power balanced by a half-waveplate which is manually adjusted while the laser frequency is tuned off-resonance to remove any effects of optical rotation.

A typical signal from the shielded setup is seen in Figure 3.2, which agrees well with the Lorentzian lineshape described in Section 2.5. The RF field is swept across a range of frequencies, and the field is generated so that the initial and final modulation phase is zero, and the sample time comprises an integer number of modulation periods. The total frequency sweep is separated into N discrete frequency packets which are phase-continuous with each other. The modulation is applied to the atoms and subsequently demodulated in software using the same frequency array. From the fit to the Lorentzian response around the Larmor frequency the parameters A , Γ and ω_L can be obtained.

In the shielded setup the atoms are optically pumped by addressing the $F = 4 \rightarrow F' = 3$ transition of the caesium D1 line, which can be seen in Figure 3.3.

3.1 Vapour Cells

The motion of the atoms in a glass cell has advantages and disadvantages for their use in detection of a magnetic field. The ballistic motion of an atomic sample at room temperature allows a polarised atom to pass through a small beam many times. As discussed in Section 2.3, increasing the coherence time of the atoms is favourable. Increasing the number of polarised atoms interacting with the beam increases the signal amplitude. A tricky interplay is increasing the amount of time an atom spends in the beam due to motion, and decreasing the number of wall collisions that cause depolarisation.

A collision with an uncoated glass cell wall by a polarised atom will result in a randomised polarisation after impact. A vapour cell contains atoms travelling

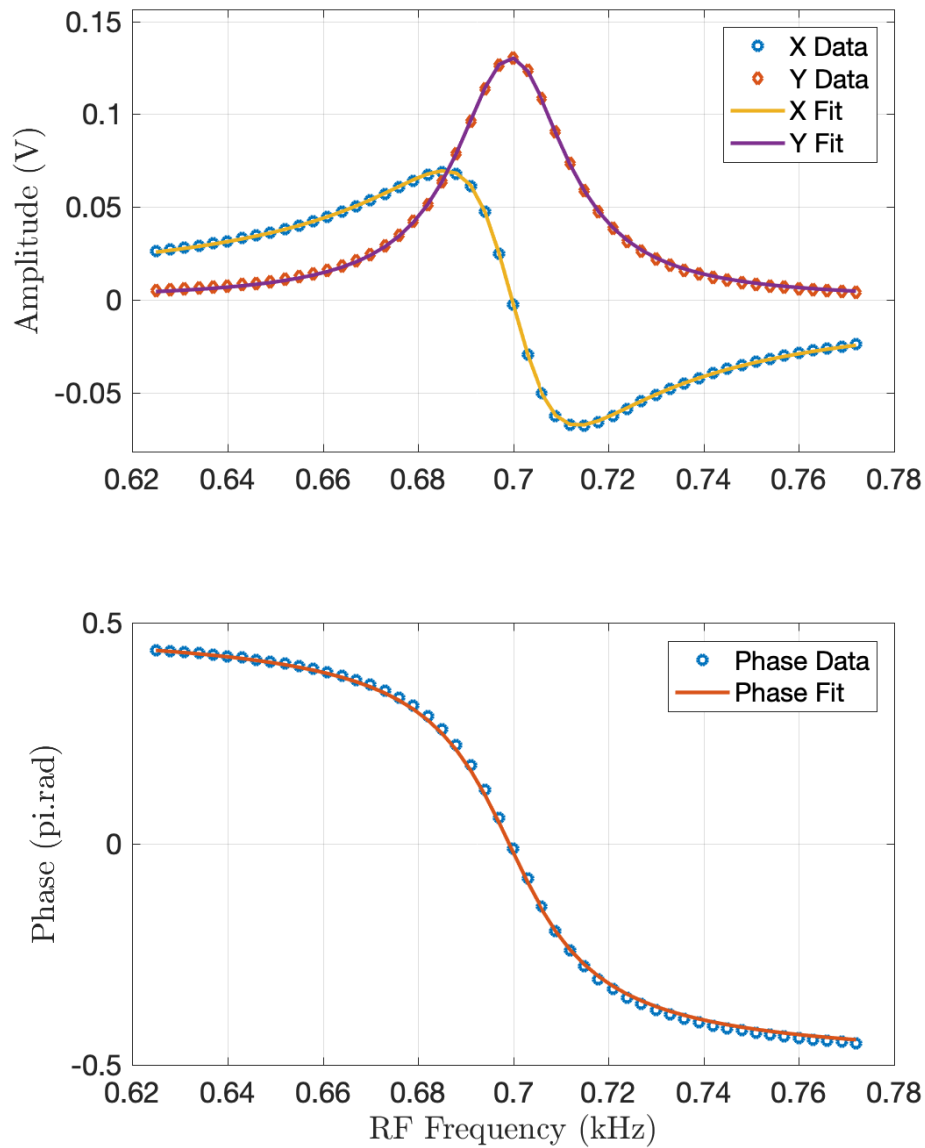


Figure 3.2: Top: In-phase (Y) and quadrature (X) components of the magnetic resonance signal around the Larmor frequency, including fits to X and Y. Bottom: Phase of the signal on resonance

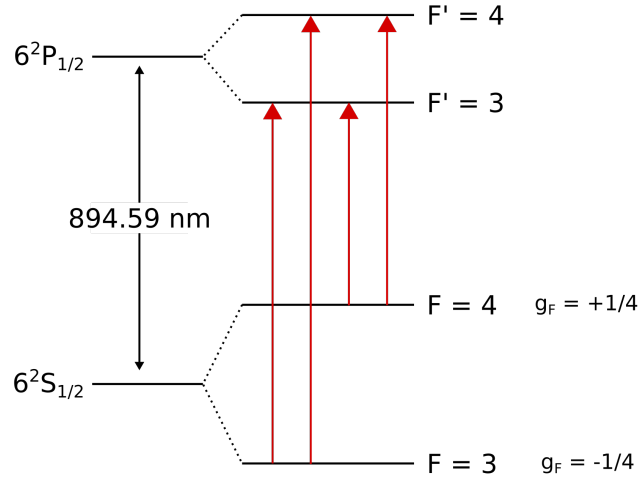


Figure 3.3: Ground and excited hyperfine level structure for the D1 line of caesium. Frequency splittings are not shown to scale. g_F is the Lande g-factor, given approximately here for the $F = 3$ and $F = 4$ ground states.

at a relative thermal velocity defined as the mean of the magnitude of the velocity of atoms in three dimensions:

$$\bar{v} = \sqrt{\frac{8k_B T}{\pi m}} \quad (3.1)$$

where k_B is Boltzmann's constant, T the temperature of the environment, and m is the atomic mass. For a caesium vapour cell at room temperature, $T = 20^\circ\text{C}$, $\bar{v} = 216$ m/s. For a spherical cell this results in a wall collision rate of:

$$\Gamma_{\text{wall}} = \frac{3\bar{v}}{4r}, \quad (3.2)$$

where r is the radius of the cell, here shown in Figure 3.4 to be approximately 30 mm. This results in a wall-collision rate, $\Gamma_{\text{wall}} = 1.08 \times 10^3$ s $^{-1}$. This broadening would significantly impact the sensitivity of the magnetometer, but can be mitigated by an antirelaxation coating [45].

Preserving atomic polarisation allows more atoms to be interrogated in the time before their polarisation is destroyed. Antirelaxation coatings can prolong the relaxation lifetime. Paraffin coatings allow approximately 10,000 collisions [45] by the atoms with the walls before the atom's polarisation is destroyed. This reduction in the decoherence rate results in a much narrower resonance in the NMOR signal - the atoms in the cell are pumped in the beam, leave the beam and collide several times with the walls, then interact



Figure 3.4: Glass cell of the type used here, photograph from Castagna et al. [46].

with the probe and cause rotation to be seen in the signal.

The spherical caesium cell used here was produced in the Weis group with a main bulb and attached stem containing a droplet of caesium. The stem ends in a capillary which leads to the main bulb. The inner surface of the spherical bulb has been coated with a paraffin antirelaxation coating [46].

Castagna et al [46] provide an in-depth discussion on the manufacture of the cells of the type used here. They measure the intrinsic transverse and longitudinal relaxation rates in a large sample of cells. The sensitivity achieved is $9\text{-}30 \text{ f}\Gamma/\sqrt{\text{Hz}}$ for these cells in a double resonance setup, limited mainly by the transverse relaxation rate arising from spin-exchange collisions between caesium atoms in different ground states and gradient broadening.

The sample study also looks at the longitudinal relaxation rate, which is dominated by relaxations due to collisions of the atoms with the stem opening or, to a lesser degree by imperfections on the paraffin coating. The rate of caesium-caesium collisions is given by:

$$\Gamma_{\text{Cs}} = n \sigma \bar{v}_{\text{rel}} , \quad (3.3)$$

where n is the density of the species, σ is the collisional cross-section, and \bar{v}_{rel} is the relative thermal velocity. Alkali-alkali collisions are either spin conserving or spin nonconserving, with a rate of spin-conserving or spin-

exchange:

$$\Gamma_{SE} = n \sigma_{SE} \bar{v}_{rel} \quad (3.4)$$

Spin exchange collisions occur in atoms which have two or more populated states in the ground-state manifold. In caesium the $F = 3$ and $F = 4$ ground state manifolds precess at the Larmor frequency with opposite sign, $\pm\omega_L$, having g-factors $\pm 1/4$, as discussed in Section 2.4. After a collision, one or both atoms may exchange hyperfine states, as described in [45]. The likelihood of exchange is bundled up in the spin-exchange cross section, likelihood of collision, and the broadening factor, q_{SE} . The spin-exchange cross-section σ_{SE} is $2 \times 10^{-14} \text{ cm}^2$ [45]. Similarly, the spin destruction rate is given by:

$$\Gamma_{SD} = q n \sigma_{SD} \bar{v}_{rel} . \quad (3.5)$$

Here q is the nuclear slowing-down factor. The spin destruction cross-section for alkali-alkali collisions, σ_{SD} , for caesium is $2 \times 10^{-16} \text{ cm}^2$, making spin-destruction an order of magnitude less likely than spin-exchange.

An atom traveling ballistically around the cell samples the whole volume of the cell between pumping and interrogation. Magnetic field gradients affect the detected signal; the probe has different precession frequencies imprinted upon it due to the different fields present in the cell, and this broadens the magnetic resonance. In addition, field gradients contribute to relaxation. The collision of atoms that are precessing at different frequencies introduces a phase shift to their precession, on further collision with other atoms this continues to dephase the sample [61]. Field gradients will contribute to the transverse relaxation rate, as they only affect the interaction between precessing atoms. The relaxation rate due to field homogeneities is defined as:

$$\Gamma_{grad} = (\gamma \Delta B_{RMS})^2 \tau_{wall} \quad (3.6)$$

where γ is the gyromagnetic ratio, ΔB_{RMS} is the value of the field averaged across the cell volume, and τ_{wall} is the mean time between wall collisions [46]. Castagna et al. have determined that in the batch of cells from which this one comes, spin exchange dominates assuming field gradients have been minimised [46]. The authors observed intrinsic relaxation rates of 2-6 Hz in these cells, extrapolated to zero laser power. Under optimal conditions relaxation rates of 7 Hz are typically achieved here. This is close to the intrinsic relax-

ation rate of the cell, and since the gradients have been reduced to 0.9 nT/mm [55], additional contributions to the FWHM are likely due to optical and RF power broadening.

3.2 Magnetic Field Control

The static field coils in both the unshielded and shielded setups have been carefully wound and calibrated to produce a homogeneous field; however, some corrections are inevitable. The coil winding is not perfect, even using a precisely-machined former, and the point at which the coil terminates at a twisted pair will introduce a small error to the field produced at the centre. The current supplied to the coils is corrected to account for this error, and the factor by which they are corrected is called the coil calibration factor, a . In addition to this permanent correction some stray DC fields will be present in the shield. For example, after degaussing the shield, residual DC fields arising from changes in distribution of magnetisation of the shielding are likely. A discrepancy then exists between the intended field and the measured response of the atoms. This can be seen by taking an “angle scan”, a series of resonance scans with an applied field, B_0 of fixed magnitude, applied at evenly distributed angles around a sphere with respect to the centre of the coils. B_0 is the intended field, that is, the current that must be sent to the coils to produce a desired field with the calibration values known at that stage.

The measured value of the Larmor frequency during each measurement in the angle scan gives B_{meas} , which can be plotted as a projection of the sphere onto a 2D Mollweide projection, as in Figure 3.6. The Mollweide projection maps the angle scan sphere representation to a 2D plot, with the equator a straight horizontal line and the central meridian along the centre vertical, with all other meridians distorted to fit in a 2:1 ellipse [62].

The vector by which the measured field, B_{meas} is different with respect to the expected field, B_0 is defined as ε . A three-axis calibration routine was developed to find the calibration factor for the coils and offset the remaining ambient field in the shield, described fully in [60]. This calibration routine applies a field with magnitude B_0 along each coil axis in turn. The field is varied by small increments δB_0 and the Larmor frequency measured. The measured response of the coils gives a straight line fit, $B_{\text{meas}} = a_i(\delta B_{0i} - \varepsilon) +$

B_0 which yields ε and a .

3.2.1 Iterative Optimisation Routine

Although the three-axis calibration improves the uniformity of the response over the 4π solid angle, the distribution of B_{meas} was still slightly anisotropic. In order to improve the isotropy and homogeneity of the measured field, an improved iterative optimisation routine was developed. The routine takes the previous dataset for the measured field magnitude in an angle scan where a desired field, B_0 was applied in every direction sequentially, and applies a nonlinear fit to the data.

The optimisation routine assumes the same calibration factor a and offset field vector ε . The expected field B_0 can be found by fitting to the ‘‘actual field’’, \mathbf{B}_A which is defined as:

$$\mathbf{B}_A = \varepsilon + \begin{pmatrix} a_x & B_x \\ a_y & B_y \\ a_z & B_z \end{pmatrix}, \quad (3.7)$$

and B_x , B_y and B_z are given by:

$$\begin{aligned} B_x &= B_0 \sin \theta_V \sin \theta_L \\ B_y &= B_0 \sin \theta_V \cos \theta_L \\ B_z &= B_0 \cos \theta_V \end{aligned} \quad (3.8)$$

where B_0 is the (intended) applied field magnitude. The angles θ_V and θ_L are the angles from the vertical and light axes respectively. This coordinate system can be seen in Figure 3.5.

The magnitude of the expected field is:

$$B_0 = \sqrt{(\varepsilon_x + a_x B_x)^2 + (\varepsilon_y + a_y B_y)^2 + (\varepsilon_z + a_z B_z)^2}. \quad (3.9)$$

The measured data is fit to this function. This fit is weighted by the variance of the measured field, σ , for each point, extracted from the resonance scan for each field direction.

The uncertainties on the fit are the square of the diagonal elements of the

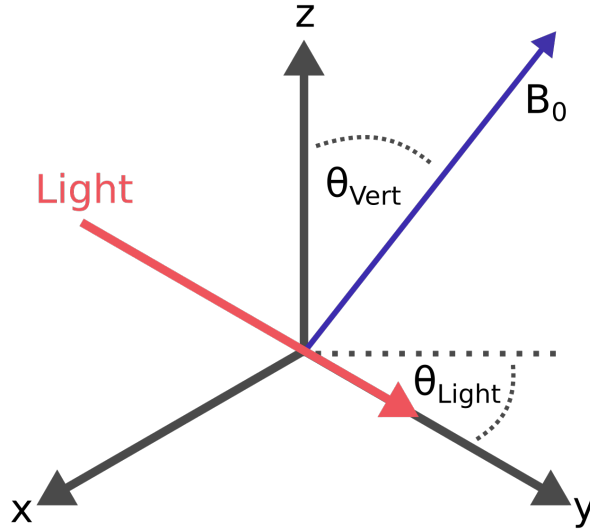


Figure 3.5: Coordinate system for the experiments described here. B_0 is the applied field, offset from the vertical z -axis and light y -axis by angles θ_V and θ_L respectively.

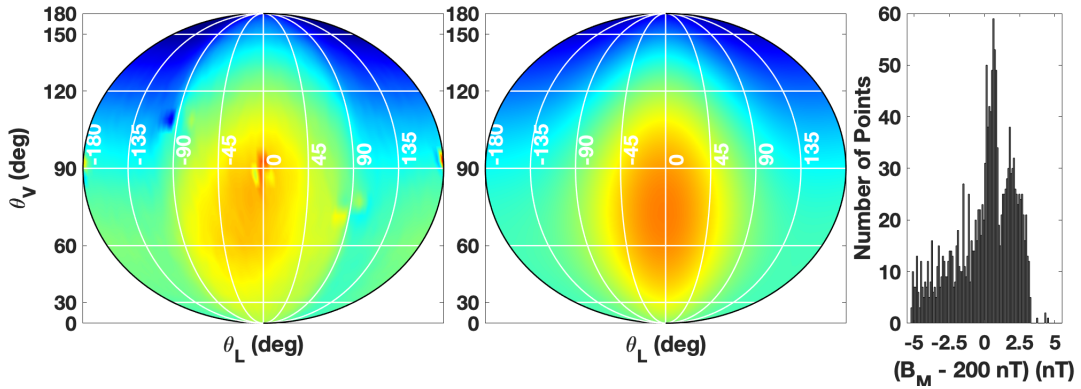
covariance matrix χ :

$$\chi = \frac{\Sigma(B_{\text{meas}} - B_0)^2}{\sigma B_{\text{meas}}^2} . \quad (3.10)$$

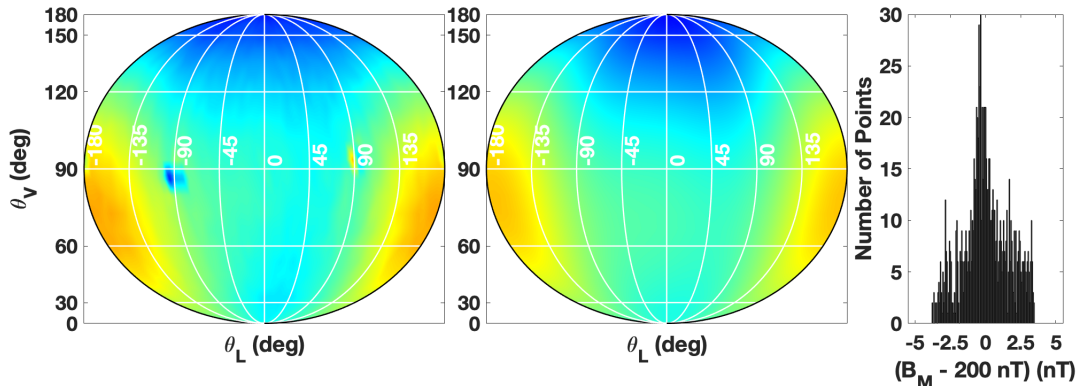
Once the free parameters have been found, they are fed back in to Equation 3.9 and plotted, as seen in Figure 3.6. The purpose of this is to check that the fit agrees with the data. A histogram plot is generated to allow qualitative analysis of the range and distribution of the inhomogeneities. This reveals asymmetries in the data. The calibration values for each axis are applied to the coil control software, which adjusts the current applied to each coil accordingly, and the next dataset is taken with an offset ε to the applied field. This process is repeated as necessary until the parameters approach the limits of uncertainty set by the field step size of the coil driver.

In order to show a clear progression from a poorly controlled field to a greatly improved one, the three-axis calibration and the iterative optimisation routine were applied and the resulting field homogeneity examined.

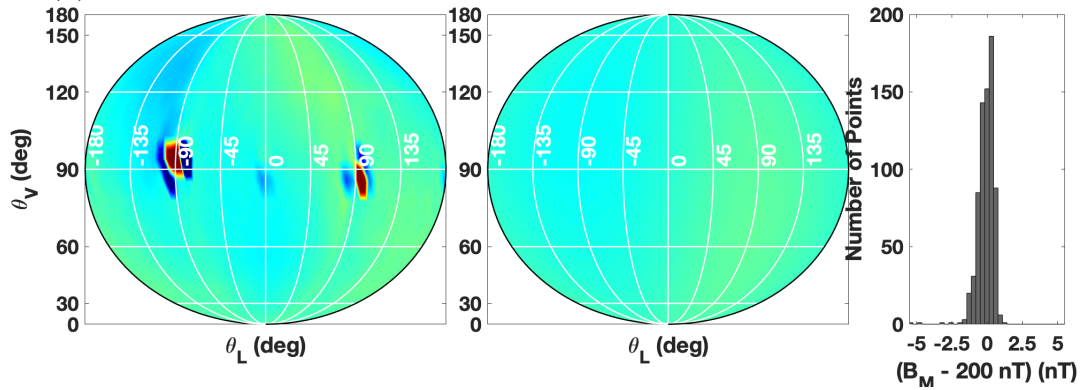
First the mumetal shield was degaussed, with the expectation that the coil calibration parameters that were correct prior to degaussing would have some offset after degaussing. A field of 200 nT was applied during an angle scan, and the value of B_{meas} measured, seen in Figure 3.6a. As expected, an anisotropic measured field magnitude is seen, as well as an asymmetric distribution, which is evident from the histogram. The fit to the field distribution



(a) Data, fit and histogram for the case where the shield has been degaussed, and no calibration has been applied.



(b) Data, fit and histogram after the three-axis calibration has been applied.



(c) Data, fit and histogram after the iterative optimisation routine has been applied.

Figure 3.6: The angular distribution of measured values of B_0 (left), fit to the data using Equation 3.9 (centre), and histogram of the distribution of field magnitude values.

from the calibration parameters reproduces the data well.

The three-axis calibration routine was run, and the calibration parameters applied. An angle scan was run, seen in Figure 3.6b, in order to assess the efficacy of this routine. Both the isotropy and the symmetry of the distribution around 200 nT were seen to improve. By minimising ε and correcting a for each coil axis the field magnitude is accurate to a tolerance of 0.94 nT. This describes the maximum uncertainty in the orientation of the applied field of 200 nT [60].

Finally, the iterative optimisation routine was run and the calibration parameters applied. There is a marked improvement in the isotropy of the field magnitude, seen in the results of the angle scan in 3.6c. The histogram spread is narrow and symmetric. The points at approximately θ_L, θ_V -90,90, and -90,-90 correspond to the dead zones where almost no sensitivity is observed. The iterative optimisation routine has yielded a mean measured field of 200.02 nT on an applied field of 200 nT. This has an associated field magnitude tolerance of 0.24 nT and an angular tolerance of 0.23 mrad.

As a result of the improvement to the field homogeneity it has been possible to measure the signal amplitude and phase with respect to angle of applied field with greater precision. This has led to a model that describes geometry dependent effects inherent to double resonance magnetometry in [55], as well as a vector magnetometry implementation benefitting from precise field control, as seen in [56]

Field gradients may be present within the shield due to inhomogeneous stray DC fields arising as described above. Due to the gradient broadening discussed in Section 3.1 contributing to a reduction in sensitivity, gradients in the shielded setup have been minimised.

The gradient minimisation routine uses the fitted relaxation rate of the resonance scan. A static field is applied to the atoms and then the gradient is swept in small increments. The resonance scan for each value of the field gradient yields a fit to Γ . The relaxation rate exhibits a quadratic dependence on the gradient, as shown in [60]. This parameter is minimised for each axis in turn, resulting in a relaxation rate of 7.5 Hz.

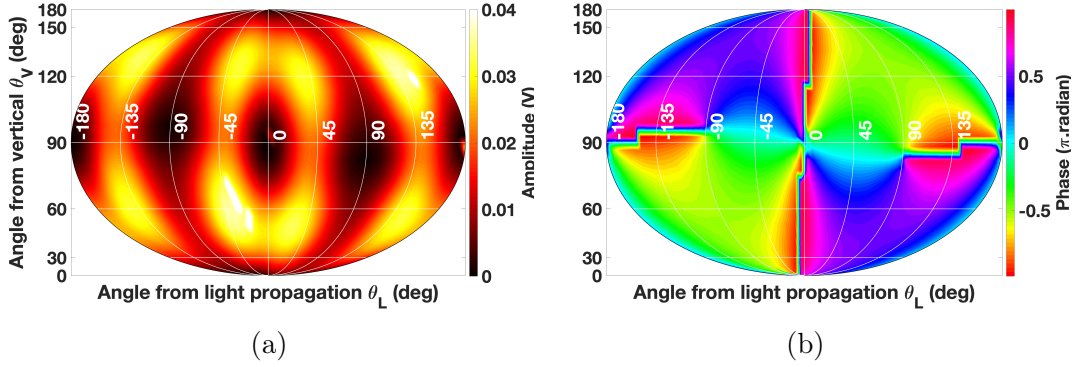


Figure 3.7: Angle scans showing the orientational dependence of signal amplitude, (a), and phase, (b) signals in the case of circularly polarised light creating an orientation moment.

3.3 Field Orientation Considerations

Double resonance magnetometers have a response dependent on the angle of the static magnetic field, B_0 , with respect to the light axis beam. For a fixed magnitude of B_0 , the Larmor frequency does not vary, but the amplitude of the demodulated signal changes as the angle of the field does. The magnetisation produced precesses with respect to the field with a response dependent on the moment created. Alignment and orientation moments produce distinct angular responses with respect to amplitude and phase.

The orientation moment is created by the interaction of circularly polarised light pumping the atoms into an oriented state as described in Section 2.2.3. Orientation is a rank-one dipole moment, whose angular momentum has a preferred direction. The orientation moment produces a cone-like response around the light-axis, which can be seen in Figure 3.7a. There are dead-zones, areas of zero sensitivity, along the axis of the light and at $\theta_L = \pm 90$ degrees, perpendicular to the light axis. The origin of this response has been well described in [55] using a multipole moment formalism, which will not be described here.

An alignment moment is produced in the case of linearly polarised light incident on the atoms. This is a rank-two quadrupole moment, with a preferred axis but no preferred direction. The population of the ground state magnetic sublevels for linear polarised light is described in Section 2.2.3, producing an alignment moment. This moment's response to the field direction produces two bright spots of sensitivity at $\theta_L = \pm 90$ degrees. There are two dead

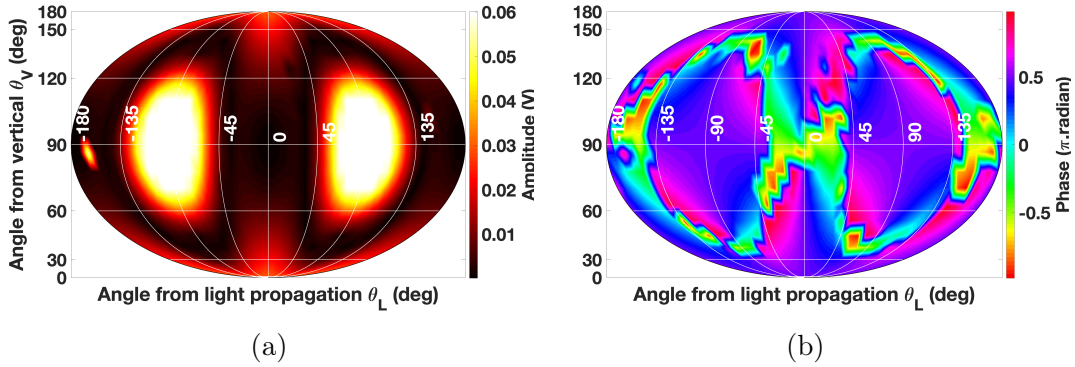


Figure 3.8: Angle scans showing the orientational dependence of amplitude, (a), and phase, (b) signals in the case of linearly polarised light creating an alignment moment.

zones that form a cone about these bright points, as can be seen in Figure 3.8a. The origin of the alignment angular response has been derived by Weis et al. [63].

Understanding the angular response of the double-resonance magnetometer is an important step in moving toward portable sensors. It is crucial that the magnetic field of interest does not lie along the axis of a dead zone of the sensor. Development of a vector magnetometer also faces challenges due to dead-zones [56].

The shielded experiment has served as a useful environment for testing effects in double resonance magnetometry and has yielded a greater understanding of the scheme. This has been invaluable in moving to an unshielded environment, detailed in the following chapter. The calibration routine described here has been implemented in the unshielded setup, and the precision achieved in the control of the field has led to further experiments in vector magnetometry and improved understanding of the way field orientation affects the signal amplitude and phase of the signal.

Chapter 4

The Unshielded Experiment

In the interest of investigating effects relevant to portable, unshielded sensors, the remainder of the work described in this thesis has been conducted outside of the shield. The unshielded magnetometer serves as a test-bed for optimisation and characterisation of miniaturised components and new techniques.

The experimental setup, seen in Figure 4.1, is a close copy of the shielded setup. There is no shielding around the sensor and the static field coils are larger, with an approximate radius and separation of 170 mm. The coil pairs have been built in such a way to provide ease of access for mounting and removing cells and additional coils. A home-built coil driver is used to amplify and smooth the current from the DAQ to the unshielded static coils. The driver is identical to the one described in Ingleby et al. [55], with operational amplifier OPA 549, in order to allow for a larger current step size.

4.1 Microfabricated Cells

As components of the magnetometer began to be miniaturised, cell size became a limiting factor. The glass cells described in Section 3.1 set a minimum sensor cross-sectional diameter of 30 mm. Building RF coils that are compact, yet produce homogeneous fields in the glass cells is a significant challenge. In order to make multiple sensors, more cells are required, and producing blown glass cells on a large scale is not within the expertise of this group. Producing silicon cells using standard microfabrication techniques allows compact cells to be made in a reproducible and scalable way. The cells

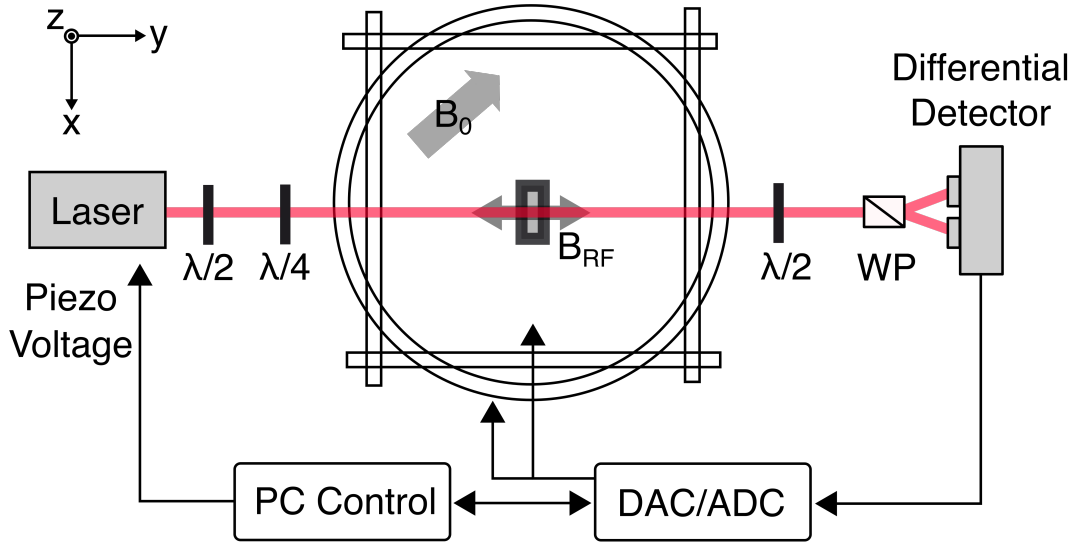


Figure 4.1: Schematic of the unshielded double resonance magnetometer. WP: Wollaston Prism

described in the following section are approximately 10 mm in their largest dimension.

Reducing cell size results in a greater number of wall collisions at a rate given by Equation 3.2. Buffer gas is used to reduce the frequency of collisions of the subject species with each other and the walls. The cells used here begin with an etched silicon wafer that is anodically bonded to two glass windows and filled with caesium azide, CsN_3 . Back-filling of nitrogen gas has been done to increase the nitrogen pressure in some cells. The cells are exposed to a UV lamp in order to dissociate the azide into nitrogen and caesium. The cells are characterised using absorption spectroscopy. This technique is highly scalable with good reproducibility [53].

The microfabricated cells used here have smallest inner dimensions between 1.5 and 2 mm, which alone would result in high relaxation rate due to dominant alkali-wall collisions. Wall collisions cause interrogation times to be much shorter. Buffer gas is used to suppress wall collisions, causing the alkali atoms to have a diffusive motion in the cell and alkali-alkali spin-exchange collisions to become the dominant source of broadening. Noble gases like argon and helium can be used, as well as nitrogen. An overview of the effects of different buffer gases has been produced by Pitz et al. [64].

One of the advantages of the large vapour cells described in Section 3.1 is the number of atoms interrogated due to the atoms' ballistic motion through

the beam. By slowing the alkalis with buffer gas, the number of atoms interrogated is decreased. Increasing the caesium number density increases the signal, and is achieved by heating. At a certain point either the relaxation rate due to alkali-alkali collisions dominates and the sensitivity decreases, or the atomic density causes the vapour to become opaque, meaning light transmission is decreased. This trade-off is described well in Scholtes et al. [65].

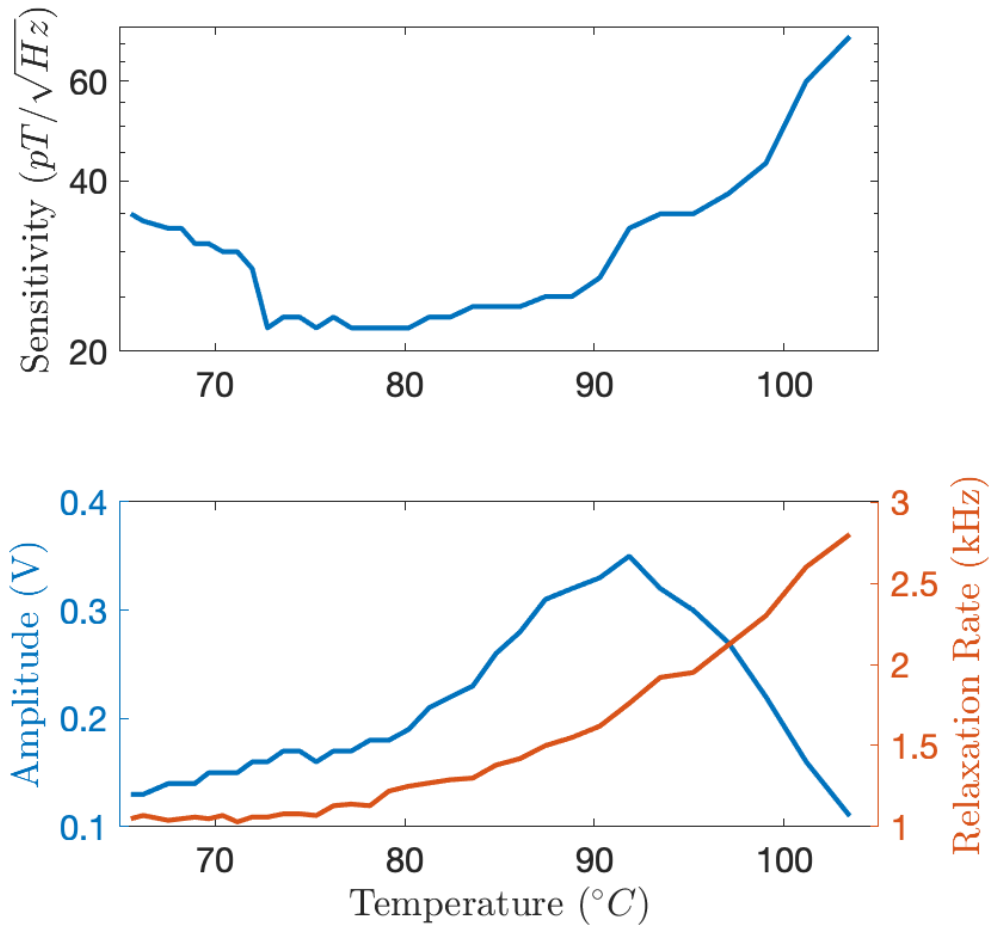


Figure 4.2: Top: Measured sensitivity of sensor in a magnetic resonance measurement with respect to cell temperature. Bottom: Signal amplitude and relaxation rate contributions to sensitivity as they vary with respect to temperature. The sensitivity (top) is calculated using Equation 2.61 in Section 2.7.

The response of the signal amplitude and linewidth to cell temperature can be seen in Figure 4.2. As the cell heats, the atom number increases, and so does the signal amplitude. The signal amplitude drops when the atom number begins to cause the cell to become opaque. The relaxation rate increases

steadily with temperature, more atoms in the cell means more collisions. The sensitivity has a wide, flat minimum, even with a few degrees temperature fluctuation, the sensitivity of the device is stable.

Another advantage of a smaller cell volume is that the system will be less sensitive to gradients. Typical linewidths for the cells used here are between 600 Hz and 1 kHz, so a magnetic gradient must be on the order of 100 nT/mm to contribute significantly to the linewidth.

A variety of microfabricated buffer gas cells have been used through the course of this project. Cells have been mounted on printed circuit boards that incorporate heating resistors, a thermistor and a printed RF coil, these can be seen in the schematic and photo in Figure 4.3. The cells have been glued to the resistors using thermal epoxy.

The printed circuit boards for cell-mounting have been designed to have a low power-consumption. By using a thin board with cutouts, a power consumption of 1 W is required in order to run at 80 °C. The low thermal mass of the thin board allows for a fast-heat up time. Fluctuations in cell temperature have been found to be due mainly to convection currents. The PCBs are mounted in lens-tubes, with the cells partially enclosed. This mitigates the main effects of convection cooling, further improving the power consumption.

Initially gated heating was used, where DC current through the heating resistors kept the cell at a steady temperature with feedback from the thermocouple. When a measurement was taken the heating was gated, that is, switched off for the duration of the measurement. This allowed the cell to stay hot enough for a few seconds. After this time the signal degraded as the atom density dropped. The gated heating meant that longer measurement times were not possible. The free-running measurements described in Chapter 5 prompted a need for continuous heating.

The cell heating in its latest configuration uses a signal generator and a broadband amplifier (Mini-Circuits ZHL 32+) to drive the heating resistors using AC current. Though this current creates a local magnetic field in the region of the cell, the amplitude has a mean value of zero. The atoms experience no DC magnetic field. The frequency is cell-specific, operating in the tens of MHz regime. This oscillating field is far outwith the bandwidth of the magnetometer (which is on the order of kHz), and is not aliased back in the the magnetic signal.

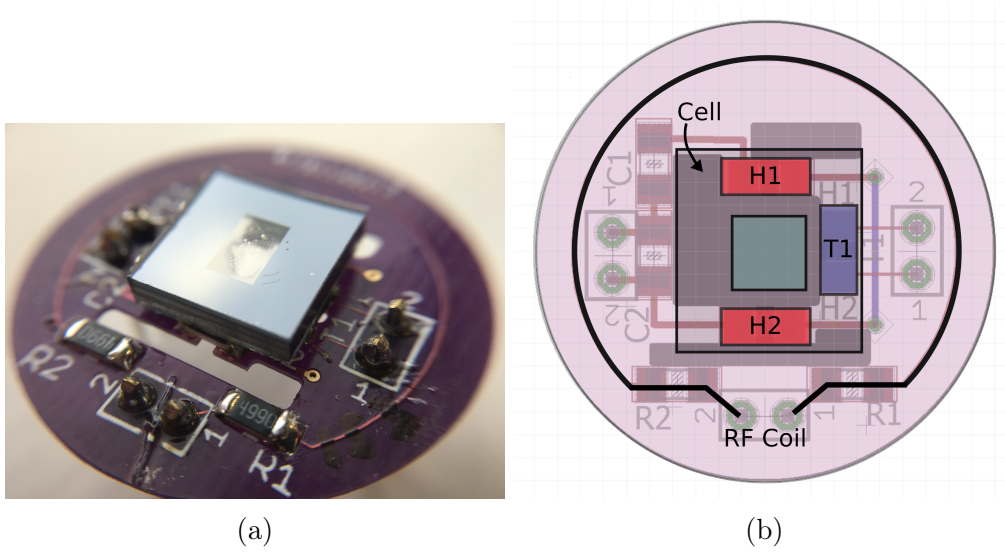


Figure 4.3: (a): Photograph of a microfabricated cell mounted on a thin PCB (b): Simplified schematic of the cell PCB. H1, and H2 are the heating resistors, and T1 is the thermistor. The cell is glued to these surface-mount components using thermal epoxy. The RF coil is integrated into the PCB and is controlled via the NI-DAQ system.

Another tactic to improve signal is to increase the path length of the cell. If the volume of the cell that the laser fills is longer and the atoms are slow with respect to the interrogation time, then the signal amplitude will be increased.

4.2 Magnetometry Considerations for Buffer Gas Cells

Heating the cell to increase the caesium density also increases the thermal energy and therefore the likelihood of collisions. Caesium-wall collisions are completely depolarising, however, the buffer gas causes the caesium to move with a diffusive motion and drastically reduces the number of wall collisions. The dominant interactions become spin exchange collisions between caesium atoms and spin-destruction collisions between caesium-caesium and caesium-nitrogen.

The relaxation rate due to buffer gas collisions is given by:

$$\Gamma_{N_2} = N_{N_2} \sigma_{Cs-N_2} \bar{v}_{rel} , \quad (4.1)$$

where N_{N_2} is the number density of nitrogen in the cell, \bar{v}_{rel} is the relative

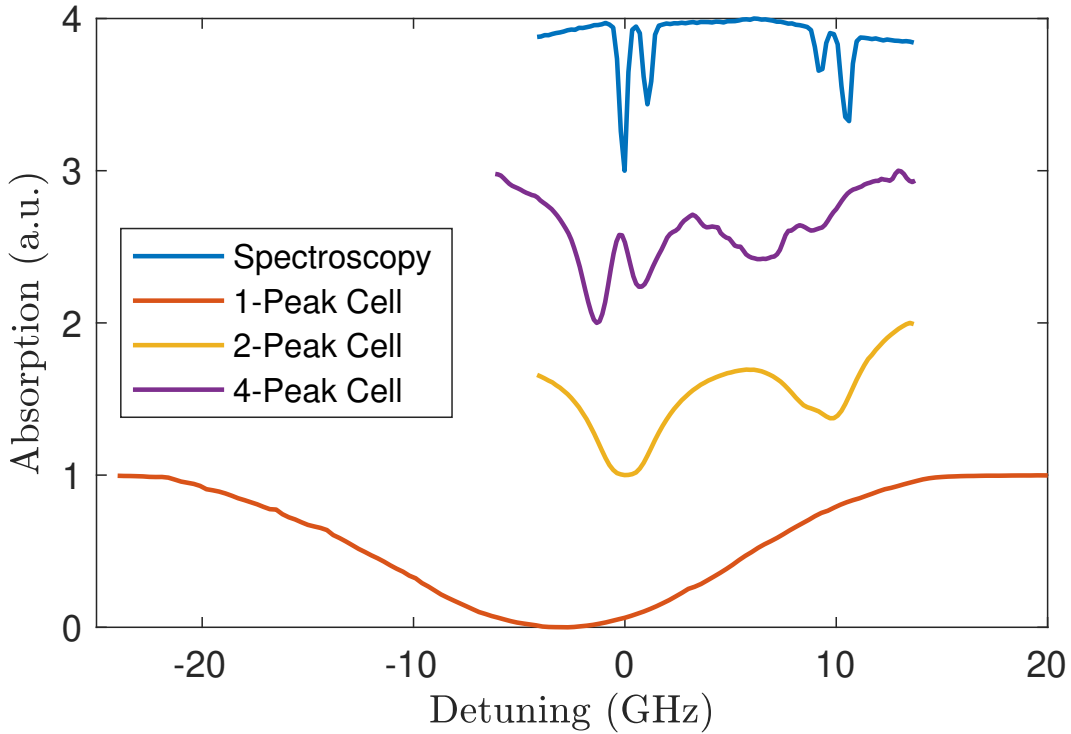


Figure 4.4: Optical absorption of three buffer gas cells of different pressures, plotted with respect to a Doppler-broadened reference cell (top).

thermal velocity between the two species, and σ_{Cs-N_2} is the cross-sectional likelihood of collision between a caesium and nitrogen atom.

Nitrogen molecules collide with the caesium atoms and broaden the optical lineshape. Collisional broadening is a homogeneous process and results in a broadened Lorentzian linewidth, which contributes to the Voigt profile described in Section 2.2.2. The absorption spectrum for the reference spectroscopy cell can be seen compared with buffer gas cells of different pressures in Figure 4.4. The cells used in this thesis have been classified by their absorption spectrum as one, two, or four-peak cells depending on the extent of their optical broadening due to their respective buffer gas pressures. The laser detuning scale has been defined with respect to the reference cell, where zero corresponds to the peak of the $F = 4 \rightarrow F' = 3$ transition.

As well as broadening the absorption spectrum, the buffer gas may induce a frequency shift. The collision-induced shift introduces a modified detuning to the optical spectrum, δ' which is the transition detuning modified by the induced shift by the nitrogen, δ_{N_2} [53]. The shift is dependent on the

buffer gas species and pressure. For nitrogen, a shift of -5.11 GHz/amg^1 is expected and the optical broadening due to nitrogen is 14.83 GHz/amg [66]. The effects of buffer gas broadening and shifts have been discussed in detail by Hunter [40].

The presence of nitrogen gas in the cell has two effects on optical pumping; collisional mixing, and quenching. Collisions between caesium and nitrogen cause collisional mixing in the excited states. As a result of this, a sample of atoms excited to any of the excited states $F' = 3$ or $F' = 4$ will relax back to both ground states isotropically, with a homogeneous population in $F = 3$ and $F = 4$. A pure stretched state in the m_F sublevels of $F = 4$ becomes difficult to achieve, as there is continuous repopulation of the $F = 3$ state. Further spin exchange and destruction collisions between the polarised atoms in $F = 3$ and $F = 4$ ground state serve to further decohere the sample, as described in Section 3.1.

The quenching effect of nitrogen can help to reduce radiation trapping. Collisions of excited state caesium with N_2 result in absorption of energy by the vibrational and rotational states of nitrogen gas [67]. Deexcitation of the caesium from the excited to the ground state can occur without a resonant photon being emitted. This minimises radiation trapping, a process by which a purposely polarised atom spontaneously emits an unpolarised photon, which further excites another atom into an unpolarised state [45]. Spin destruction between alkali and nitrogen occurs as given by the rate in Equation 3.5, with a cross section given by $\sigma_{SD}^{N_2} = 5.5 \times 10^{-22} \text{ cm}^2$. The probability of spin destruction with nitrogen is six orders of magnitude less likely than a spin destruction with another caesium atom. The broadening of the magnetic resonance lineshape due to the buffer gas is primarily a spin-exchange effect.

The quantity of buffer gas present in the cell has measurable effects on the magnetometry signal. In order to characterise cells that have been procured and understand some of the effects inherent to buffer gas cells, detuning scans have been used. The detuning scan routine automatically steps the laser frequency detuning through a range of values, taking a magnetic resonance scan at each detuning value. The parameters resulting from a fit to the magnetic resonance can be plotted with respect to laser detuning.

¹Amagat (amg) is a unit of number density used to describe the number of ideal gas molecules per unit volume, at standard temperature and pressure ($T = 273 \text{ }^\circ\text{K}$, $P = 1 \text{ atm}$).

The detuning scan for the one-peak cell can be seen in Figure 4.5. The fitted parameters; signal amplitude, relaxation rate, and Larmor frequency have been plotted, as well as the calculated sensitivity. Despite the single peak in the optical spectrum, there are two distinct local maxima in the magnetic response, as can be seen in the amplitude subplot. These regions likely correspond to the precession predominantly in the $F = 3$ and $F = 4$ ground state manifolds. In a broadened optical spectrum such as the one-peak cell, the excited states are unresolved and the laser light addresses two transitions instead of four. The rate of change in sensitivity with respect to detuning is small, and this suggests that this cell may be a good choice for a setup in which the laser is not necessarily highly stable. Small fluctuations in laser frequency (due, for example, to temperature fluctuations in an environment outside of the lab) will not correspond to large changes in the response of the sensor.

The two-peak cell shown in Figure 4.6 is moderately broadened and slightly red-shifted. This cell shows again two distinct local maxima in amplitude, though the highest signal amplitude is in this case found to the left hand side, on the side corresponding to the $F = 4$ ground state. There do appear to be four distinct peaks in amplitude, suggesting that there is partial resolution of the excited states. This would imply that the $F = 4$ ground state manifold can be polarised and probed from both $F = 4 \rightarrow F' = 4$ and $F = 4 \rightarrow F' = 3$ transitions. The relaxation rate dependence on detuning exhibits sharp features in its response, and their significance will be discussed further in the following section. The optimum sensitivity in this case is found at an optical detuning of approximately -2.5 GHz, to the left side of the peak corresponding to the $F = 4$ ground state.

The four-peak cell shown in Figure 4.7 shows similar amplitude dependence to the previous data, with four distinct peaks in the signal amplitude subplot. As in the previous cells, the Larmor frequency has several sharp dispersive features with respect to detuning. This has consequences for the accuracy of the field measurement. Small changes in laser frequency detuning may lead to large variation in the measured field. This cell shows the best sensitivity of the three cells discussed here, with a sensitivity on the order of tens of pT/ $\sqrt{\text{Hz}}$ around 8 GHz detuning. Although the signal amplitude is not maximised in this region, the low relaxation rate produces a steep slope in the magnetic resonance. It is interesting to note that the best sensitivity is

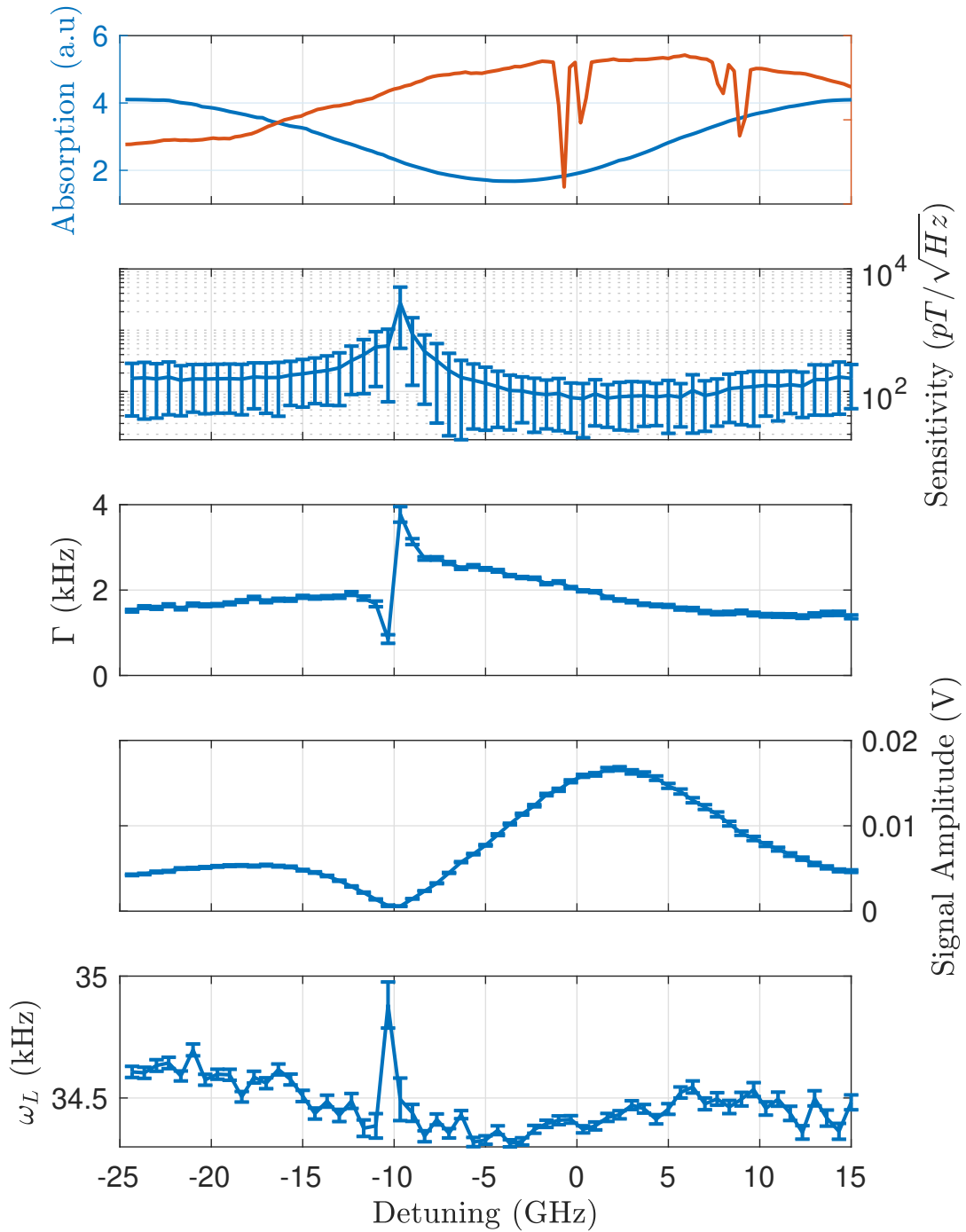


Figure 4.5: One-peak cell detuning scan. The parameters arising from the fit to the magnetic resonance for each detuning value are plotted; sensitivity, relaxation rate, signal amplitude, and Larmor frequency, with an optical absorption scan for reference (top). The reference cell absorption plot is shown in red and the broadened cell absorption plot in blue.

on the right hand side, corresponding to the $F = 3$ ground state manifold.

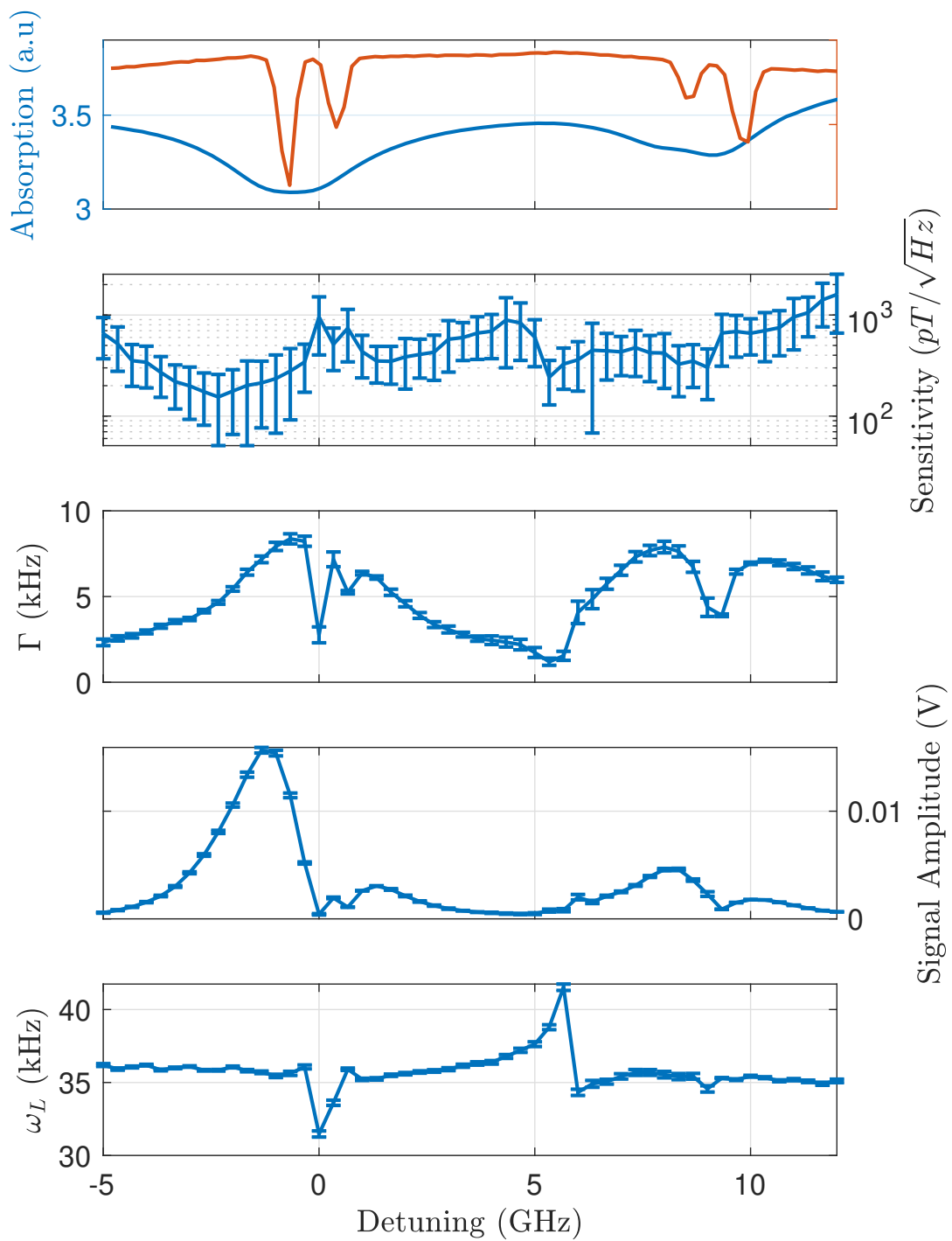


Figure 4.6: Two-peak cell detuning scan. The parameters arising from the fit to the magnetic resonance for each detuning value are plotted; sensitivity, relaxation rate, signal amplitude, and Larmor frequency, with an optical absorption scan for reference (top). The reference cell absorption plot is shown in red and the broadened cell absorption plot in blue.

This is a good demonstration of the wide variation in optimal operation parameters across the cells.

4.2.1 Light Narrowing

Light-narrowing is a form of spin-exchange relaxation suppression. Unlike traditional SERF magnetometry, light-narrowing can be observed at high magnetic fields in the range relevant for the work here. Light-narrowing suppresses spin relaxation due to alkali-alkali collisions with atoms in different ground states by shifting the population to one ground state [68].

Optical pumping with a single beam results in a single polarised ground state, but inevitably some population remains in the other ground state. In the case of an optically broadened cell, the spin exchange in the excited states results in equal probability of the population relaxing to each ground state. The spin-exchange collisions between the two ground state populations significantly broaden the magnetic response [65].

An optically-broadened cell allows a single beam to address both ground state sublevels of the $6^2S_{1/2}$ at once. If the laser is tuned such that the $F = 3$ state is strongly pumped, the atoms will be pumped out of the $F = 3$ state, after which collisional mixing redistributes into both ground states. By continuously pumping out of $F = 3$, the population in the dark state of $F = 4$ increases. This creates a stronger magnetisation due to greater population in the stretched state $F, m_F = 4, 4$, for the case where the light induces σ_+ transitions [8]. The pumping on the $F = 4$ state is moderate, leading to reduced power broadening than expected for the laser intensity [65]. In addition, the lower $F = 3$ population decreases the likelihood of spin-exchange collisions between ground states, narrowing the magnetic resonance linewidth. The increased amplitude and decreased linewidth can lead to significant improvements in sensitivity.

The process of exploring the parameter space with respect to detuning has yielded some unusually narrow resonances. The markers of light-narrowing are a reduced linewidth and increased signal amplitude.

In Figure 4.6 the relaxation rate response shows two sharp dips in each ground state manifold. These dips occur at the centre of broad local maxima. These sharp features might indicate light narrowing, but there is not a corresponding increase in signal amplitude simultaneously.

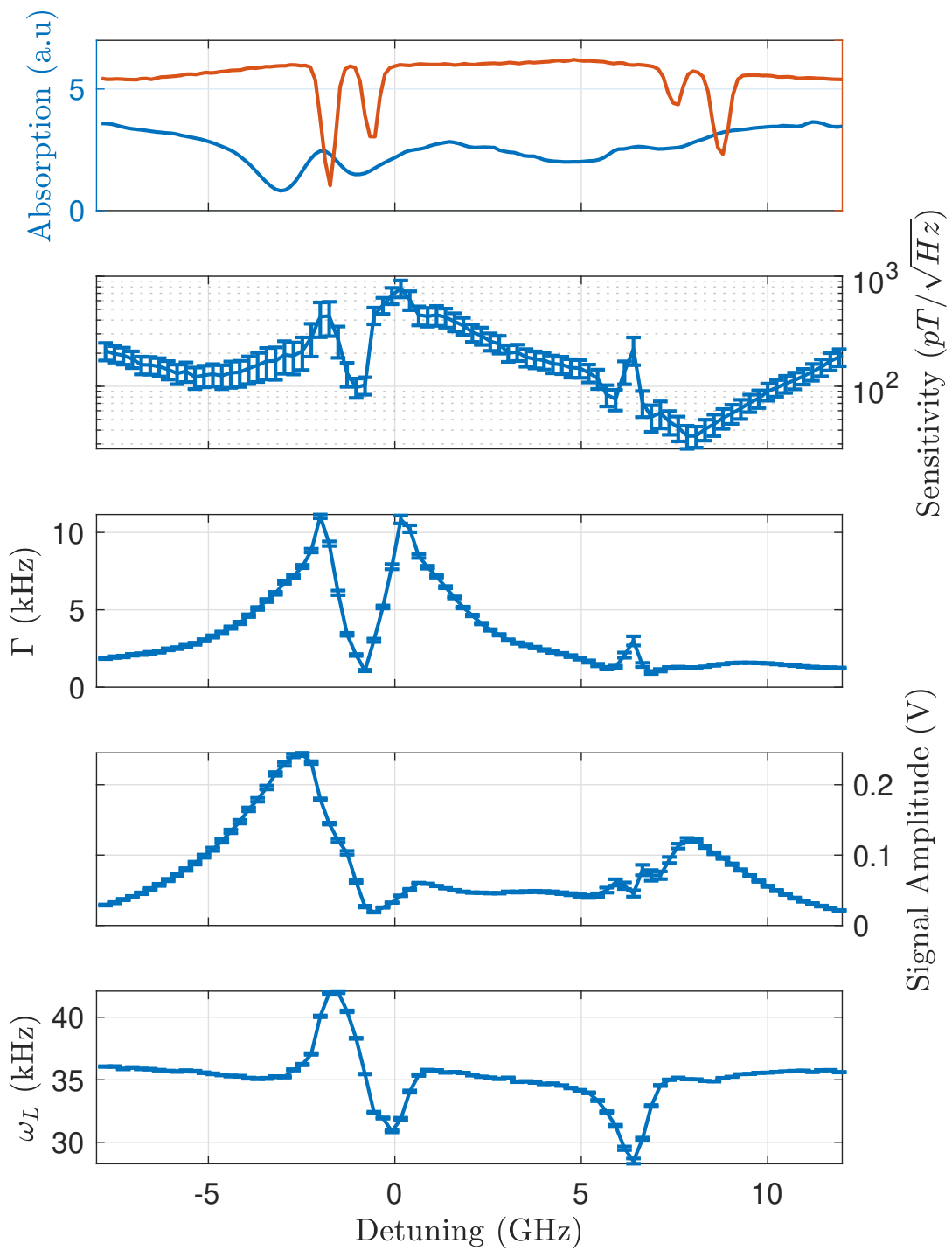


Figure 4.7: Four-peak cell detuning scan. The parameters arising from the fit to the magnetic resonance for each detuning value are plotted; sensitivity, relaxation rate, signal amplitude, and Larmor frequency, with an optical absorption scan for reference (top). The reference cell absorption plot is shown in red and the broadened cell absorption plot in blue.

Light narrowing is not obviously seen in Figure 4.5, with no distinct increase in signal amplitude, or decrease in relaxation rate. It seems likely that too much buffer gas causes collisional mixing at a rate that is higher than the atoms are pumped into a single state. Increased laser power may be required to display this effect in this cell.

It is favourable to seek out effects such as this that might yield advantages in sensitivity for the sensors here. Ultimately sensitivity is the parameter of interest. This effect may be useful in a lab setting with access to laser power on the order of 1 mW but may be limited in portable sensors where it is desirable to decrease power consumption. The investigation conducted here was brief, and conducted adjacent to cell characterisation work. Further work is required to definitively ascertain whether the light-narrowing mechanism is at play.

4.2.2 Alignment to Orientation Conversion

Alignment to orientation conversion describes the process in which linearly polarised light creates an alignment moment in the atoms, and this atomic alignment is subsequently converted to an orientation. The orientation moment can be detected after the probe has propagated through the medium [69, 70], and here can be identified by the change in angular sensitivity characteristic to each moment, as discussed in Section 3.3.

This effect can arise due to a number of factors. Alignment to orientation conversion has been induced by an electric field analogous to a Stark shift [71], magnetic field gradients, and anisotropic collisions between ground and excited state atoms [72].

In the case of Figure 4.8, angle scans have been taken across a range of laser detuning values. Linearly polarised light at $P = 75 \mu\text{W}$ was incident on the microfabricated cells, and resonance scans taken for angles of the static field across a range of angles. The expected angular response from these data was that of an alignment moment. However, the presence of orientation in the data became evident by the angular distribution of the signal amplitude on resonance. The expected angular responses for alignment and orientation have been produced with linear and circular polarised light in the shielded experiment, seen in Section 3.3. Linearly polarised light is expected to produce two bright spots at $\theta_L = \pm 90$, $\theta_V = 0$. Instead, an

orientation-like angular response was observed across the frequency detuning range.

At an incident power, $P = 500 \mu\text{W}$, the angular response is primarily that of an orientation moment, except in the case of a laser detuning of -2 GHz, where an alignment-like distribution is seen, and at -3 GHz, where a mixture of both is apparent in Figure 4.8. These alignment-like features occur on the low-frequency side of the peak corresponding to the $F = 4$ ground state manifold. Although orientation-to-alignment conversion has been demonstrated by other groups [73], the light in this experiment is linearly polarised. This should produce an alignment moment, but an orientation-like response is observed.

Were the alignment to orientation being induced by an AC Stark shift at high light power, the orientation moment should appear only in the high-power data. The opposite is the case here. It is unlikely also that there is a significant magnetic field gradient across a cell as small as this. It is unclear as of yet what mechanism is driving this effect. The small cell coupled with the presence of the buffer gas may be inducing collisional effects as described by [72].

Further investigation is necessary to determine the origin of the signal in these results. It is possible that the mixed signal seen at -3 GHz in the data at $500 \mu\text{W}$ could be beneficial for the minimisation of the dead zones inherent to each moment.

The unshielded experiment has served as a valuable testbed for integrating microfabricated components into the double resonance setup. The characterisation and optimisation of the cells discussed here has already contributed to other work on cell manufacture and portable sensors in this research group. The focus of the work on the cells described here has been to optimise for sensitivity, by increasing signal amplitude and narrowing the resonance width, as outlined in Section 2.7. The following chapter addresses sources of noise in the unshielded environment and their mitigation.

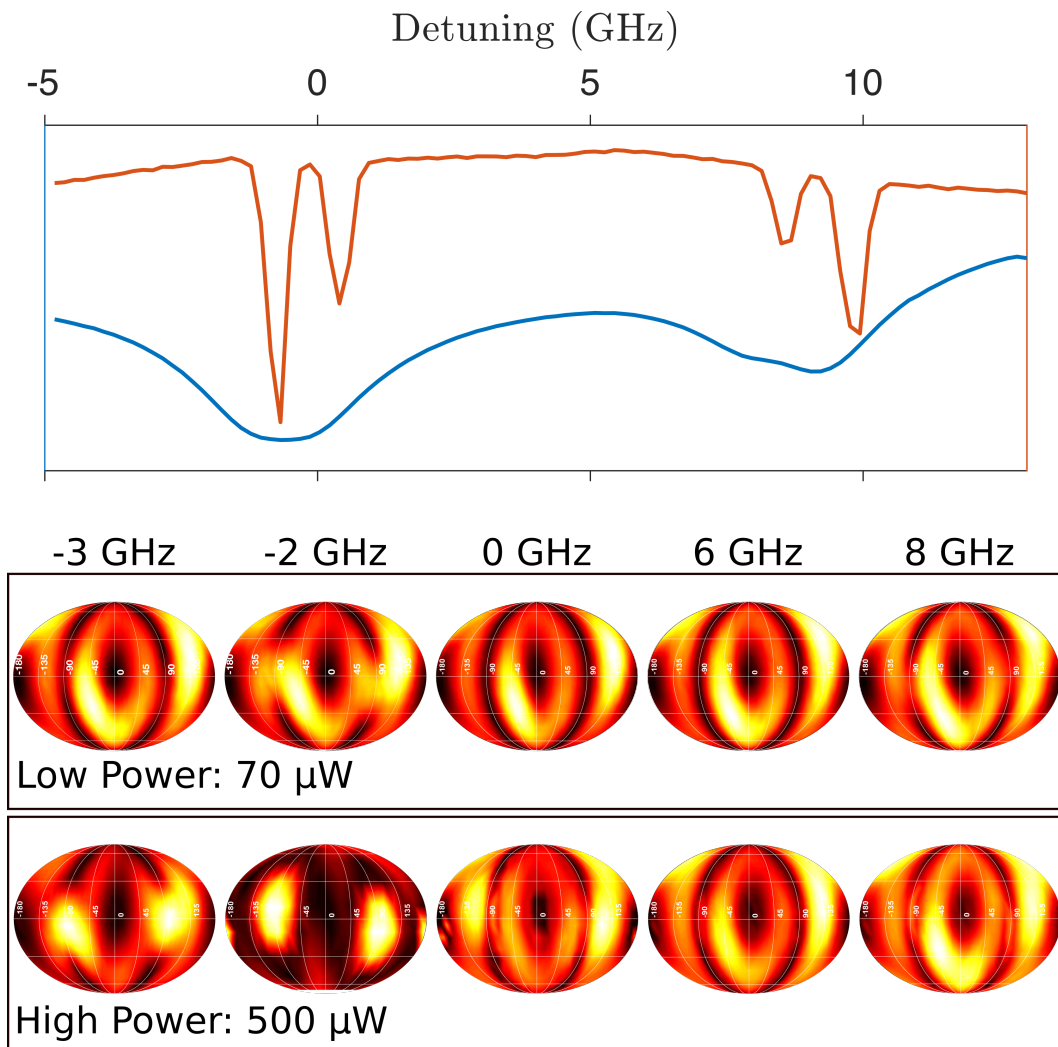


Figure 4.8: Angular distributions of magnetic resonance signal amplitudes, for values of laser detuning across the absorption spectrum of a two-peak cell. The angle scans have been taken at two laser powers, 75 μ W and 500 μ W. The angular axes of the angle scan plots have been removed for readability, equivalent axes for θ_L , θ_V can be found in Figure 3.7a.

Chapter 5

Noise Suppression

Building a magnetic sensor that operates in a range of unshielded conditions requires the ability to deal with a variety of noise sources. Some sources of noise inherent to magnetometry and detection methods have been described in Section 2.7, but the dominant sources of noise in the unshielded environment are magnetic and electronic noise. Magnetic noise arises in two ways; due to dense or ferromagnetic objects moving in the vicinity of the sensor, or by inductively-driven fields arising from current flow. The atoms are directly affected by magnetic noise as it modifies the ambient field they experience. Electrical noise arises in the control system of the sensor, with potential for noise pickup on the detection chain from the polarimeter to the computer, and in the outputs to the RF coil and static field coils, which is seen by the atoms as magnetic field noise. A schematic of the inputs and outputs of the sensor is shown in Figure 5.1.

The lab in which the unshielded experiment is built is quite a magnetically noisy environment. As well as the presence of extensive electrical wiring, many pieces of equipment are regularly switched on and off. Low frequency intermittent magnetic noise arises due to the magnetic door lock and highly magnetic desk chairs moving near to the experiment. This is all in addition to periodic noise arising from the mains AC line. An unshielded sensor must be capable of operating in noisy environments in order to work in an indoor environment such as this. As such, the focus of the following work has been to characterise and reduce noise inherent to the sensor such as electronic noise, while finding ways to operate in the presence of inevitable background magnetic noise.

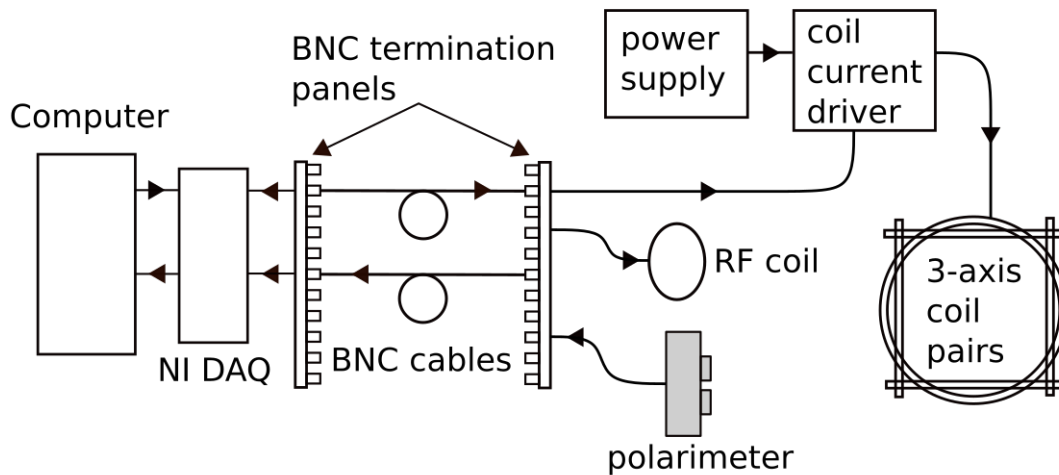


Figure 5.1: Schematic of connections between the sensor inputs and outputs with the control and readout system. The outputs to the sensor have the potential to introduce magnetic noise to the sensor, and the inputs to the DAQ and computer are susceptible to electronic noise coupling to the signal as it is read in.

5.1 Measurement-Induced Noise

The static and oscillating fields around the sensor are applied using the analog outputs from the DAQ. The RF coil is driven directly from the DAQ, and the static field coils are driven via a custom current driver and power supply described in Section 4. It is important that the fields applied do not introduce noise to the atomic ensemble. Significant effort has been made to ensure that the RF signals applied to the atoms are pure. Furthermore, any effects due to harmonics of the RF field will be averaged out in the lock-in detection scheme. For these reasons the noise from the RF source is not considered to be a significant contribution.

The static coil pairs have the potential to introduce magnetic noise if voltage noise is present on the input to the coils. The current driver has a 1 kHz low-pass filter, and the applied fields are kept constant throughout magnetic field measurements, but it is possible that white or low-frequency magnetic noise could arise due to the coil pairs.

To characterise the effects of electrical noise that may couple to the static field coils, various configurations were run; with the power supply to the coil driver switched off, the power supply switched on, and with an electrical

short physically applied across the coils. Finally, to test the DAQ itself, the input to the DAQ was shorted with a $50\ \Omega$ termination. This method assumes that all electronic noise arising from these sources couples entirely into the system magnetically via the coil pairs.

The current driver circuit is in series with a sense resistor across which the current to the coils can be monitored, and in this case read back to the DAQ. The voltage across the sense resistor was recorded for 10 seconds into an analog input channel of the DAQ, and the RMS average taken. The data are read in volts and converted to Tesla by the conversion factor for the z-axis coil. The conversion factor is found by determining the current required to achieve a field value as detected by the atoms along the z-axis, as described in Section 3.6. The resulting values from each noise measurement are summarised in Table 5.1. In the case of the measurement where there is a 50 Ohm resistor across the DAQ analog input, the signal is read directly from the analog input channel. As this factor gives a reproducible static field, the conversion will map to smaller values of field noise.

| Condition | Noise Amplitude (pT) |
|----------------------------------|----------------------|
| Power Supply Off | 2.64 |
| Power Supply On. 1V Output | 2.53 |
| 0 Ohm Resistor in place of coils | 2.65 |
| 50 Ohms across DAQ | 0.68 |

Table 5.1: Average values of measured voltage noise converted to magnetic noise using a conversion factor based on the coil calibration.

The static field coil pairs do not appear to act as an antenna for electrical noise in the system. When a 0 Ohm resistor is connected in their place, the measured noise through the system is not changed. Other components of the measurement chain being isolated also do not show any improvement, only by disconnecting everything and measuring the noise inherent to the DAQ system is there any detectable reduction in the electronic noise. This implies that noise in this measurement is due mainly to the system as a whole picking up noise in a busy lab. In this case, the signal from each measured component travels through approximately 3 metres of BNC cables between the sense resistor and the DAQ. If the assumption is made that all of the electronic noise that is possible to measure on the DAQ is transferred to the atoms via the coils, then the atoms will experience noise on the order of 2 pT RMS over a 10 second period. This is likely a worst-case-scenario estimation

of the magnetic noise introduced by the coils, but indicates that noise due to the lab environment is significant.

5.2 Detection Noise

The differential photodiode used in the unshielded experiment (New Focus large area photodiode 2307) measures two inputs from the beam that have been split by the Wollaston prism. By subtracting the signal from each port laser intensity noise is largely rejected and laser power fluctuations may be neglected as a source of noise after detection.

Figure 5.2 demonstrates the noise contributions from the polarimeter, the laser and the RF coils. The RF coils are included as a potential contributor in this instance due to the possibility of crosstalk between the RF signal and the signal from the detector. When taking readings from the polarimeter while it is powered off, it can be assumed that the voltage noise noise arises from the DAQ and electronic pickup from the BNC cables. The only spectral feature in this data which persists in the other measurements is a peak at 541 Hz. It is unclear what this feature is, and this requires further investigation.

When the polarimeter is powered on, for the remainder of the measurements the response is consistent with the specification sheet, with a broad peak at 150 kHz, which is stated as the 3 dB bandwidth of the sensor on high gain setting. This peak is unusual, the response of the detector is expected to roll-off as a low-pass filter, and this warrants further inquiry. Since the unshielded sensor operates in the frequency detection range below 100 kHz, this increase in voltage noise should not affect the noise floor of the sensor. The data in which the laser was not blocked were taken with the laser far from resonance. The laser being incident on the detector increases the noise floor by an order of magnitude and increased noise peaks in the 10-100 Hz region. For measurements with the RF field, the applied frequency was far from magnetic resonance. It was applied to the atoms during the measurement and also appears to cause an increase in the noise floor, with peaks in the 1-100 Hz range. It is possible that there is pickup between the RF analog-out and detector analog-in BNC cabling - the cabling system from the DAQ to the experiment is in its first iteration and is far from ideal. Pickup between channels will be carefully considered in future work.

The region of interest in the Larmor frequency, between 10 and 70 kHz is

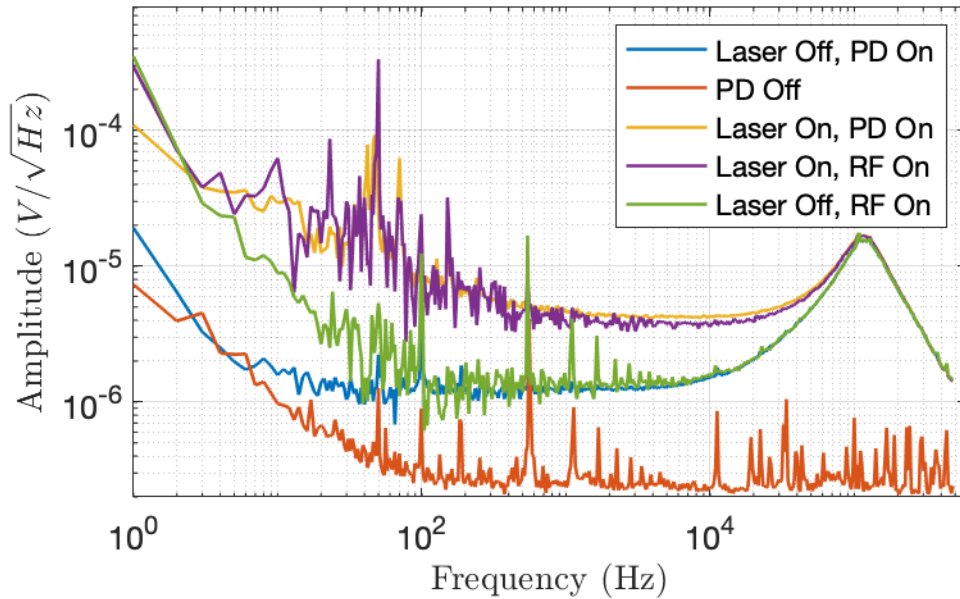


Figure 5.2: Power spectral density of noise contributions from sources that could contribute to detection noise. PD: Photodiode, here a differential detector.

flat, contributing no major oscillating signals. The noise floor in this region is between 4×10^{-6} and 9×10^{-6} $V/\sqrt{\text{Hz}}$ which is lower than the measurement of optical noise used to calculate the sensitivity as described in the following section.

5.3 Measurement Modes

The magnetometer can be run in different measurement modes depending on the RF field modulation that is applied. Up to this point, the resonance scan has provided a useful metric for improvement of the sensor. By sweeping the RF field frequency through the Larmor frequency of the static field, a single measurement of the Larmor frequency is taken to be the zero-crossing of the in-phase component. The magnetic resonance provides a mean value of the magnetic field over the period of a few seconds required to take the scan.

The resonance scan data comprises samples that have each been taken for a time period corresponding to an integer number of mains AC periods. This ensures that the Larmor frequency measured is an average of the field in the presence of the periodic field arising from the mains. Characterising the

| Condition | RMS Noise (V) | \sqrt{PSD} (pT/ $\sqrt{\text{Hz}}$) |
|------------------------------------|-----------------------|--|
| Laser blocked, B_{RF} on | 1.85×10^{-4} | 1.75(19) |
| Laser blocked, B_{RF} off | 2.28×10^{-4} | 1.46(75) |
| Laser on, B_{RF} off | 2.9×10^{-4} | 2.30(46) |
| Photon shot noise | 6.2×10^{-6} | 0.05 |

Table 5.2: Contributions to noise in the sensor arising from primary noise sources in the experimental setup. The sensitivity (\sqrt{PSD}) is calculated using Equation 2.61 for each noise value.

noise in this measurement mode is useful for making coarse changes to the system.

The noise on the resonance scan is calculated by taking the RMS average of the signal from the polarimeter. The noise measurement is taken for the same time period as the sample time of the resonance scan in question. No RF modulation is applied during this time, the noise measured arises only due to the laser and its interaction with the atoms while they are not being coherently driven.

Table 5.2 illustrates contributions to the sensitivity of the sensor as compared to the calculated photon shot-noise sensitivity. RMS noise was recorded for each condition for a 20 ms period and the equivalent sensitivity calculated using Equation 2.61. This gives an indication of the contribution of optical noise, RF coils and the DAQ system.

Monitoring the magnetic field over longer time periods yields information crucial to many applications. The time-varying magnetic field is particularly important in MCG and MEG measurements. In order to monitor the field as it changes in time, a single RF field frequency can be output close to the Larmor frequency. If the field and therefore Larmor frequency changes, the resonant response can be thought of as moving left or right along the frequency axis. The instantaneous value of in-phase component represents how far from the applied RF frequency the measured Larmor frequency is.

As the ambient field is tracked over time, so too are time-varying fields. The largest noise source in most environments is mains AC line noise at 50 Hz (the mains frequency in the United Kingdom), as well as activity in the lab and the building causing magnetic noise on short timescales. The feed forward technique described in the following section is one proposed solution to deal with periodic noise.

5.4 Feed-Forward Technique

1

Typically, environmental noise is dealt with by using passive shielding or active compensation. Passive shielding, which places the sensor inside a highly-permeable enclosure, is necessarily bulky, heavy and shields the sensor from signals of interest. Active compensation, through the generation of local magnetic fields opposing components of the environmental field, can be achieved either dynamically or statically using coils and low-noise current drivers.

Schemes have been implemented that modify the ambient field around the sensor in order to reduce magnetic noise [74]. Often an additional sensor such as a fluxgate is used to generate an error signal [75]. Within active compensation there are two broad categories; feedback and feed-forward. Feedback reacts directly to recent changes in the field [76], feed-forward uses knowledge of the environment to modify the response of the sensor in future measurements, thereby tracking large field fluctuations.

In order to implement a feedback system that is capable of tracking with the mains AC at 50 Hz, the feedback loop should operate at a much higher rate than the main noise frequency – a reasonable response rate would be 10 kHz. This is not possible with the current experimental setup due to the latency of the control system.

In the control system of the magnetometer, analog outputs to the sensor have been batched to improve run-time, requiring that the entire output voltage series is calculated and passed to a buffer before being output to the system. The sample rate of the DAQ used here is high, and all measurements have been hardware-timed, but the hardware communication (between the DAQ and the computer) is limited by bus latency. This affects latency in both directions; the samples being read in and the system response out. Algorithms required to process data introduce further latency. Although the throughput of the control system is likely high enough, the delay between signal and response is too long for fast feedback to be possible. This is a common issue in design of control systems for instrument feedback. Achieving a feedback rate this fast is typically done by using an FPGA (field-programmable gate array).

¹Parts of the work presented here expand upon published work found in the Appendix

FPGAs still have latency arising due to analog-to-digital conversion and algorithm run-time, but the computation is faster due to hardware execution, and they can run at rates as fast as $\approx 1\text{MHz}$ [77]. Future iterations of the sensor described in this thesis already have begun to utilise FPGAs for this purpose. These will be reported in future publications and PhD theses.

Feed-forward schemes have been demonstrated in configurations where a sensor feeds forward to compensation coils in order to cancel the ambient noise in the field [78, 79]. Full-field compensation is difficult to achieve without introducing additional noise in the environment. In this work an ambient field snapshot is fed forward to the sensor itself, modifying the RF field frequency to track the field more closely as it varies in time, thus ensuring that the magnetometer operates close to its maximum sensitivity throughout the noise cycle and stays in the linear regime of the response. No modification of the ambient field is done, only the RF field modulation is adapted to track the real ambient field more closely. Feed-forward can be advantageous if feedback is not implementable due to equipment latency and data transmission rate constraints. In addition, field compensation coils do not lend themselves well to future portable sensors.

The remainder of this chapter describes a feed-forward scheme that sequentially takes an unlocked measurement in the presence of noise and a feed forward measurement, by tracking the Larmor frequency in the same sensor. In a practical sensor it should be noted that oscillating signals of interest should not be present during the unlocked measurement. As such, the signal must be capable of being isolated, switched, or moved with respect to the sensor between the unlocked and feed-forward stage. Both measurements are started in phase with the 50 Hz AC line such that the feed-forward measurement phase matches the instantaneous magnetic field and the RF field frequency follows the Larmor frequency more accurately. Although feed-forward schemes have previously been implemented to control the ambient magnetic field [78], there appear to be no other feed-forward implementations that operate in the same sensor, or by feeding forward to the RF field frequency, thereby tracking the real ambient field more closely.

The experimental setup schematic of the unshielded double resonance magnetometer is much the same as that described in Chapter 4, with the addition of a small auxiliary Helmholtz coil placed within the field coils and around the cell.

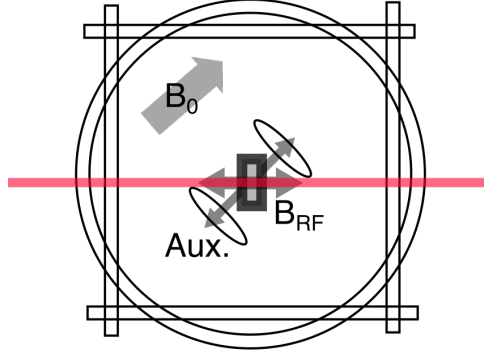


Figure 5.3: Schematic of the experimental setup for operation of the feed-forward technique. The experimental setup is as described in Chapter 4 with the addition of an auxiliary coil around the cell. The auxiliary coil is used to apply signals to the magnetometer during operation for subsequent detection. (Aux.: Auxiliary coil)

The feed forward measurement scheme comprises three distinct steps; a resonance sweep, an unlocked noise measurement, and a feed forward measurement. These are represented by their RF field modulation types in Figure 5.4.

The resonance sweep produces the data shown in Figure 5.5. By fitting to the in-phase (X), quadrature (Y) and phase components of the demodulated signal the parameters Γ , the relaxation rate; ω_L , the Larmor frequency; and A , the on-resonance amplitude can be calculated.

The fit functions, previously derived in Section 2.5 are as follows:

$$X = \frac{xA}{1 + S^2 + x^2}, \quad (5.1)$$

$$Y = \frac{A}{1 + S^2 + x^2} \quad (5.2)$$

where $x = \frac{\omega_L - \omega_{RF}}{\Gamma}$, $S = \frac{\Omega}{\Gamma}$, and Ω is the magnetic Rabi frequency. Measured and derived parameters relevant to the feed-forward scheme are tabulated in Table 5.3.

The sensitivity of the device in unlocked and feed-forward modes is frequency specific. The resonance scan in Figure 5.5 has a projected sensitivity of $2.91 \text{ pT}/\sqrt{\text{Hz}}$, where sensitivity is here estimated as the square root of the power spectral density (PSD) which is defined in Section 2.7, Equation 2.61. This gives an estimate of the magnetic noise the atoms are experiencing and

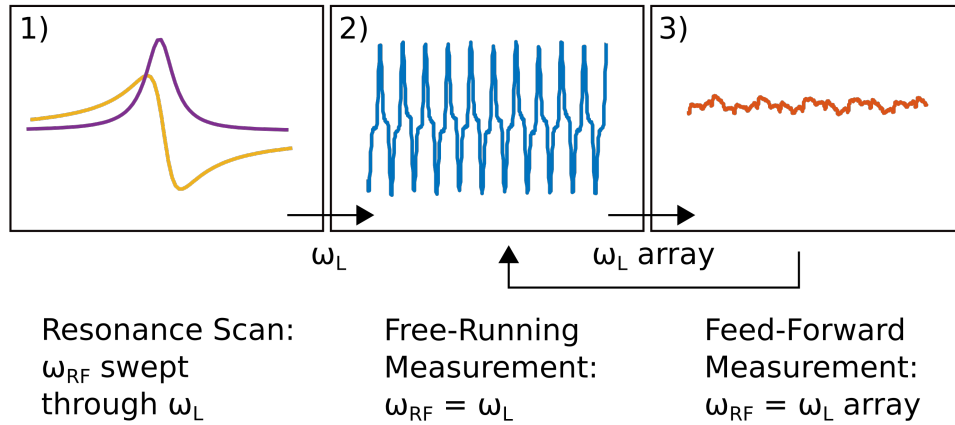


Figure 5.4: Flowchart indicating the three steps of the feed-forward process. The resonance scan, free-running and feed-forward measurements are done sequentially. The RF modulation frequency is shown for each stage of the scheme.

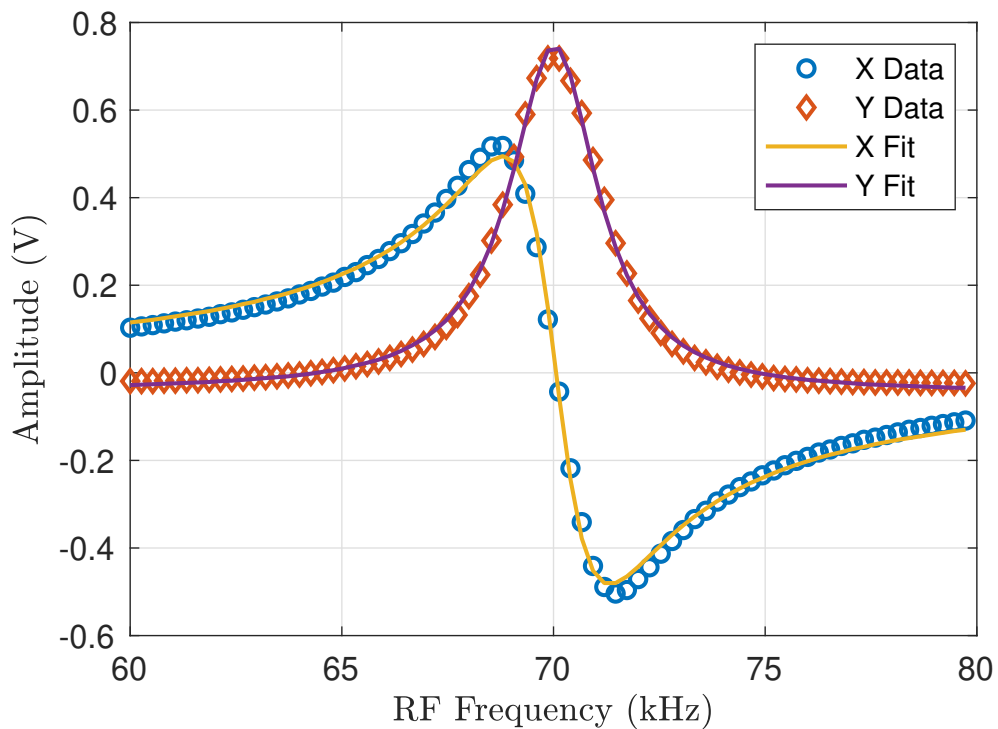


Figure 5.5: In-phase and quadrature components of the magnetic resonance signal for an applied RF magnetic field that is swept through the Larmor frequency.

transferring to the laser beam. This sensitivity figure reflects the ability of the sensor to resolve small changes in the field over the short measurement period of the resonance scan.

| | |
|---|------------|
| Larmor frequency, ω_L (kHz) | 70.049(11) |
| SNR | 4370(62) |
| Relaxation Rate, Γ (kHz) | 1.016(14) |
| Sensitivity, \sqrt{PSD} (pT/ $\sqrt{\text{Hz}}$) | 2.913(69) |

Table 5.3: Values of experimentally-relevant parameters derived from fits to the resonant response in Figure 5.5.

The measured Larmor frequency, ω_L , is then used in a free-running, or ‘unlocked’ measurement. The start of this measurement is triggered from the AC line. A constant RF field at ω_L is applied for a period of time and the response of the magnetometer measured. The polarimeter signal is demodulated at ω_L and the in-phase signal component (X) is converted to a magnetic field deviation using the fitted on-resonance gradient. This is a snapshot of the ambient periodic magnetic noise.

The in-phase response of the magnetometer is applied to the next measurement as a modulation of the applied RF field frequency. This measurement is also AC-line triggered in order to ensure that the phase of the 50 Hz line noise matches that of the previous measurement. The sensor has been found to more accurately track the ambient field when operating in this mode. The reduction of the noise amplitude maintains the magnetic signal in the desired linear operating regime. This can be seen clearly in the demodulated data in Figure 5.6. The RF frequency more closely tracks the Larmor frequency on the feed-forward measurement, corresponding to a smaller variation in the magnetic field amplitude.

The noise reduction can be seen more clearly in the spectral response, as seen in Figure 5.7. The power under the 50 Hz peak, in the range 45–55 Hz, is reduced by 22 dB, as well as the peak amplitude being reduced by a factor of over 500. The area under the peak at 100 Hz is reduced by 3 dB between 95 and 105 Hz, and the 150 Hz peak is suppressed by 21 dB between 145 and 155 Hz.

The peak at 22 Hz corresponds to building air conditioning units that are not in phase with the AC line. These units are directly adjacent to the lab and therefore the magnetic signal is large with respect to other noise

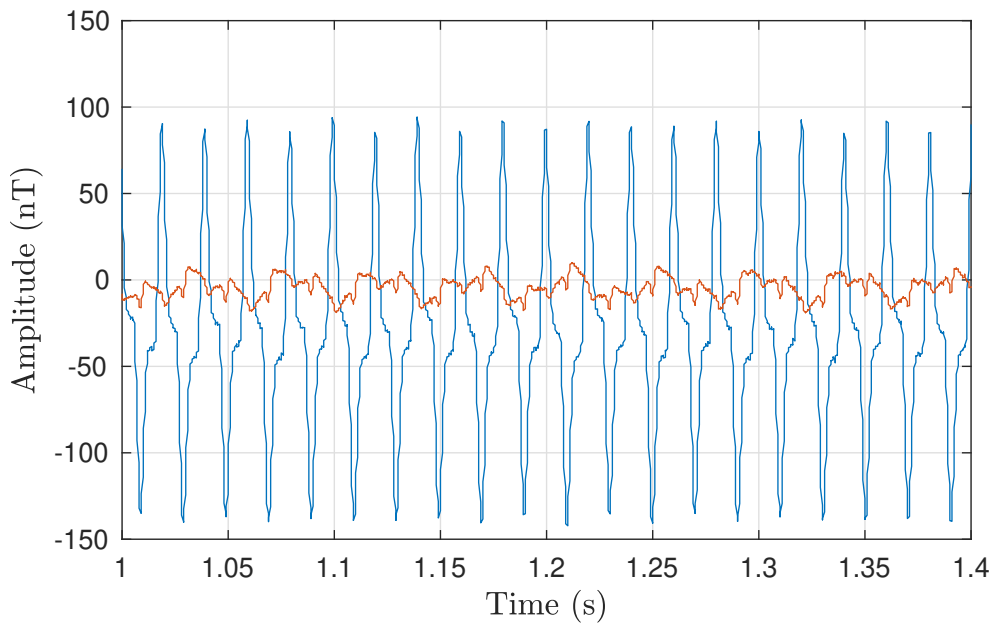


Figure 5.6: Segment of demodulated magnetic field data from a 6 second period in the unlocked, or free-running (blue) and feed-forward (red) modes.

sources. Air conditioning units are likely to be phase-stable with respect to the mains, however the phase of their signal is very unlikely to be the same at the first point of the unlocked and feed-forward measurements. The feed-forward routine does not suppress the noise from this source, and instead the noise at 22 Hz is increased. This will be the case with any signal not phase-locked to the mains signal present during both the initial unlocked and feed-forward measurements. This observation highlights both a limitation and advantage of this technique. Noise sources such as the air conditioning units are amplified, but so too are non-synchronous signals of interest.

5.4.1 Bandwidth Response

In order to test the noise cancellation technique in the presence of an arbitrary magnetic field signal, a small auxiliary Helmholtz coil pair was placed around the cell. The coils are aligned to the axis of maximum sensitivity of the magnetometer [55]. A function generator can apply arbitrary time-dependent currents to the coil during the unlocked and feed forward measurement stages. The magnetometer signal can be demodulated in software at the frequency of the function generator to recover the amplitude of the field. The coil was calibrated by applying a series of fields at fixed amplitude and increasing

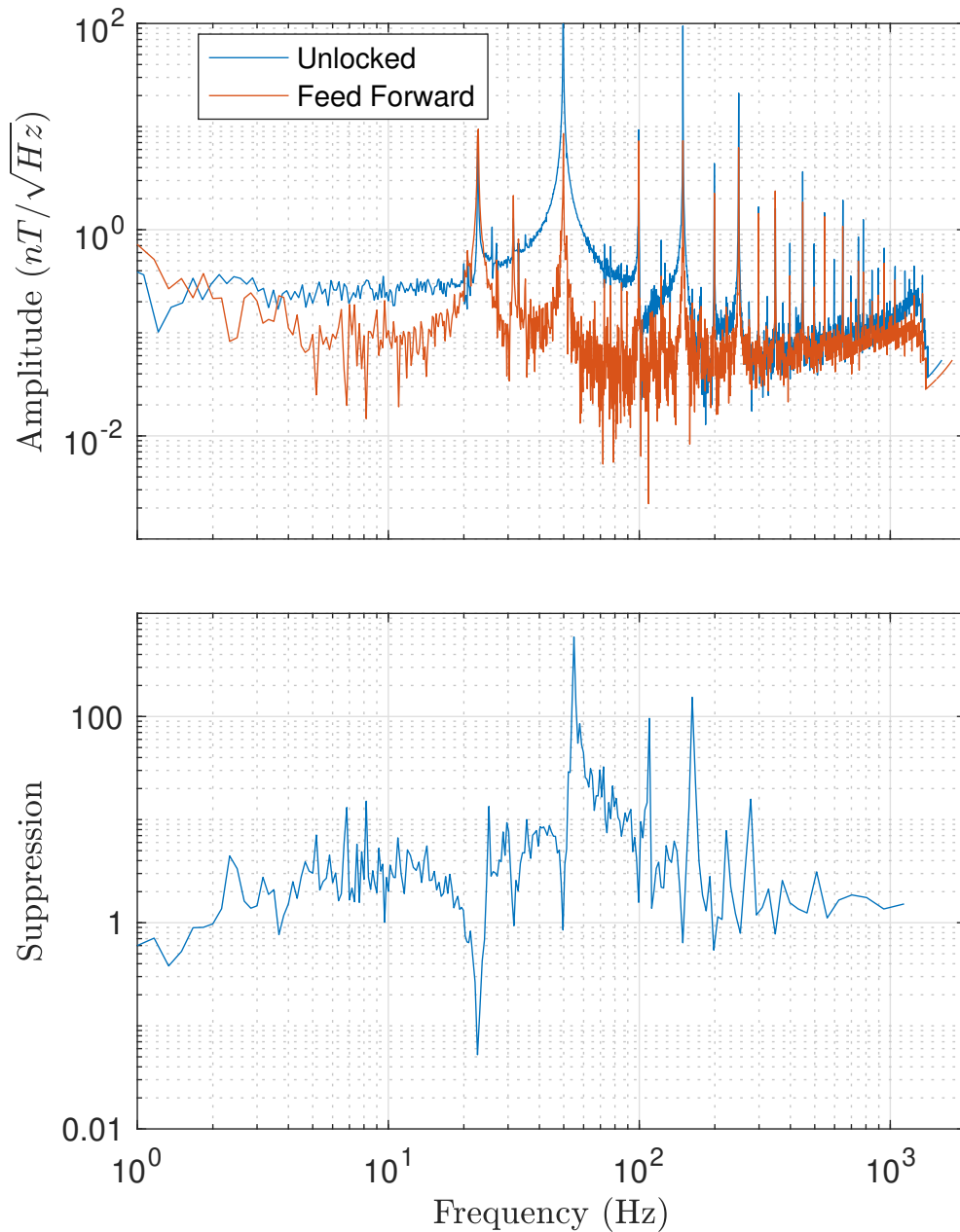


Figure 5.7: Top; magnetic noise spectra for the unlocked (blue) and feed-forward (red) modes. The power under the 50 Hz line and its harmonics can be seen to be reduced in the feed-forward mode. These data have been rescaled by the response of the sensor. Bottom; ratio of unlocked spectral response to that of feed-forward, showing ability of the feed forward technique to suppress noise across the a range of frequencies. In particular the peak at 50 Hz is suppressed by a factor of 500. Data have been rebinned into 500 logarithmically spaced bins for clarity.

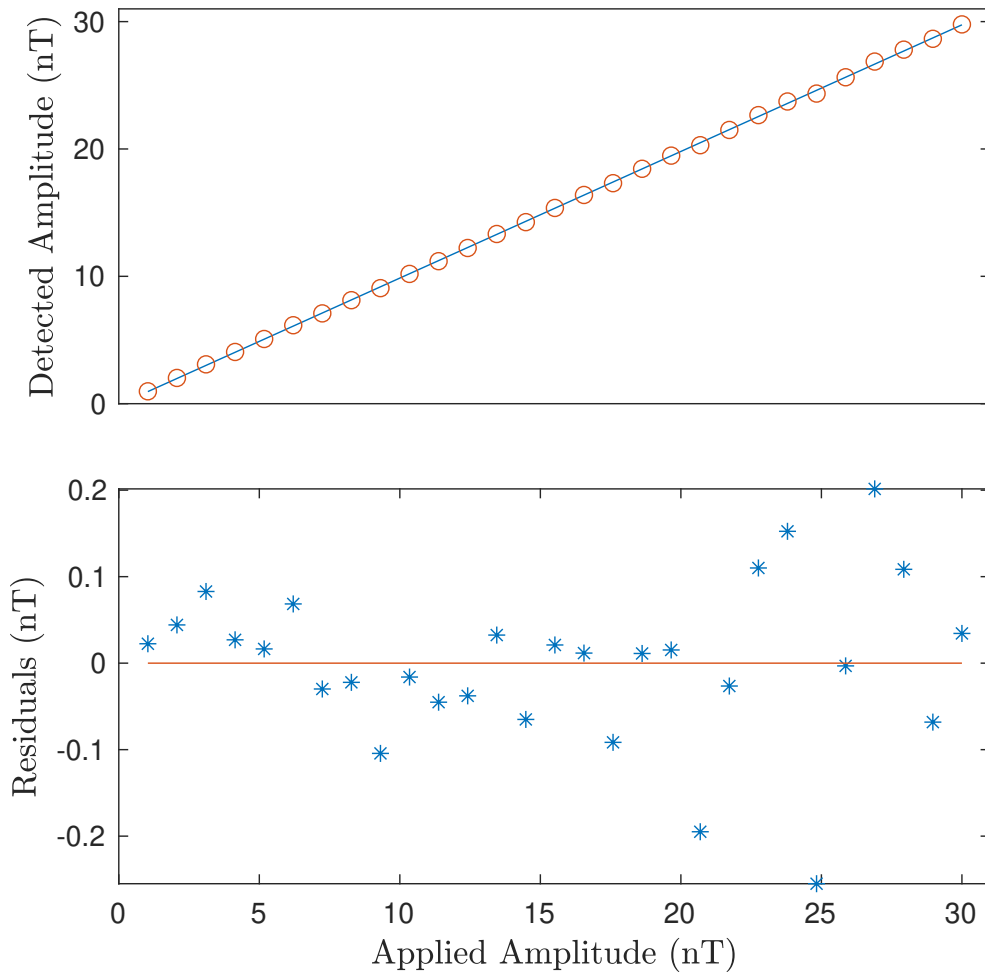


Figure 5.8: AC Calibration of the auxiliary coil around the cell. The straight line fit through the data (top) gives residuals (bottom), and is used to define the current-to-field calibration factor.

frequency to the magnetometer during the free-running measurement, and recovering the demodulated amplitude in software. The calibration results are shown in Figure 5.8.

Applying a known, constant amplitude oscillating field at different frequencies yields the frequency response of the sensor in Figure 5.9 from which the bandwidth of the sensor can be inferred to be 520 Hz (-3 dB cut-off). The expectation was that the response of the sensor would follow that of a low-pass filter, with a cutoff frequency given by the relaxation rate of the atoms. This is not the case for the response shown in Figure 5.9. Two distinct slopes can be seen in the frequency response. It is possible that there are two competing processes by which the response is damped. A phenomenological fit of two low-pass filters can be used, with orders of 1 and 7, corresponding to the

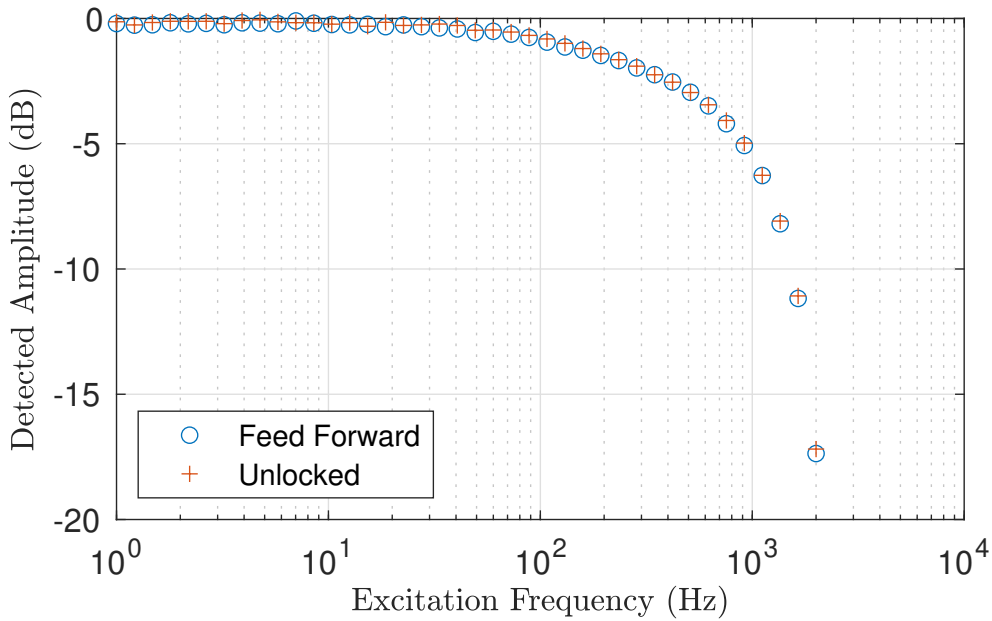


Figure 5.9: Response of the sensor to applied magnetic fields of a fixed amplitude. The response rolls off to a -3 dB point of 520 Hz. The response of the sensor is identical in the unlocked and feed-forward modes.

slope, dB/decade. While this works as a fit, there is no known mechanism for this response, and the implementation of a fit due to physical effects remains an open question.

The region up to 100 Hz is flat which demonstrates part of this scheme's advantage over a notch filter, which would necessarily attenuate signals of interest in its band. It should be noted that the measured response function has been incorporated into the calculation of the magnetic noise spectrum in Figure 5.7.

The response of the sensor to applied excitation fields is identical in the unlocked and feed-forward modes, rolling off to a bandwidth of 520 Hz, which is compatible with the pressure-broadened vapour cell used. The cell in question has a fitted resonance linewidth of between $\Gamma = 600\text{--}800$ Hz. The linewidth depends strongly on the operational parameters discussed in Section 4.1.

5.4.2 Signal Recovery

As a proof of principle, a simulated cardiac trace was applied to the auxiliary coil in place of the sine waves applied for calibration purposes. The data in Figure 5.10 shows the main features of the cardiac trace preserved in

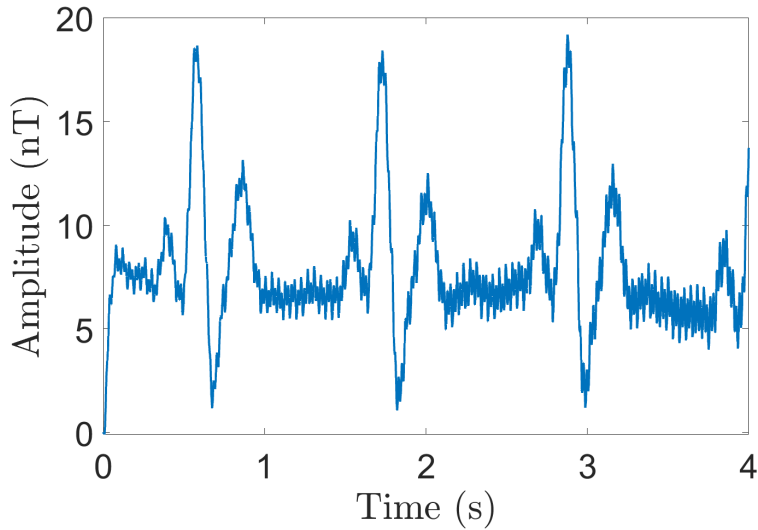


Figure 5.10: False cardiac-like trace applied to the auxiliary coil over the course of a feed-forward measurement, with a peak to peak amplitude of 15 nT

the signal, with appropriate timing and amplitude preserved. Of course, 15 nT field amplitude is far from the expected amplitude (approximately 50–100 pT) of a real mammalian heartbeat [80, 81], but this measurement demonstrates that arbitrary waveforms may be applied and recovered in the feed-forward mode. It would not be possible to resolve a 15 nT cardiac signal with this clarity in the presence of the ≈ 200 nT mains AC noise in the unlocked mode. Cardiac measurements could benefit from this noise suppression technique due to the nature of the measurement. The initial feed-forward snapshot could be taken, and then a subject moved to the sensor, and the cardiac magnetic response measured.

Although the results shown here focus on mains AC noise, this technique is readily implementable in any scenario that presents periodic magnetic noise. Foetal magnetocardiography provides a possible example. A foetal magnetocardiogram measurement may in theory be triggered from the mother’s electrocardiogram, allowing her heart’s large amplitude magnetic signal to be suppressed and improving recovery of the foetal heart rate.

The steps for optimal noise suppression in a magnetometer are context-specific. Some noise is inevitable in the unshielded environment, and ideally a portable magnetic sensor should cope with a variety of noise sources. This

chapter has presented attempts to minimise technical noise inherent to the sensor, but the challenge to sensing in the presence of large external noise sources remains. The feed-forward technique presents one avenue for operating in large amplitude periodic noise without filtering and without fast feedback. This software routine is easily implementable in any magnetic sensor. The following chapter will address further work on noise suppression from a hardware design perspective.

Chapter 6

Gradiometry

The feed-forward technique described in the previous section has been successful in suppressing periodic noise, but many other non-periodic noise sources remain, which continue to be a challenge for unshielded magnetic sensors. Magnetic gradiometry uses the principle of common mode noise cancellation to subtract noise that is common to two magnetic sensors. This chapter will describe two magnetic gradiometry experiments, one built around the microfabricated cells discussed in Section 4.1, and the other using the glass paraffin-coated cells described in Section 3.1.

This chapter describes an investigation that began shortly before the lab shut down at the end of March 2020, due to the COVID-19 outbreak, and some of the data presented are very preliminary. There was a narrow window in which to take measurements, and the datasets are not as rigorous or as well understood as would be ideal. However, the results presented here are promising and offer a good starting point for future investigations.

6.1 Common-Mode Noise Cancellation

The principle of common mode noise cancellation lies in the measurement of a system in two physical locations. The measurements must be made close enough that ambient noise is common to both, but far enough that a localised signal may be distinguished by one measurement location. The subtraction of the two measurements eliminates global environmental noise common to both and leaves only the differential measurement [82]. The baseline is defined as the distance between the two measurement volumes. Some magnetic gradiometer schemes use two individual sensors to achieve

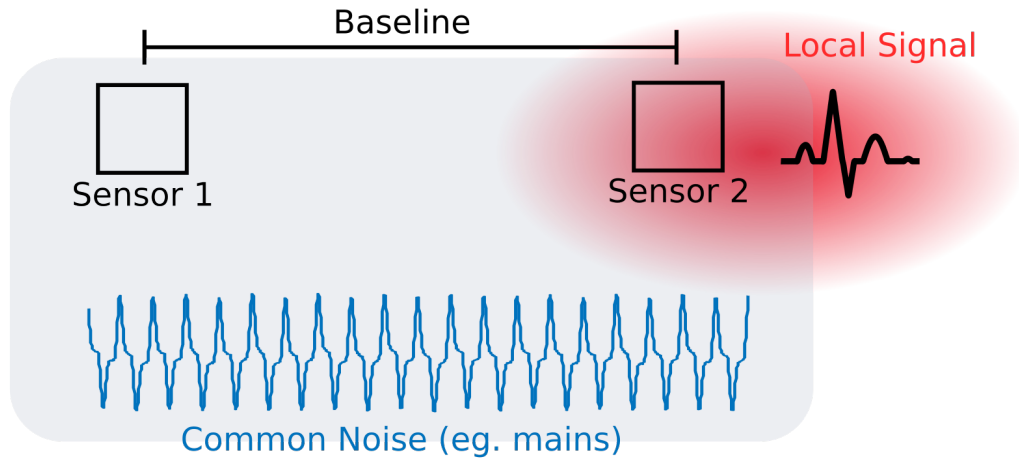


Figure 6.1: General schematic of a gradiometer where two sensors volumes are separated by a distance defined as the baseline. Both sensors experience common noise, eg. mains noise (blue), and Sensor 2 detects a magnetic signal local to its sensing volume (red). By subtracting the two measurements the common noise is rejected and only the local signal remains.

common mode noise suppression, which allows for a flexible baseline [83]. SQUID and fluxgate gradiometers have been widely demonstrated [84, 85], and optically-pumped magnetic gradiometers have been successfully constructed in many different configurations. These include two beams in a single cell [86–88], two separate magnetic sensors [83], and two separate cells in a single portable sensor [31, 32]. Shielded gradiometers have already found applications in proton NMR experiments [31, 82], and unshielded gradiometers in MCG [89] and geophysics [18]. Some of the most sensitive measurements in an unshielded environment to date have been performed using a gradiometer. Limes et al. have recently demonstrated the first unshielded magnetoencephalography measurement using a gradiometer based on free induction decay [31]. In that work they reported a common-mode rejection ratio of at least 2000, which yields a sensitivity of $16 \text{ fT/cm}/\sqrt{\text{Hz}}$.

An intrinsic magnetic gradiometer describes a system that uses the same laser beam to probe the Larmor precession of the atoms in two sensor volumes in succession. The rotation of the first and second sets of atoms will be imprinted on the beam by the precession of each atomic ensemble. In this work, RF modulation is used to drive the coherent precession of each ensemble, and the atoms are driven at the same frequency with exactly opposite

phase. If the atoms are experiencing the same field magnitude, the resonant response from one sensor volume should cancel on subtraction from that of the other, assuming identical responses from each volume. If the Larmor frequency is different in each location, the signals subtract but do not completely cancel. The resulting signal can be used to measure the field gradient along the axis of the gradiometer baseline. This gradiometric measurement has the potential to yield very sensitive magnetic measurements [88, 89].

The total cancellation of the resonant response is possible only if the atomic vapour cells have identical magnetic lineshapes. Balancing the cells is tricky, especially when separate cells are used. Methods to address this have been demonstrated by Zhang et al. [89] by balancing the pump and probe intensity, and Kamada et al. [88] by using a single cell with two sensing volumes. An advantage of using a single cell is that the operating parameters should be identical, and hence the same linewidth and signal amplitude can be expected from each sensor volume. However, the baseline is fixed in the case of a single cell, and cell manufacturing techniques limit the cell size and therefore the maximum baseline. Using separate pump and probe beams allows for further control of the response from each cell, but necessitates more beam paths and optical access to each cell. This chapter will follow from previous intentions of compact form and scalability, and will describe work towards an intrinsic gradiometer with a single beam and two cells.

6.2 Microfabricated Cell Gradiometer

With the microfabricated cells described in Section 4.1 it is possible to build a gradiometer with a flexible baseline which can be as short as a few millimetres. Two cells with similar buffer gas pressures were selected and mounted within the static coil pairs described in Chapter 4. The cells are spaced symmetrically from the centre of the coil pairs along the axis of the light. The mounting system allows the cells to be accurately located with respect to each other and the beam. A schematic of the mounting system can be seen in Figure 6.2.

The PCB cell mounts can be mounted in a single lens tube so that both cells face into the lens tube, almost completely enclosed. This allows for good thermal stability by shielding the cells from convection currents. The cells are heated individually using the AC heating method described in Section

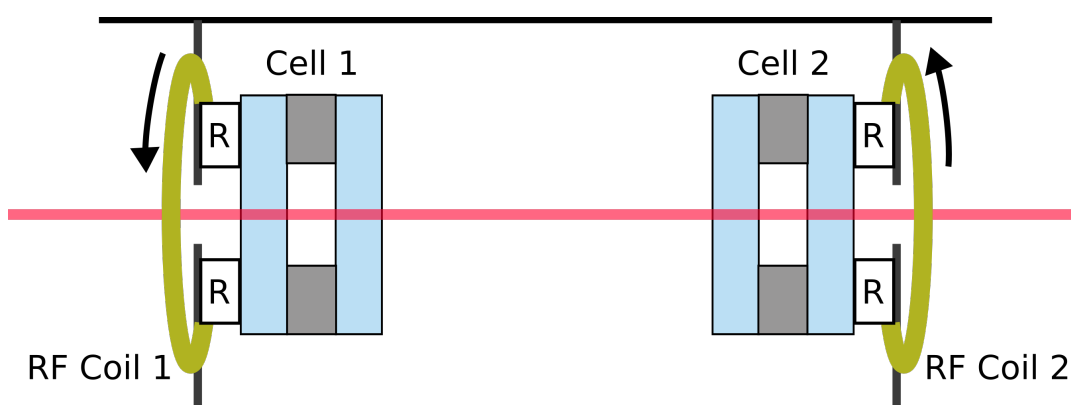


Figure 6.2: Cut-through of the lens tube holding the cells. The cells are mounted on heating resistors (R) on a printed circuit board with integrated RF coil. The cells are 30 mm apart. The heating and RF control for each cell is separate. The current direction in each coil is shown here with arrows: in this configuration the current is out of phase.

4.1. Individual amplifiers are used to apply signals of different amplitudes and frequencies in order to achieve different temperatures in each cell.

In a single-beam configuration, some laser light will inevitably be lost through the first cell to absorption, and the light intensity will be attenuated in the second cell. By adjusting the cell temperatures individually, the drop in laser intensity due to absorption by the first cell can be accounted for, as well as any magnetic resonance linewidth variability between cells due to differing pressure. The atomic density in the first cell can be reduced and the second increased, in order to achieve well-balanced signals. The integrated RF coils around each cell are controlled individually, and RF amplitude is another parameter that can be adjusted to match the resonance linewidth and amplitude of the magnetic resonance from each cell. A small amount of cross-talk is inevitable here, but this is assumed to be negligible in the present work.

Due to a background field gradient along the baseline, an applied gradient of approximately $\delta B/\delta y = 17 \text{ nT/mm}$ has been required to balance the cells. The gradient is applied along the baseline axis such that the cell responses overlap at the Larmor frequency of the applied field at $20 \mu\text{T}$. The laser passes through each cell sequentially and is then detected by the balanced polarimeter, as described in earlier chapters. The magnetic resonance plots that follow show the demodulated signal from the laser after it has passed

through both cells.

The response from each cell is a Lorentzian with in-phase and quadrature components, X and Y , as described in Section 2.5 and seen experimentally for a single microfabricated cell in Section 4.1. The signal that is seen by the polarimeter arises due interaction of the beam with cell 1, and then cell 2, and in the limit of weak optical rotation, is the sum of the X and Y responses from each one. This can be modelled by the addition of the components of the Lorentzian lineshape. Magnetic resonance scans were taken from each cell individually, and the parameters Γ , the FWHM, and A , signal amplitude were found from the fit to the resonance response. The fit parameters from each cell have been used to model the lineshapes presented here.

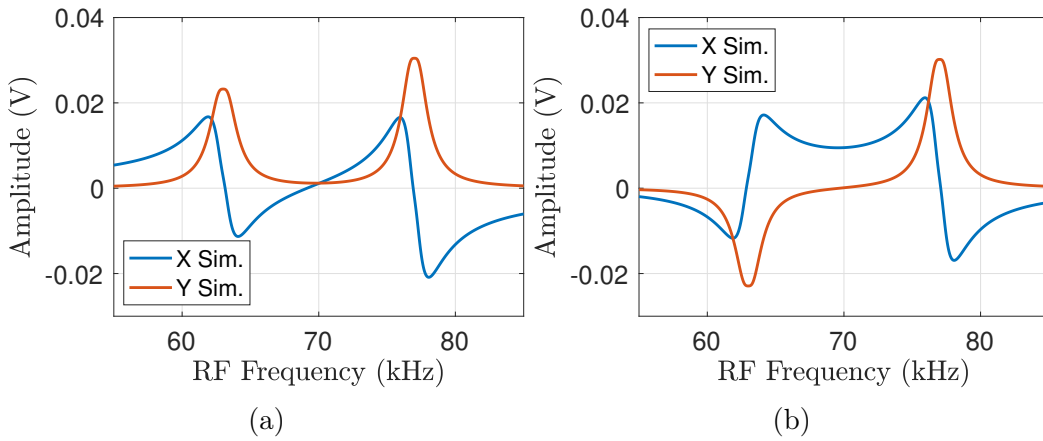


Figure 6.3: Simulated response for the intrinsic gradiometer in the presence of a large field gradient. The RF field is swept through the Larmor frequency of each cell. (a): RF signals applied to each cell are in-phase. (b): RF signals applied to each cell are out of phase.

Figure 6.3 shows simulated responses for the intrinsic gradiometer described here. These plots show the response of both cells to a sweep of the RF field frequency through the resonant frequency of each cell, it should be noted that the individual responses are not perfectly matched, but still close to ideal behaviour is seen. In this case, a large gradient is simulated in the vicinity of both cells along the light-axis, such that the resonant responses are 14 kHz apart, corresponding to a difference in the magnetic fields of $\delta B = 4 \mu\text{T}$. The signal in Figure 6.3a is for the case when the RF modulation is in-phase - experimentally, the signal to the RF coil around each cell is synchronous. In the case of Figure 6.3b, the signal from cell 1 is perfectly out of phase with cell 2. The phase is relevant here due to demodulation of the signal,

which sets the sign of the individual signals from each cell. For the purpose of this work, the case in which the RF fields applied are 180° out of phase will simply be referred to as the out-of-phase mode.

Both figures 6.3a and 6.3b yield a measurement of the field gradient — by measuring the Larmor frequency of each resonant response and knowing the baseline, $\frac{\delta B}{\delta y}$ can be found. The gradient has been found experimentally and the gradient calibration factor adjusted accordingly. For the out-of-phase mode shown in Figure 6.3b, the signals intrinsically subtract such that were they perfectly balanced, the signal would go to zero. Any small difference in the field measured between the cells produces a signal in the X -channel that is proportional to that difference.

For the case where gradient along the light-axis is small, the resonant line-shapes overlap. When the RF signals are in-phase, the amplitude of the response is larger than that of a single cell, as the signals add. The in-phase mode may be practically used to balance the cells by maximising the signal amplitude. The experimental signal from the in-phase mode can be seen in the data in Figure 6.4a, where the on-axis gradient has been minimised. The model of this mode presented in Figure 6.4b agrees well with the experimental results.

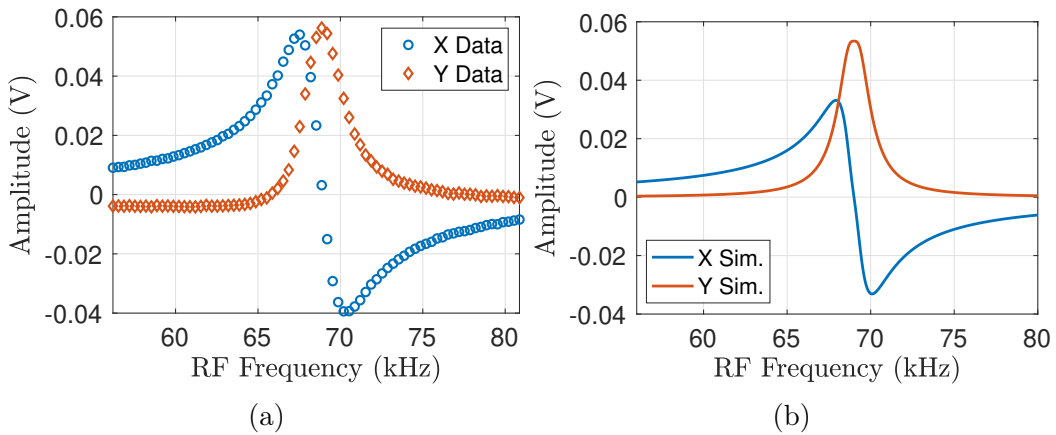


Figure 6.4: (a): Data and (b): Model of the signal from the intrinsic gradiometer being run in the in-phase mode, for the case where the magnetic resonance parameters for each cell are well-balanced and the gradient along the axis of the baseline has been minimised.

When the RF coils are driven out of phase with each other, the response from each cell subtracts, and a reduction in the signal amplitude is seen, as in Figure 6.5a. The model replicates this drop in signal amplitude, seen in

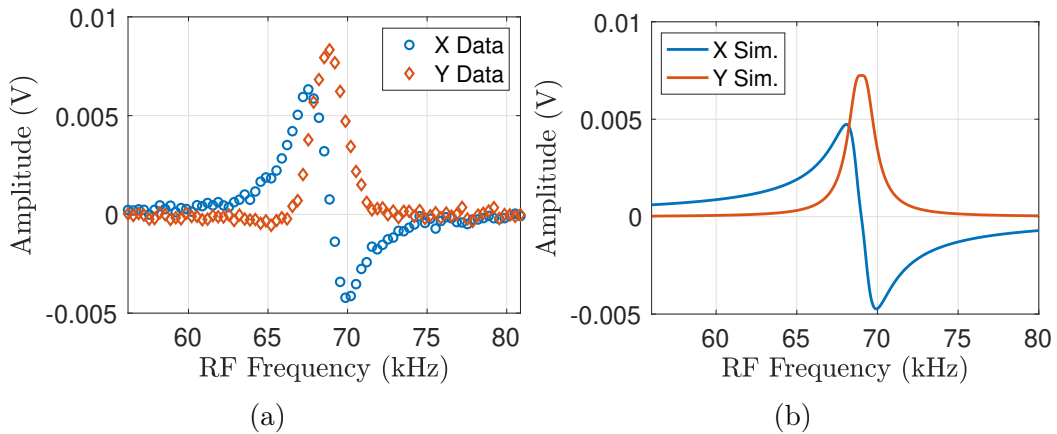


Figure 6.5: (a): Data and (b): Model of the signal from the intrinsic gradiometer being run in the out-of-phase mode, for the case where the magnetic resonance parameters for each cell are well-balanced and the gradient along the axis of the baseline has been minimised.

Figure 6.5b. For these data the on-axis gradient was minimised. Here it can be seen that the X and Y signals do not go to zero, that is, they do not perfectly cancel. However, there has been an approximately 85% reduction in the signal amplitude from the in-phase results in Figure 6.4a.

As the on-axis gradient increases, the subtraction of the signals yields the response seen in Figure 6.6. The applied field in this instance is $20 \mu\text{T}$, with a Larmor frequency of 70 kHz. The resonant response of each cell can be seen to shift symmetrically along the frequency axis in response to an applied gradient.

To check the behaviour of the gradiometer, a single RF frequency was applied in a free-running mode. The required frequency is the average value of both sensors, which is found by first running a frequency sweep, yielding a signal such as Figure 6.4a. By monitoring the DC level of the X response at the Larmor frequency as the applied gradient is stepped from positive to negative around the balance point, the gradient can be monitored as it modifies the lineshape. This yields a response function for X and Y amplitude on resonance with respect to gradient, seen in Figure 6.7a. The response of Y is mostly flat, with the dip on resonance due to the cells being slightly imbalanced. The X -response exhibits a dispersive shape which, as seen in earlier chapters, is close to ideal for making sensitive measurements.

From the data shown in Figure 6.7a, the central linear portion of the X DC level between $\approx \pm 15 \text{ nT/mm}$ can be used for gradiometry. By balancing

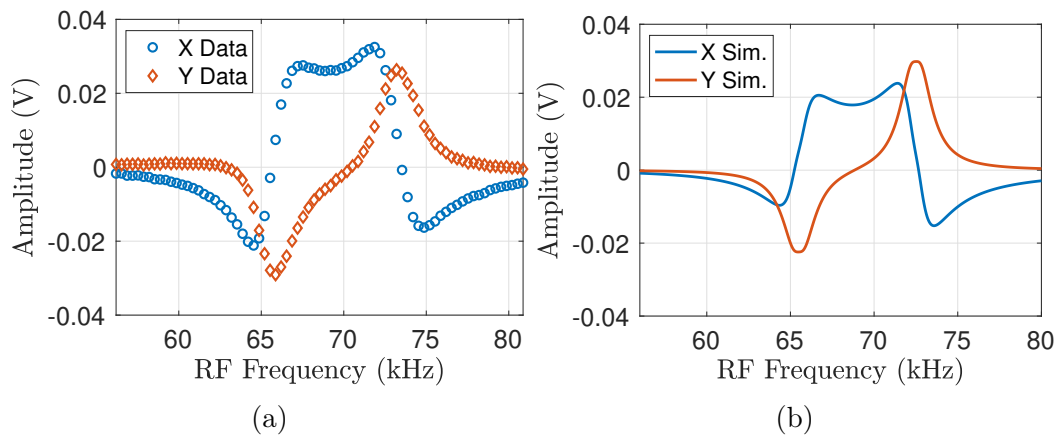


Figure 6.6: (a): Data and (b): Model of the signal from the intrinsic gradiometer being run in the out-of-phase mode, for the case where the magnetic resonance parameters for each cell are well-balanced. A gradient of approximately 70 nT/mm has been applied.

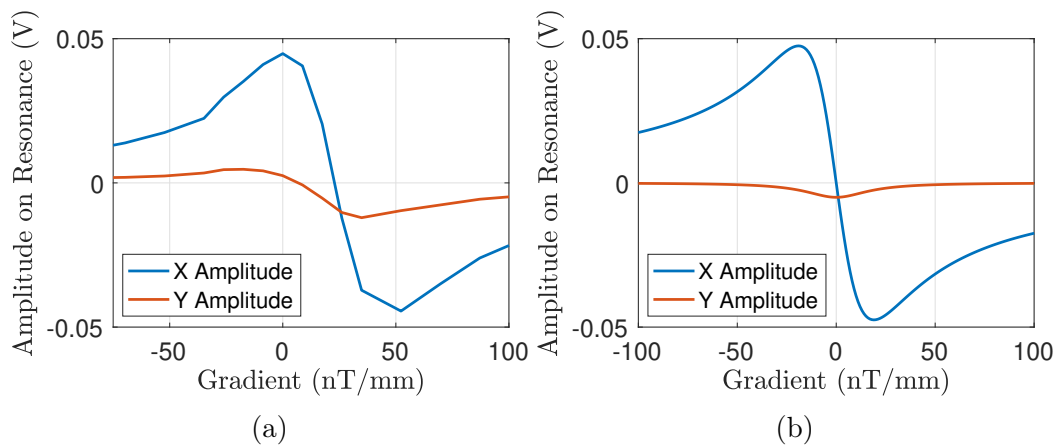


Figure 6.7: (a): Measured response of X and Y features of two cells to a gradient applied along the y -axis. The dispersive feature is offset from zero on the gradient axis due to the balance point of the cells, which has been found to be ≈ 17 nT/mm. (b): Simulated X and Y amplitude response on-resonance (70 kHz) to applied gradients.

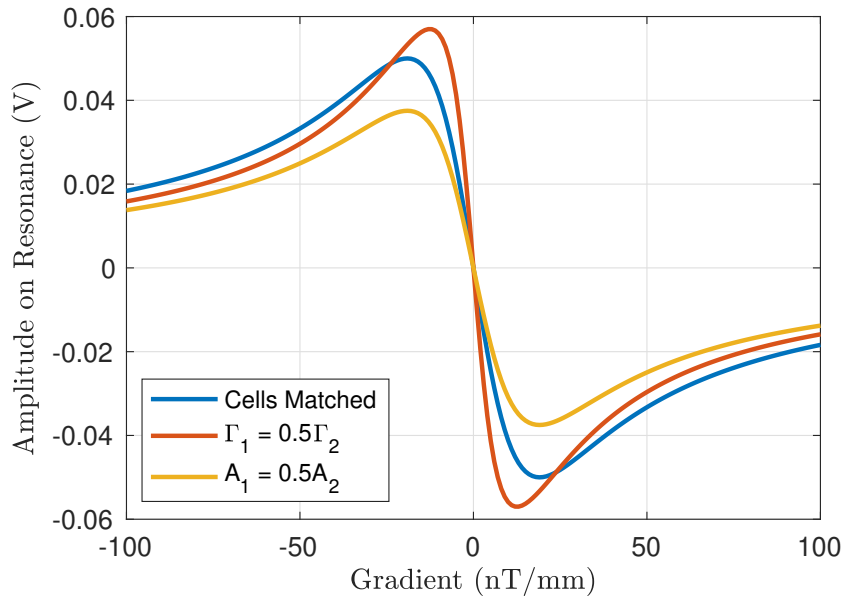


Figure 6.8: Simulated response of the gradiometer for different values of relaxation rate, Γ and signal amplitude, A . Cells are matched when the relaxation rate and signal amplitude of each cell are identical.

the cells to operate in this region, the response of X on resonance can be monitored in order to take a gradiometric measurement. The limit of linear region is roughly when the individual signals are split by Γ . This sets a scale for the sensitivity; $\delta B/\delta y \approx \Gamma/\delta y$. The range of the gradient measurement will depend on the separation between the cells - a longer baseline gives better sensitivity but narrows the linear range. This system intrinsically subtracts the signals, and in this way common mode noise should also be subtracted. Modelling different values of the resonance linewidth and signal amplitude yields different response curves, seen here in Figure 6.8. “Unbalancing” the cells by changing the amplitude and linewidth of one of the cell responses results in a steeper gradient response. This could yield a more sensitive measurement of the gradient, but the noise contributions from each sensing volume may not be favourable [89]. By changing the cell parameters it may be possible in this way to improve sensitivity in a sensor with a fixed baseline. The measured gradient response shown in Figure 6.7a provides a promising starting point for gradiometric measurements. Further investigation is required to understand how the contributions from linewidth and amplitude contribute to the magnetic noise floor. The next steps include taking an unlocked measurement over a long period of time in order to examine and

compare the spectral response of the in-phase and out-of-phase operation modes. Known calibration signals could be applied to the sensors as described in Section 7 by placing an auxiliary coil around one or both cells.

6.3 Glass Vapour Cell Gradiometer

The glass vapour cells described in Section 3.1 can be operated in an unshielded environment, though the resonance linewidth is significantly broadened due to background gradients. In principle, since these cells have an intrinsic resonance linewidth that is significantly narrower than the micro-fabricated cells, they might be exploited for improved sensitivity under the right conditions.

6.3.1 Vapour Cell Mount Design

In order to operate a gradiometer using the large blown-glass vapour cells, the location of the cells with respect to the laser and each other should be well-defined. Refraction of the laser beam can occur as the beam passes through the curved walls of the cells. In order to minimise beam steering of the light, the beam should pass through the centre of each cell, and once the beam has been aligned through the cells onto the detector, the cells should not move, as small changes in their position can lead to beam misalignment. Each cell should be located as close as possible to the centre of its RF coil in order that the RF field is uniform within the cell. The RF coils must be large enough to create a homogeneous field in the volume of the cells, but must be far enough apart to minimise cross-talk between them. The baseline of the gradiometer mount was chosen to fit inside the static field coils described in Chapter 4 such that the static field that the cells experienced would be reasonably homogeneous. A baseline of 90 mm between the cell centres was set.

A mount was designed to locate and hold the vapour cells with formers for the RF coils that are precise with respect to the location of the cell. The mount was 3D printed using a Formlabs Form 2 printer with a resolution of approximately 25 microns. The cells are held in place by protruding rings from the mount body, as seen in Figure 6.9d. The mount top and bottom sections are held in place using nylon threaded bars and nylon nuts. The

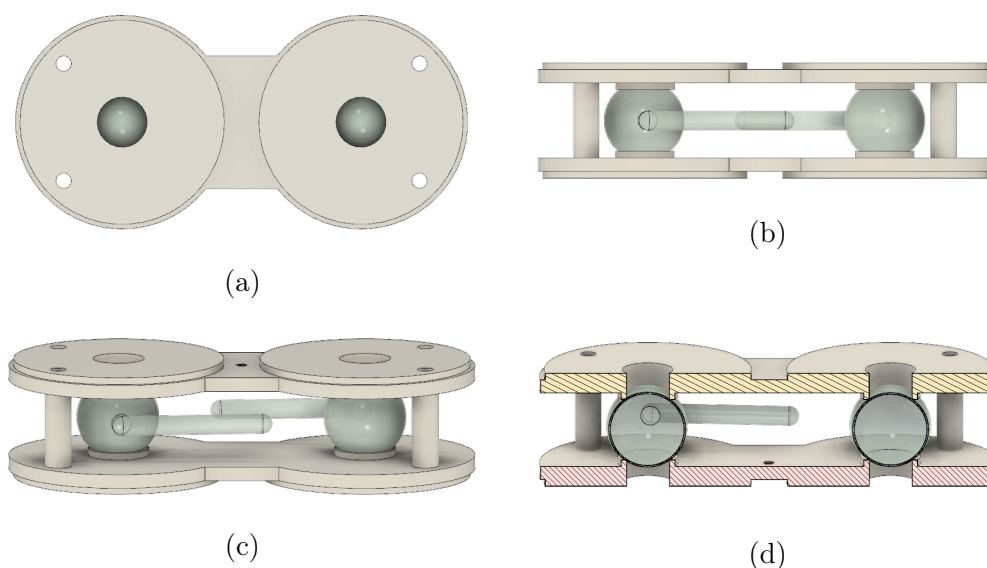


Figure 6.9: Design drawings for the gradiometer mount displaying different angles in (a), (b), (c) and cut-through, (d). The cells are similar to those shown in Figure 3.4.

RF coils are each wound using a single loop, which is terminated in twisted pairs; these coils are controlled in software.

6.3.2 Sensor Characterisation

Each RF coil can be controlled individually, in the same way as the microfabricated gradiometer described in the previous section, with software control of the RF amplitude and frequency separate for each cell. The magnetic resonances for each cell are recorded individually, shown in Figures 6.10a and 6.10b. Based on the slight distortion of the lineshape at the Larmor frequency of the other cell, it can be seen that there is some crosstalk of the RF field between the cells. The amplitude of this crosstalk is small with respect to the signal and is not likely to distort the final signal. Figure 6.11 shows the signal for the case when both RF coils are switched on.

The operation of the glass-cell intrinsic gradiometer has not been fully optimised. Although the signals from individual cells have acceptable SNR and reasonably undistorted lineshape, when a gradient is applied using the static field coils, the overlapping resonance lineshapes become very distorted and a clean gradiometric signal requires more work.

The glass cells are 90 mm apart (centre to centre) in a set of coil pairs with

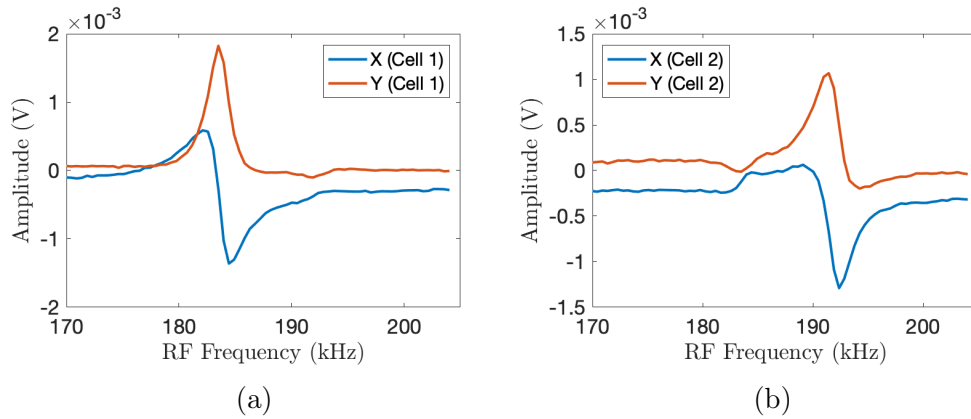


Figure 6.10: Magnetic resonance scans for the cases where (a): There was signal to RF coil 1, and no signal to RF coil 2, and (b): There was signal to RF coil 2, and no signal to RF coil 1.

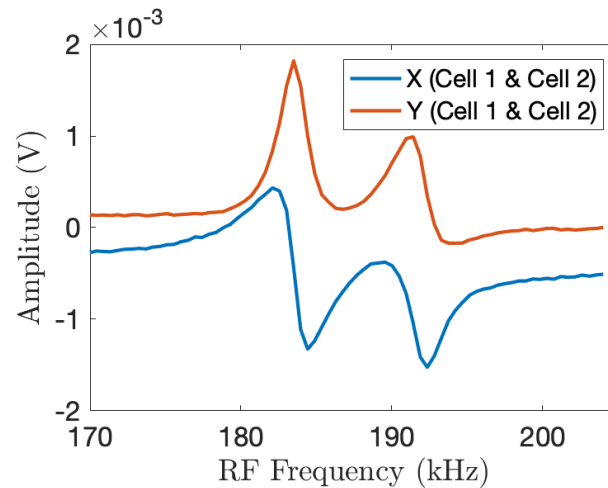


Figure 6.11: Overlapping magnetic resonances from cell 1 and cell 2, while both RF coils are in operation.

a radius and separation of approximately 170 mm. This means that the cells in this configuration are far from the centre of the coil pairs. This has made it tricky to adjust the gradient in a homogeneous way. The atoms in the large glass cells are very sensitive to field gradients along all axes, and by placing these in the static field coils offset from centre, it is difficult to apply a homogeneous field without unacceptable gradients distorting the resonant response. This issue could be solved by using a larger set of static field coils capable of creating a uniform field over a larger volume.

Given that the glass cells exhibit a magnetic linewidth almost as wide as that of the microfabricated cells, it seems likely that the work in [Section 6.2](#) will represent a more fruitful approach, with little lineshape distortion due to field gradients. The microfabricated gradiometer may be balanced using heat and RF field amplitude, giving greater flexibility while being more readily scalable to portable devices.

Chapter 7

Conclusion and Outlook

In this thesis double-resonance magnetometry has been explored as a route to portable magnetic field sensing. The experimental considerations have been outlined for this double-resonance sensor and the specific design choices made have been justified with regard to scalability.

The shielded experiment described has served as a controlled, quiet environment used for testing effects inherent to double resonance magnetometry. This setup has been used to develop the iterative optimisation technique for magnetic field control described here. The optimisation technique has yielded a field magnitude tolerance of 0.24 nT on an applied field of 200 nT and has allowed subsequent experiments to make use of a well-defined and isotropic field. A typical sensitivity achieved in the shielded setup is $170 \text{ pT}/\sqrt{\text{Hz}}$.

An unshielded experiment with the same design characteristics as the shielded setup has been described. This experiment has primarily been used to test new experimental techniques for use in unshielded sensors, as well as for characterising microfabricated cells. Results from a selection of cells have been presented, and the best sensitivity achieved using a microfabricated cell in the unshielded setup is $2 \text{ pT}/\sqrt{\text{Hz}}$.

Several interesting effects have been observed in the microfabricated cells tested here. The light-narrowing effect may be advantageous in improving sensitivity, but it remains to be seen whether it is a useful effect for future sensors. In particular, if this effect may only be observed at high light powers, its utility in portable sensors may be limited. Despite linearly polarised light being used in cell characterisation, the angular sensitivity observed from the microfabricated cells has the characteristics of an orientation moment, and work is ongoing to determine the exact process by which this signal arises.

Noise has been a significant consideration throughout this work, and efforts to characterise the sources have been detailed, along with experimental considerations for reducing noise inherent to the sensor. An approach has been taken whereby some noise in the unshielded regime is considered inevitable, and techniques have been developed to address the primary magnetic noise sources.

The remainder of the thesis has investigated methods for operating a sensor in the presence of significant noise sources. As such, a software technique has been demonstrated for suppression of periodic noise. The feed-forward scheme has been successful in suppressing noise arising from the 50 Hz mains AC line, achieving 22 dB of suppression between 45 and 55 Hz, as well as suppression of the primary harmonics.

The feed-forward technique has the potential to be scaled to improve the duty cycle. A shorter unlocked measurement should still yield good noise suppression for 50 Hz and its main harmonics, and may couple less low-frequency noise to subsequent measurements. The initial snapshot could also be used adaptively, adjusting to changes in the field as the sensor runs continuously.

As part of the work on the feed-forward technique, oscillating fields of fixed amplitude were applied to the sensor to determine the bandwidth, which was found to be 520 Hz. Other arbitrary signals have been applied and successfully recovered. The feed-forward scheme is easily implementable in an unshielded system where large amplitude periodic noise dominates. In its current form it lends itself to applications that do not require 100% duty cycle, and those where the signal to be measured is periodic or can be deterministically turned on and off. The feed-forward technique uses a snapshot that may include spurious non-periodic noise. By fitting spectrally to the response, noise could be removed from the signal to be fed forward.

Preliminary results from an intrinsic magnetic gradiometry experiment have been presented using two different cell types. The intrinsic addition of the signals obtained experimentally matched the modelled responses accurately. The intrinsic gradiometer is promising for the purposes of scalability due to the single beam path. Given that the microfabricated cells yielded promising results, it seems this system would be easily scaled to a more compact setup. A key area of future study in the gradiometer is the observation of common mode noise suppression. A comparison of the intrinsic “out-of-phase” mode

with respect to the response of a single sensor will determine the efficacy of this technique. It may be the case that the sensitivity to the gradient can be altered according to the cell parameters, and further work is required to determine the impact this may have on noise. Once the gradiometer is configured to allow free-running measurements it will be worthwhile to apply known signals and monitor its response.

Some of the work in this thesis has already contributed to the production of portable, compact sensors, which will be described in future publications. In particular, cell characterisation in the work described here has informed cell selection for other sensors built in this group. It is hoped that the feed-forward and gradiometric schemes may be implemented in portable sensors. In the meantime, both shielded and unshielded experimental setups continue to serve as invaluable testbeds for miniaturised components and future portable sensors.

Appendix: A Feed-Forward Noise Suppression Scheme for Periodic Noise Suppression in Atomic Magnetometry

A Feed-Forward Measurement Scheme for Periodic Noise Suppression in Atomic Magnetometry

Carolyn O'Dwyer,^{1, a)} Stuart J. Ingleby,¹ Iain C. Chalmers,¹ Paul F. Griffin,¹ and Erling Riis¹
Department of Physics, SUPA, University of Strathclyde, Glasgow, G4 0NG, UK

(Dated: 13 March 2020)

We present an unshielded, double-resonance magnetometer in which we have implemented a feed-forward measurement scheme in order to suppress periodic magnetic noise arising from, and correlated with, the mains electricity alternating current (AC) line. The technique described here uses a single sensor to track ambient periodic noise and feed forward to suppress it in a subsequent measurement. This feed forward technique has shown significant noise suppression of electrical mains-noise features of up to 22 dB under the fundamental peak at 50 Hz, 3 dB at the first harmonic (100 Hz), and 21 dB at the second harmonic (150 Hz). This technique is software based, requires no additional hardware, and is easy to implement in an existing magnetometer.

I. INTRODUCTION

Unshielded magnetic sensors that operate at geomagnetic field magnitudes will provide previously unavailable precision to applications in archaeology¹, surveying², cardiology³ and many other fields^{4,5}. To satisfy the needs of such differing applications magnetometers must provide, variously, high dynamic range, wide bandwidth, and high sensitivity. As an example, applications in magnetocardiography ideally require the capability of operating in Earth's field of $\sim 50 \mu\text{T}$, bandwidths of DC–100 Hz, and sensitivities approaching $1 \text{ pT}/\sqrt{\text{Hz}}$ ⁶.

Superconducting quantum interference devices (SQUIDs) and fluxgates have long been established as sensitive and reliable magnetic sensors, but they have a number of limitations. SQUIDs require cryogenic cooling which limits their use as portable, compact sensors⁷. Fluxgates, despite their portability, lack the required sensitivity for applications with short integration times or those requiring good low frequency resolution, such as detection of rotating machinery^{5,8}. Optically pumped atomic magnetometers have operating temperatures in the range 20–200°C and demonstrate sensitivities comparable with SQUIDs and far exceeding fluxgates. Of this class of device, spin exchange relaxation-free (SERF) atomic magnetometers lead the way in absolute sensitivity⁹, but their measurement range is limited to near-zero fields¹⁰. Double resonance atomic sensors have excellent dynamic range, achieving sensitivities compatible with a range of applications with the potential to operate in the Earth's field¹¹.

In this work, we report a double-resonance atomic magnetometer that achieves $\leq 100 \text{ pT}/\sqrt{\text{Hz}}$ sensitivity in a noisy, unshielded environment using a robust and easily-implemented feed-forward method with a -3 dB cut-off frequency of 520 Hz. The magnetometer described here uses an elliptically polarized beam to create a net magnetisation in the atomic cesium vapor due to orientation of their spins through optical pumping¹². The magnetisation precesses about the ambient field, B , at ω_L , the Larmor frequency such that: $\omega_L = \gamma B$, with proportionality constant γ being the gyromagnetic ratio. The atoms are simultaneously optically pumped with near-resonant light and interrogated magnetically with a

near-resonant oscillating magnetic field in a process known as double-resonance magnetometry¹³. In this case we drive the precession with a small sinusoidal RF field, B_{RF} . This technique has the advantage of simple geometry, with a single laser beam acting as pump and probe. Our experimental setup has been designed as a test bed for portable sensors, and we aim to minimize the complexity and number of optical elements. Alternative schemes such as amplitude or polarization modulation have additional power and space constraints due to component requirements such as acousto-optic and electro-optic modulators^{14,15}.

Periodic environmental magnetic noise is a challenge for unshielded magnetometers^{16,17}. A common source of noise in unshielded indoor environments is inductively-driven magnetic fields generated at harmonics of the AC line electrical supply frequency. In our laboratory, this line noise has a typical amplitude in the 100 nT range, observed at 50 Hz (United Kingdom electrical mains frequency) and higher harmonics.

Typically, environmental noise is dealt with by using passive shielding or active compensation. Passive shielding, which places the sensor inside a highly-permeable enclosure is necessarily bulky, heavy and shields the sensor from signals of interest. Active compensation, through the generation of local magnetic fields opposing components of the environmental field, can be achieved either dynamically or statically using coils and low-noise current drivers. Schemes have been implemented which modify the ambient field around the experiment in order to reduce magnetic noise¹⁸. Often an additional sensor such as a fluxgate is used to generate an error signal¹⁹. Within active compensation there are two broad categories; feedback and feed-forward. Feedback directly reacts to changes in the field based on the last instantaneous measurement²⁰. Feed-forward takes a slice of data over time and feeds forward a prediction to the next slice. This can be implemented by feeding forward to compensation coils to cancel the ambient noise in the field external to the sensor^{21,22}. In this work an ambient field snapshot is fed forward to the sensor itself, modifying the RF field frequency to track the ambient field more accurately as it varies in time, thus ensuring that the magnetometer operates close to its maximum sensitivity throughout the noise cycle. This can be advantageous if feedback is not implementable due to equipment latency and data transmission rate constraints.

We describe a feed-forward scheme that takes a free-running measurement in the presence of noise and a feed for-

^{a)}Electronic mail: carolyn.odwyer@strath.ac.uk

ward measurement sequentially, by tracking the Larmor frequency in the same sensor. Oscillating signals of interest should not be present during the unlocked measurement. As such, the signal must be capable of being isolated, switched, or moved with respect to the sensor between the unlocked and feed-forward stage. The measurements are triggered from the AC line signal such that the feed-forward measurement phase matches the magnetic noise and the RF field frequency follows the Larmor frequency more accurately – reducing the power under the 50 Hz peak in the frequency domain by 22 dB and the overall noise floor by 20 dB (in the bandwidth 1 Hz to 1 kHz). Although feed-forward schemes have previously been implemented to control the ambient magnetic field, we do not know of any to date that operate in the same sensor, or by feeding forward to the RF field frequency, thereby tracking the real ambient field more closely.

II. EXPERIMENTAL SETUP

The experimental setup schematic of the unshielded double resonance magnetometer can be seen in Figure 1. An external cavity diode laser tuned to the cesium D1 transition is elliptically polarized and incident on a micro-fabricated vapor cell containing cesium and 700 Torr nitrogen buffer gas. The smallest inner dimension of the cell is 2 mm. The cell is mounted on a small purpose-built printed circuit board (PCB) and heated to approximately 80 degrees using an AC heater driven at 17 MHz. This temperature ensures sufficient vapor pressure and thus atomic density of cesium in the cell. The PCB has an integrated RF coil that is used to apply RF fields to the cell. This is controlled in software via a digital to analog converter (DAC).

The cell is at the centre of a three-axis Helmholtz coil set which act to compensate the Earth's field and apply arbitrary fields in any orientation²³. The laser light interacts with the atoms and is subsequently analysed by a half-wave plate. A Wollaston prism (WP) separates the light into its orthogonal components and directs them onto a two-channel differential photodiode. The polarization rotation due to circular dichro-

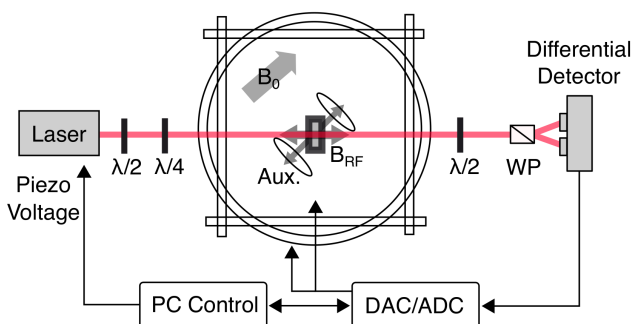


FIG. 1. Schematic of the experimental setup. The laser is elliptically polarized and incident on a microfabricated atomic cell. The ambient field, B_0 is controlled by three-axis Helmholtz coils and B_{RF} is applied on a small coil mounted close to the cell. The magnetic signal is read using a balanced photodetector and both analysis and system control is done in software. (DAC: Digital to Analog Converter; ADC: Analog to Digital Converter; WP: Wollaston Prism; Aux.: Auxiliary coil)

ism is read by the computer via an analog to digital converter (ADC), and demodulated at the applied B_{RF} field frequency.

III. RESULTS

The feed forward measurement scheme comprises three distinct steps; a resonance sweep, an unlocked noise measurement, and a feed forward measurement.

The resonance sweep is generated by scanning a 300 nT sinusoidal field, amplitude B_{RF} and frequency ω_{RF} through a range of frequencies in the region of the Larmor frequency and the resultant signal is demodulated at the applied frequencies. This produces a Lorentzian resonant response, as seen in Figure 2, with the zero-crossing corresponding to ω_L . By fitting to the in-phase (Y), quadrature (X) and phase components of the demodulated signal the parameters Γ , the relaxation rate; ω_L , the Larmor frequency; and A , the on-resonance amplitude can be calculated. The fit functions are as follows:

$$X = \frac{xA}{1 + S^2 + x^2}, \quad (1)$$

$$Y = \frac{(1+x)A}{1 + S^2 + x^2} \quad (2)$$

where $x = \frac{\omega_L - \omega_{RF}}{\Gamma}$, $S = \frac{\Omega}{\Gamma}$, and Ω is the magnetic Rabi frequency. Parameters relevant to the feed-forward scheme are tabulated in Table I. A pre-trigger time is included before the B_{RF} is applied, during which only the static field is applied. The noise on this measurement is calculated by taking the RMS deviation of the polarimeter signal while no B_{RF} is applied for the same sample time as the resonance scan in question.

The measured Larmor frequency, ω_L , is then used in a free-running, or 'unlocked' measurement. The start of this measurement is triggered from the AC line. A constant RF field at ω_L is applied for a period of time and the response of the magnetometer measured. The polarimeter signal is demodulated at ω_L and the in-phase signal component (X) is converted to

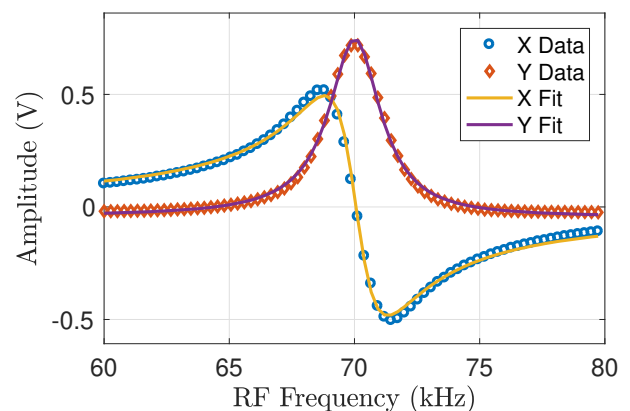


FIG. 2. In-phase and quadrature components of the magnetic resonance signal for an applied RF magnetic field that is swept through the Larmor frequency.

| | |
|---|------------|
| Larmor frequency, ω_L (kHz) | 70.049(11) |
| SNR | 4370(62) |
| Relaxation Rate, Γ (kHz) | 1.016(14) |
| Sensitivity, \sqrt{PSD} (pT/ $\sqrt{\text{Hz}}$) | 2.913(69) |

TABLE I. Values of experimentally-relevant parameters derived from fits to the resonant response in Figure 2.

a magnetic field deviation using the fitted on-resonance gradient. This is a snapshot of the ambient periodic magnetic noise.

The in-phase response of the magnetometer is applied to the next measurement as a modulation of the applied RF field frequency. This measurement is also AC-line triggered in order to ensure that its phase matches the previous measurement. The sensor has been found to more accurately track the ambient field when operating in this mode. The reduction of the noise amplitude maintains the magnetic signal in the desired linear operating regime. This can be seen clearly in the demodulated data in Figure 3. The RF frequency more closely tracks the Larmor frequency on the feed-forward measurement, resulting in the peak to peak amplitude being reduced by ~ 200 nT.

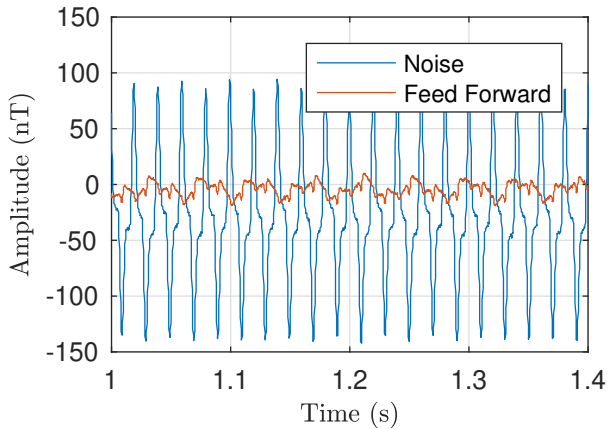


FIG. 3. Segment of demodulated magnetic field data from a 6 second period in the unlocked (blue) and feed-forward (red) modes.

The noise reduction can be seen more clearly in the frequency spectrum, as seen in Figure 4. The power under the 50 Hz peak is reduced by 22 dB in the range between 45 and 55 Hz as well as the peak amplitude being reduced by a factor of over 500. The peak at 100 Hz is reduced by 3 dB between 95 and 105 Hz, and the 150 Hz peak is suppressed by 21 dB between 145 and 155 Hz.

The peak at 22 Hz corresponds to building air conditioning units which are not in phase with the AC line. These units are directly adjacent to the lab and therefore the magnetic signal is large with respect to other noise sources. The feed-forward routine does not suppress the noise from this source, and instead the noise at 22 Hz is increased. This will be the case with any signal not phase-locked to the mains signal present during the initial unlocked measurement. This observation highlights a limitation of our technique.

In order to test the noise cancellation technique in the presence of an arbitrary magnetic field signal, a small auxiliary Helmholtz coil pair is placed around the cell. The

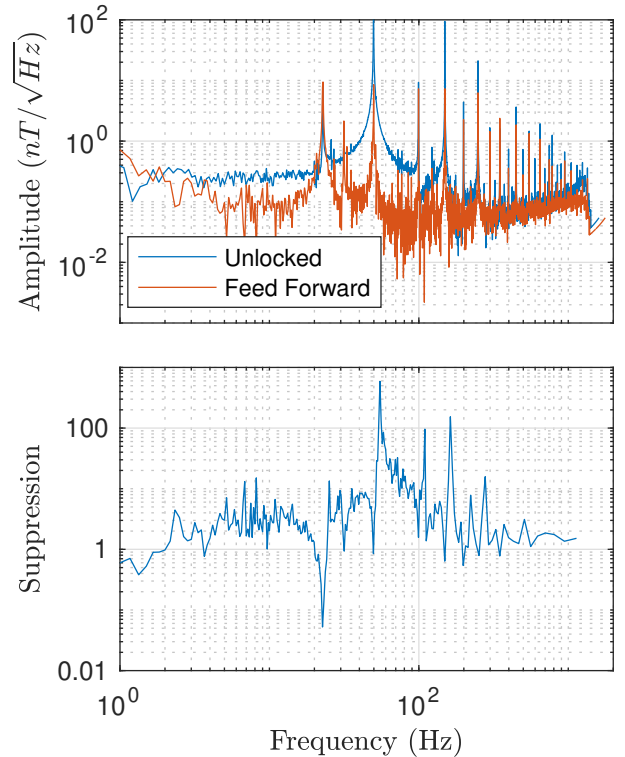


FIG. 4. Top; magnetic noise spectra for the unlocked (blue) and free-running (red) modes. The power under the 50 Hz line and its harmonics can be seen to be reduced in the feed-forward mode. These data have been rescaled by the response of the sensor. Bottom; ratio of unlocked spectral response to that of feed-forward, showing ability of the feed forward technique to suppress in-phase periodic noise across a range of frequencies. In particular the peak at 50 Hz is suppressed by a factor of 500. Data have been rebinned into 500 logarithmically spaced bins for clarity.

coils are aligned to the axis of maximum sensitivity of the magnetometer²⁴. A function generator can apply oscillating currents to the coil at arbitrary frequencies during the feed forward measurement stage and this can be demodulated in software to recover the amplitude of the field.

Applying a known, constant amplitude oscillating field at different frequencies yields the frequency response of the sensor in Figure 5 from which the bandwidth of the sensor can be inferred to be 520 Hz (-3 dB cut-off). The region up to 100 Hz is flat, and we are able to resolve frequencies close to the 50 Hz line. This demonstrates part of this scheme's advantage over a notch filter, which would necessarily attenuate signals of interest in its band. It should be noted that the measured response function has been incorporated into the calculation of the magnetic noise spectrum in Figure 4.

The response of the sensor in the feed forward mode is seen to be the same as in the unlocked mode, in Figure 5. This is as expected, as the feed-forward technique should not change the response of the sensor, only allow smaller signals to be resolved. The sensitivity of the device in unlocked and feed-forward modes is frequency specific. The resonance scan in Figure 2 has a sensitivity of 2.91 pT/ $\sqrt{\text{Hz}}$, where sensitivity is here estimated as the square root of the power spectral density (PSD):

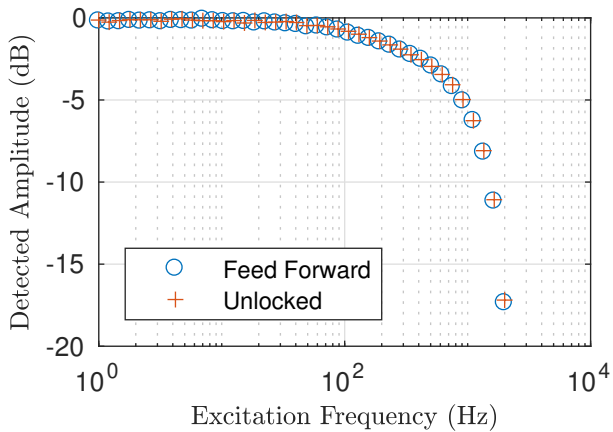


FIG. 5. Response of the sensor to applied magnetic fields of a fixed amplitude. The response rolls off to a -3 dB point of 520 Hz. The response of the sensor is identical in the unlocked and feed-forward modes.

| Condition | RMS Noise (V) | \sqrt{PSD} (pT/ $\sqrt{\text{Hz}}$) |
|-----------------------------|-----------------------|--|
| Laser blocked, B_{RF} on | 1.85×10^{-4} | 1.75(19) |
| Laser blocked, B_{RF} off | 2.28×10^{-4} | 1.46(75) |
| Laser on, B_{RF} off | 2.9×10^{-4} | 2.30(46) |
| Photon shot noise | 6.2×10^{-6} | 0.05 |

TABLE II. Contributions to noise in the sensor arising from primary noise sources in the experimental setup.

$$\sqrt{PSD} = \frac{1}{\sqrt{BW}} \frac{\delta B}{\delta X} \delta X \quad (3)$$

Where BW is the measured bandwidth of the sensor, $\frac{\delta B}{\delta X}$ is the gradient on resonance and δX is the RMS noise of the polarimeter signal after demodulation in the range 60-80 kHz, the range shown in Fig. 2. This gives an estimate of the magnetic noise the atoms are experiencing and transferring to the laser beam. This sensitivity figure reflects the ability of the sensor to resolve small changes in the field over a short measurement period of 20 ms. Over longer measurement periods the ambient magnetic noise contributes significantly.

Table II illustrates contributions to the sensitivity of the sensor as compared to our calculated photon shot-noise sensitivity. RMS noise was recorded for each condition for a 20 ms period and the equivalent sensitivity calculated using (3). This gives an indication of the contribution of optical noise, RF coils and the DAQ system. This feed-forward technique has the potential to be scaled to improve the duty cycle. A shorter unlocked measurement should still yield good noise suppression for 50 Hz and its main harmonics, and may couple less low-frequency noise to subsequent measurements.

IV. CONCLUSION

We have presented an experimental feed-forward technique that achieves suppression of periodic magnetic noise arising from the mains AC line primary frequency and its harmonics. The noise reduction is greatest around 50 Hz and 150 Hz, improving the sensor's ability to resolve magnetic signals around

this frequency band, with an amplitude reduction of 500 and a noise power reduction of 22 dB in the band of ± 5 Hz around the 50 Hz peak. The feed-forward mode is effective in tracking more closely the ambient periodic noise, as the applied B_{RF} is closer to the Larmor frequency for longer periods of time. This effect can be achieved with fast feedback, where the RF field continuously tracks the Larmor frequency in real-time. Constraints of our data acquisition system do not allow for fast enough feedback.

The response of the sensor to applied excitation fields is identical in the unlocked and feed-forward modes, rolling off to a bandwidth of 520 Hz, which is compatible with the pressure-broadened vapor cell used. This feed-forward scheme is easily implementable in an unshielded system where large amplitude periodic noise dominates. In its current form it lends itself to applications that do not require 100% duty cycle, and those where the signal to be measured is periodic or can be deterministically turned on and off. Although the results shown here focus on mains AC noise, this technique is readily implementable in any scenario that presents periodic magnetic noise. Fetal magnetocardiography provides a possible example. A fetal magnetocardiogram measurement may in theory be triggered from the mother's electrocardiogram, allowing her heart's large amplitude magnetic signal to be suppressed and improving recovery of the fetal heart rate.

ACKNOWLEDGMENTS

This work was funded by the UK Quantum Technology Hub in Sensing and Metrology, EPSRC grant N^o EP/M013294/1.

- ¹E. Ben-Yosef, M. Millman, R. Shaar, L. Tauxe, and O. Lipschits, Proceedings of the National Academy of Sciences of the United States of America **114**, 2160 (2017).
- ²D. T. Germain-Jones, Journal of Scientific Instruments **34**, 1 (1957).
- ³J. Belfi, G. Bevilacqua, V. Biancalana, S. Cartaleva, Y. Dancheva, and L. Moi, J. Opt. Soc. Am. B **24**, 2357 (2007).
- ⁴P. Bevington, R. Gartman, and W. Chalupczak, Review of Scientific Instruments **90**, 13103 (2019).
- ⁵L. Marmugi, L. Gori, S. Hussain, C. Deans, and F. Renzoni, Applied Optics **56**, 743 (2017).
- ⁶K. Jensen, M. A. Skarsfeldt, H. Stærkind, J. Arnbak, M. V. Balabas, S. P. Olesen, B. H. Bentzen, and E. S. Polzik, Scientific Reports **8**, 16218 (2018).
- ⁷J. H. Storm, M. Drung, M. Burghoff, and R. Körber, Superconductor Science and Technology **29**, 1 (2016).
- ⁸C. C. Lu, J. Huang, P. K. Chiu, S. L. Chiu, and J. T. Jeng, Sensors (Switzerland) **14**, 13815 (2014).
- ⁹I. K. Kominis, T. W. Kornack, J. C. Allred, and M. V. Romalis, Nature **422**, 596 (2003).
- ¹⁰I. M. Savukov and M. V. Romalis, Physical Review A - Atomic, Molecular, and Optical Physics **71** (2005), 10.1103/PhysRevA.71.023405.
- ¹¹L. Lenci, S. Barreiro, P. Valente, H. Failache, and A. Lezama, Journal of Physics B: Atomic, Molecular and Optical Physics **45** (2012), 10.1088/0953-4075/45/21/215401.
- ¹²S. J. Ingleby, I. C. Chalmers, C. O'Dwyer, P. F. Griffin, A. S. Arnold, and E. Riis, in 2017 IEEE SENSORS (2017).
- ¹³A. L. Bloom, Appl. Opt. **1**, 61 (1962).
- ¹⁴D. Hunter, S. Piccolomo, J. D. Pritchard, N. L. Brockie, T. E. Dyer, and E. Riis, Physical Review Applied **10**, 14002 (2018).
- ¹⁵E. Breschi, Z. D. Grujić, P. Knowles, and A. Weis, Applied Physics Letters **104** (2014), 10.1063/1.4861458.
- ¹⁶J. Belfi, G. Bevilacqua, V. Biancalana, R. Cecchi, Y. Dancheva, and L. Moi, Review of Scientific Instruments **81**, 065103 (2010).
- ¹⁷G. Bevilacqua, V. Biancalana, Y. Dancheva, and A. Vigilante, Physical Review Applied **11**, 14029 (2019).

- ¹⁸J. Malmivuo, J. Lekkala, P. Kontro, L. Suomaa, and H. Vihinen, *Journal of Physics E: Scientific Instruments* **20**, 151 (1987).
- ¹⁹C. Deans, L. Marmugi, and F. Renzoni, *Review of Scientific Instruments* **89**, 083111 (2018).
- ²⁰H. J. M. ter Brake, R. Huonker, and H. Rogalla, *Measurement Science and Technology* **4**, 1370 (1993).
- ²¹C. Flühmann and J. P. Home, *Encoding a qubit in the motion of a trapped-ion using superpositions of displaced squeezed states presented by*, Ph.D. thesis, ETH Zurich (2019).
- ²²B. Merkel, K. Thirumalai, J. E. Tarlton, V. M. Schäfer, C. J. Ballance, T. P. Harty, and D. M. Lucas, *Review of Scientific Instruments* **90**, 44702 (2019).
- ²³S. J. Ingleby, P. F. Griffin, A. S. Arnold, M. Chouliara, and E. Riis, *Review of Scientific Instruments* **88**, 043109 (2017).
- ²⁴S. J. Ingleby, C. O'Dwyer, P. F. Griffin, A. S. Arnold, and E. Riis, *Phys. Rev. A* **96**, 013429 (2017).

Bibliography

- [1] Massimo Guarnieri, “Once upon a time... The compass,” [IEEE Industrial Electronics Magazine](#) **8**, 60–63 (2014).
- [2] G. D. Garland, “The contributions of Carl Friedrich Gauss to geomagnetism,” [Historia Mathematica](#) **6**, 5–29 (1979).
- [3] M N Nabighian, V. J.S. Grauch, R O Hansen, T. R. LaFehr, Y Li, J W Peirce, J D Phillips, and M E Ruder, “The historical development of the magnetic method in exploration,” [Geophysics](#) **70** (2005), [10.1190/1.2133784](#).
- [4] Wallace H Campbell, “Quiet daily geomagnetic fields,” [Pure and Applied Geophysics](#) **131** (1989), [10.1016/0021-9169\(90\)90099-9](#).
- [5] William Gilbert, *On the Magnet, Magnetick Bodies also, and on the great magnet the earth; a new Physiology, demonstrated by many arguments & experiments* (Chiswick Press, 1600).
- [6] D. Macaluso and O. M. Corbino, “Sopra una nuova azione che la luce subisce attraversando alcuni vapori metallici in un campo magnetico,” [Il Nuovo Cimento Series 4](#) **8**, 257–258 (1898).
- [7] Szymon Pustelny, *Nonlinear magneto-optical effects*, [Ph.D. thesis](#), Jagiellonian University in Krakow (2007).
- [8] D Budker, W Gawlik, D F Kimball, S M Rochester, V V Yashchuk, and A Weis, “Resonant nonlinear magneto-optical effects in atoms,” [Reviews of Modern Physics](#) **74**, 1153–1201 (2002), [arXiv:0203077 \[physics\]](#) .
- [9] D F Jackson Kimball, E B Alexandrov, and D Budker, “A Brief History of Optical Magnetometry,” in *Optical Magnetometry*, edited by D. Bud-

- ker (Cambridge University Press, Cambridge, UK, 2013) Chap. 1, pp. 1–10.
- [10] William Happer, “Optical pumping,” *Reviews of Modern Physics* **44**, 169–249 (1972).
- [11] Jean Brossel and Alfred Kastler, “La detection de la resonance magnetique des niveaux excites-leffect de depolarisation des radiations de resonance optique et de fluorescence,” *Comptes Rendus Hebdomadaires Des Seances De L Academie Des Sciences* **229**, 1213—1215 (1949).
- [12] Jean Brossel and Francis Bitter, “A new "double resonance" method for investigating atomic energy levels. Application to Hg,” *Physical Review* **86**, 308–316 (1952).
- [13] William E. Bell and Arnold L. Bloom, “Optically driven spin precession,” *Physical Review Letters* **6**, 280–281 (1961).
- [14] W Gawlik, J Kowalski, R Neumann, and F. Träger, “Observation of the electric hexadecapole moment of free Na atoms in a forward scattering experiment,” *Optics Communications* **12**, 400–404 (1974).
- [15] W Gawlik, J Kowalski, R Neumann, and F. Träger, “Strong narrowing of the Na forward scattering signals due to the interaction with an intense dye laser field,” *Physics Letters A* **48**, 283–284 (1974).
- [16] Dmitry Budker and Michael Romalis, “Optical magnetometry,” *Nature Physics* **3**, 227–234 (2007), arXiv:0611246 [physics] .
- [17] Igor Savukov, “Ultra-Sensitive Optical Atomic Magnetometers and Their Applications,” in *Advances in Optical and Photonic Devices*, January, edited by Kim Ki Young (INTECH, 2010) Chap. 17.
- [18] Vivien Mathé, François Lévêque, Pierre Etienne Mathé, Claude Chevalier, and Yves Pons, “Soil anomaly mapping using a caesium magnetometer: Limits in the low magnetic amplitude case,” *Journal of Applied Geophysics* **58**, 202–217 (2006).
- [19] P Bevington, R Gartman, and W Chalupczak, “Imaging of material defects with a radio-frequency atomic magnetometer,” *Review of Scientific Instruments* **90**, 13103 (2019).

- [20] Cameron Deans, *Electromagnetic induction imaging with atomic magnetometers*, Ph.D. thesis, University College London (2017).
- [21] V Gerginov, F. C.S. Da Silva, and D Howe, “Prospects for magnetic field communications and location using quantum sensors,” [Review of Scientific Instruments](#) **88**, 125005 (2017).
- [22] I. K. Kominis, T. W. Kornack, J. C. Allred, and M. V. Romalis, “A subfemtotesla multichannel atomic magnetometer,” [Nature](#) **422**, 596–599 (2003).
- [23] H. B. Dang, A. C. Maloof, and M. V. Romalis, “Ultrahigh sensitivity magnetic field and magnetization measurements with an atomic magnetometer,” [Applied Physics Letters](#) **97**, 28–30 (2010), [arXiv:0910.2206](#) .
- [24] I M Savukov and M V Romalis, “Effects of spin-exchange collisions in a high-density alkali-metal vapor in low magnetic fields,” [Physical Review A - Atomic, Molecular, and Optical Physics](#) **71** (2005), 10.1103/Phys-RevA.71.023405.
- [25] Elena Boto, Zelekha A. Seedat, Niall Holmes, James Leggett, Ryan M. Hill, Gillian Roberts, Vishal Shah, T. Mark Fromhold, Karen J. Mullinger, Tim M. Tierney, Gareth R. Barnes, Richard Bowtell, and Matthew J. Brookes, “Wearable neuroimaging: Combining and contrasting magnetoencephalography and electroencephalography,” [NeuroImage](#) **201**, 116099 (2019).
- [26] D. F. Jackson Kimball, S. K. Lamoreaux, and T. E. Chupp, “Tests of fundamental physics with optical magnetometers,” in [Optical Magnetometry](#), Vol. 9781107010, edited by Dmitry Budker and Derek F. Jackson Kimball (Cambridge University Press, Cambridge, 2011) Chap. 18, pp. 339–368.
- [27] J. H. Storm, D. Drung, M. Burghoff, and R. Körber, “A modular, extendible and field-tolerant multichannel vector magnetometer based on current sensor SQUIDs,” [Superconductor Science and Technology](#) **29**, 1–11 (2016), [arXiv:1708.08382](#) .

- [28] Chih Cheng Lu, Jeff Huang, Po Kai Chiu, Shih Liang Chiu, and Jen Tzong Jeng, “High-sensitivity low-noise miniature fluxgate magnetometers using a flip chip conceptual design,” *Sensors (Switzerland)* **14**, 13815–13829 (2014).
- [29] Luca Marmugi, Lorenzo Gori, Sarah Hussain, Cameron Deans, and Ferruccio Renzoni, “Remote detection of rotating machinery with a portable atomic magnetometer,” *Applied Optics* **56**, 743 (2017), [arXiv:1701.05385](#) .
- [30] Vishal Shah, Svenja Knappe, Peter D.D. Schwindt, and John Kitching, “Subpicotesla atomic magnetometry with a microfabricated vapour cell,” *Nature Photonics* **1**, 649–652 (2007).
- [31] M E Limes, E L Foley, T W Kornack, S Caliga, S. McBride, A Braun, W Lee, V G Lucivero, and M V Romalis, “Total-field atomic gradiometer for unshielded portable magnetoencephalography,” [arXiv:2001.03534](#) (2020), [arXiv:2001.03534](#) .
- [32] D. Sheng, A. R. Perry, S. P. Krzyzewski, S. Geller, J. Kitching, and S. Knappe, “A microfabricated optically-pumped magnetic gradiometer,” *Applied Physics Letters* (2017), 10.1063/1.4974349, [arXiv:1701.03236](#) .
- [33] H. Xia, A. Ben-Amar Baranga, D. Hoffman, and M. V. Romalis, “Magnetoencephalography with an atomic magnetometer,” *Applied Physics Letters* **89**, 211104 (2006).
- [34] Robert Wyllie, Matthew Kauer, Ronald T. Wakai, and Thad G. Walker, “Optical magnetometer array for fetal magnetocardiography,” *Optics Letters* **37**, 2247 (2012), [arXiv:1202.5019](#) .
- [35] Carolyn O’Dwyer, Stuart J. Ingleby, Iain C. Chalmers, Paul F. Griffin, and Erling Riis, “A feed-forward measurement scheme for periodic noise suppression in atomic magnetometry,” *Review of Scientific Instruments* **91**, 1–5 (2020).
- [36] Igor I. Sobelman, *Atomic Spectra and Radiative Transitions*, Vol. 53 (Springer Berlin Heidelberg, 1992) pp. 1689–1699, [arXiv:arXiv:1011.1669v3](#) .

- [37] Jacques Vanier and Claude Audoin, *The Quantum Physics of Atomic Frequency Standards* (1989).
- [38] Daniel Adam Steck, *Cesium D Line Data, Revision 2.1.4, 23 December 2010*, Tech. Rep. (Oregon Center for Optics and Department of Physics, University of Oregon, 1998).
- [39] Christopher J Foot, *Atomic Physics*, 1st ed. (Oxford University Press, 2004).
- [40] Dominic Hunter, *Chip-Scale Atomic Magnetometer Based on Free-Induction-Decay*, Ph.D. thesis, University of Strathclyde (2019).
- [41] Jenelle Rajroop, *Radio-frequency atomic magnetometers : an analysis of interrogation regimes*, Ph.D. thesis, University College London (2018).
- [42] Marcis Auzinsh, Dmitry Budker, and Simon M. Rochester, *Optically polarized atoms: understanding light-atom interactions*, Vol. 1 (Oxford University Press, 2010).
- [43] Yijie Pan, Wenhan Liao, He Wang, Yan Yao, Jinhui Cai, and Jifeng Qu, “Cesium atomic Doppler broadening thermometry for room temperature measurement,” *Chinese Optics Letters* **17**, 3–6 (2019).
- [44] Theo Scholtes, Stefan Woetzel, Rob IJsselsteijn, Volkmar Schultze, and Hans Georg Meyer, “Intrinsic relaxation rates of polarized Cs vapor in miniaturized cells,” *Applied Physics B: Lasers and Optics* **117**, 211–218 (2014).
- [45] Scott Jeffrey Seltzer, *Developments in Alkali-Metal Atomic Magnetometry*, Ph.D. thesis, Princeton University (2008).
- [46] N. Castagna, G. Bison, G. Di Domenico, A. Hofer, P. Knowles, C. MacChione, H. Saudan, and A. Weis, “A large sample study of spin relaxation and magnetometric sensitivity of paraffin-coated Cs vapor cells,” *Applied Physics B: Lasers and Optics* **96**, 763–772 (2009), [arXiv:0812.4425](https://arxiv.org/abs/0812.4425) .
- [47] Gianni Di Domenico, Hervé Saudan, Georg Bison, Paul Knowles, and Antoine Weis, “Sensitivity of double-resonance alignment magnetometers,” *Physical Review A - Atomic, Molecular, and Optical Physics* **76** (2007), [10.1103/PhysRevA.76.023407](https://doi.org/10.1103/PhysRevA.76.023407).

- [48] Paul K Dixon and Lei Wu, “Broadband digital lock-in amplifier techniques,” *Review of Scientific Instruments* **60**, 3329–3336 (1989).
- [49] D. F. Jackson Kimball, E. B. Alexandrov, and D. Budker, “General principles and characteristics of optical magnetometers,” in *Optical Magnetometry*, Vol. 9781107010, edited by Dmitry Budker and Derek F. Jackson Kimball (Cambridge University Press, Cambridge, 2011) Chap. 1, pp. 3–24.
- [50] Vito Giovanni Lucivero, Pawel Anielski, Wojciech Gawlik, and Morgan W Mitchell, “Shot-noise-limited magnetometer with sub-picotesla sensitivity at room temperature,” *Review of Scientific Instruments* **85** (2014), 10.1063/1.4901588, arXiv:1403.7796 .
- [51] V Schultze, R. I. Jsselsteijn, and H. G. Meyer, “Noise reduction in optically pumped magnetometer assemblies,” *Applied Physics B: Lasers and Optics* **100**, 717–724 (2010).
- [52] David A Keder, David W Prescott, Adam W Conovaloff, and Karen L Sauer, “An unshielded radio-frequency atomic magnetometer with sub-femtoTesla sensitivity,” *AIP Advances* **4**, 127159 (2014).
- [53] D Hunter, S Piccolomo, J D Pritchard, N L Brockie, T E Dyer, and E Riis, “Free-Induction-Decay Magnetometer Based on a Microfabricated Cs Vapor Cell,” *Physical Review Applied* **10**, 14002 (2018).
- [54] E. Breschi, Z. D. Grujic, P. Knowles, and A. Weis, “A high-sensitivity push-pull magnetometer,” *Applied Physics Letters* **104** (2014), 10.1063/1.4861458, arXiv:1312.3567 .
- [55] Stuart J. Ingleby, Carolyn O’Dwyer, Paul F. Griffin, Aidan S. Arnold, and Erling Riis, “Orientational effects on the amplitude and phase of polarimeter signals in double-resonance atomic magnetometry,” *Physical Review A* **96**, 1–6 (2017), arXiv:1707.04418 .
- [56] Stuart J. Ingleby, Carolyn O’Dwyer, Paul F. Griffin, Aidan S. Arnold, and Erling Riis, “Vector Magnetometry Exploiting Phase-Geometry Effects in a Double-Resonance Alignment Magnetometer,” *Physical Review Applied* **10**, 034035 (2018), arXiv:1802.09273 .

- [57] V V Yashchuk, S.-K. Lee, and E Paperno, “Magnetic shielding,” in *Optical Magnetometry*, edited by Dmitry Budker and Derek F. Jackson Kimball (Cambridge University Press, Cambridge, 2013) Chap. 12, pp. 225–248.
- [58] C P Bidinosti and J W Martin, “Passive magnetic shielding in static gradient fields,” *AIP Advances* **4**, 47135 (2014), [arXiv:1310.8242](#) .
- [59] T. J. Sumner, J. M. Pendlebury, and K. F. Smith, “Convictional magnetic shielding,” *Journal of Physics D: Applied Physics* **20**, 1095–1101 (1987).
- [60] S. J. Ingleby, P. F. Griffin, A. S. Arnold, M. Chouliara, and E. Riis, “High-precision control of static magnetic field magnitude, orientation, and gradient using optically pumped vapour cell magnetometry,” *Review of Scientific Instruments* **88** (2017), [10.1063/1.4980159](#).
- [61] S Pustelny, D. F. Jackson Kimball, S M Rochester, V V Yashchuk, and D Budker, “Influence of magnetic-field inhomogeneity on nonlinear magneto-optical resonances,” *Physical Review A - Atomic, Molecular, and Optical Physics* **74** (2006), [10.1103/PhysRevA.74.063406](#).
- [62] M Lapaine, “Mollweide Map Projection,” *KoG* , 7–16 (2011).
- [63] Antoine Weis, Georg Bison, and Anatoly S. Pazgalev, “Theory of double resonance magnetometers based on atomic alignment,” *Physical Review A - Atomic, Molecular, and Optical Physics* **74** (2006), [10.1103/PhysRevA.74.033401](#), [arXiv:0605234 \[physics\]](#) .
- [64] Greg A Pitz, Douglas E Wertepny, and Glen P Perram, “Pressure broadening and shift of the cesium D1 transition by the noble gases and N₂, H₂, HD, D₂, CH₄, C₂ H₆, CF₄, and H₃ e,” *Physical Review A - Atomic, Molecular, and Optical Physics* **80** (2009), [10.1103/PhysRevA.80.062718](#).
- [65] T Scholtes, V Schultze, R. IJsselsteijn, S Woetzel, and H.-G. Meyer, “Light-narrowed optically pumped magnetometer with a miniaturized Cs cell,” *Physical Review A* **84**, 043416 (2011).
- [66] A Andalkar and R B Warrington, “High-resolution measurement of the pressure broadening and shift of the Cs D1 and D2 lines by N₂ and

- He buffer gases,” [Physical Review A - Atomic, Molecular, and Optical Physics](#) **65**, 7 (2002).
- [67] S Appelt, A Baranga, CJ Erickson, MV Romalis, AR Young, and W Happer, “Theory of spin-exchange optical pumping of ^3He and ^{129}Xe ,” [Physical Review A](#) **58**, 1412 (1998).
- [68] Yangying Fu, Xiaohu Liu, and Jie Yuan, “Light narrowing of cesium magnetic-resonance lines in a radio-frequency atomic magnetometer,” [AIP Advances](#) **9** (2019), [10.1063/1.5043231](#).
- [69] D. Budker, D. F. Kimball, S. M. Rochester, V. V. Yashchuk, and M. Zolotarev, “Sensitive magnetometry based on nonlinear magneto-optical rotation,” [Physical Review A](#) **62**, 043403 (2000).
- [70] M Auzinsh, A Berzins, R Ferber, F Gahbauer, L Kalvans, A Mozers, and A Spiss, “Alignment-to-orientation conversion in a magnetic field at nonlinear excitation of the D2 line of rubidium: Experiment and theory,” [Physical Review A - Atomic, Molecular, and Optical Physics](#) **91**, 53418 (2015), [arXiv:1503.03334](#) .
- [71] D. Budker, D. F. Kimball, S. M. Rochester, and V. V. Yashchuk, “Non-linear Magneto-optical Rotation via Alignment-to-Orientation Conversion,” [Physical Review Letters](#) **85**, 4–7 (2000).
- [72] T Manabe, T Yabuzaki, and T Ogawa, “Observation of collisional transfer from alignment to orientation of atoms excited by a single-mode laser,” [Physical Review Letters](#) **46**, 637–640 (1981).
- [73] S. M. Rochester, M. P. Ledbetter, T. Zigdon, A. D. Wilson-Gordon, and D. Budker, “Orientation-to-alignment conversion and spin squeezing,” [Physical Review A - Atomic, Molecular, and Optical Physics](#) **85**, 22125 (2012), [arXiv:1106.3538](#) .
- [74] J Malmivuo, J Lekkala, P Kontro, L Suomaa, and H Vihinen, “Improvement of the properties of an eddy current magnetic shield with active compensation,” [Journal of Physics E: Scientific Instruments](#) **20**, 151–164 (1987).

- [75] Cameron Deans, Luca Marmugi, and Ferruccio Renzoni, “Sub-picotesla widely tunable atomic magnetometer operating at roomtemperature in unshielded environments,” *Review of Scientific Instruments* **89**, 083111 (2018), [arXiv:1804.05124](#) .
- [76] H. J M ter Brake, R Huonker, and H Rogalla, “New results in active noise compensation for magnetically shielded rooms,” *Measurement Science and Technology* **4**, 1370–1375 (1993).
- [77] Andrew Heim, “[Make it Faster: More Throughput or Less Latency?](#)” (2019).
- [78] Christa Flühmann, *Encoding a qubit in the motion of a trapped-ion using superpositions of displaced squeezed states presented by*, Ph.D. thesis, ETH Zurich (2019).
- [79] B. Merkel, K. Thirumalai, J. E. Tarlton, V. M. Schäfer, C. J. Ballance, T. P. Harty, and D. M. Lucas, “Magnetic field stabilization system for atomic physics experiments,” *Review of Scientific Instruments* **90**, 44702 (2019), [arXiv:1808.03310](#) .
- [80] Kasper Jensen, Mark Alexander Skarsfeldt, Hans Stærkind, Jens Arnbak, Mikhail V. Balabas, Søren Peter Olesen, Bo Hjorth Bentzen, and Eugene S. Polzik, “Magnetocardiography on an isolated animal heart with a room-temperature optically pumped magnetometer,” *Scientific Reports* **8**, 16218 (2018), [arXiv:1806.10954](#) .
- [81] G. Bison, N. Castagna, A. Hofer, P. Knowles, J.-L. L. Schenker, M. Kasprzak, H. Saudan, and A. Weis, “A room temperature 19-channel magnetic field mapping device for cardiac signals,” *Applied Physics Letters* **95**, 173701 (2009), [arXiv:0906.4869](#) .
- [82] Shoujun Xu, Simon M. Rochester, Valeriy V. Yashchuk, Marcus H. Donaldson, and Dmitry Budker, “Construction and applications of an atomic magnetic gradiometer based on nonlinear magneto-optical rotation,” *Review of Scientific Instruments* **77**, 083106 (2006).
- [83] Rui Zhang, Kenneth Smith, and Rahul Mhaskar, “Highly sensitive miniature scalar optical gradiometer,” *Proceedings of IEEE Sensors* **1**, 1–3 (2017).

-
- [84] R H Koch, J R Rozen, J Z Sun, and W J Gallagher, “Three SQUID gradiometer,” *Appl. Phys. Lett* **63**, 403 (1993).
- [85] Alexey V Veryaskin, “Magnetic gradiometry,” in *Magnetic and Electromagnetic Gradiometry. Strategic Technologies in the 21st Century* (Morgan & Claypool Publishers, 2018) Chap. Gravity, M.
- [86] Giuseppe Bevilacqua, Valerio Biancalana, Piero Chessa, and Yordanka Dancheva, “Multichannel optical atomic magnetometer operating in unshielded environment,” *Applied Physics B: Lasers and Optics* **122**, 1–9 (2016), [arXiv:1601.06938](https://arxiv.org/abs/1601.06938) .
- [87] C. Affolderbach, M. Stähler, S. Knappe, and R. Wynands, “An all-optical, high-sensitivity magnetic gradiometer,” *Applied Physics B: Lasers and Optics* **75**, 605–612 (2002).
- [88] Keigo Kamada, Yosuke Ito, Sunao Ichihara, Natsuhiko Mizutani, and Tetsuo Kobayashi, “Noise reduction and signal-to-noise ratio improvement of atomic magnetometers with optical gradiometer configurations,” *Optics Express* **23**, 6976 (2015).
- [89] Rui Zhang, Rahul Mhaskar, Ken Smith, and Mark Prouty, “Portable Intrinsic Gradiometer for Ultra-Sensitive Detection of Magnetic Gradient in Unshielded Environment,” *Appl. Phys. Lett* **143501**, 16–21 (2020).